The Dissertation Committee for Xing Liu Certifies that this is the approved version of the following Dissertation

Gyrokinetic Simulation of Pedestal Turbulence Using GENE

Committee:

Swadesh M. Mahajan, Co-Supervisor

Richard D. Hazeltine, Co-Supervisor

Francois L. Waelbroeck

Gary A. Hallock

Gyrokinetic Simulation of Pedestal Turbulence Using GENE

by

Xing Liu

Dissertation

Presented to the Faculty of the Graduate School of

The University of Texas at Austin

in Partial Fulfillment

of the Requirements

for the Degree of

DOCTOR OF PHILOSOPHY

The University of Texas at Austin

August 2018

Acknowledgements

I would like to express my sincere gratitude to Dr. Mike Kotschenreuther, Professor Swadesh Mahajan and Dr. David Hatch for the continuous support of my PhD study and research. I thank Mike for his immense knowledge, otherworldly creativity and relentless perseverance which have shaped this dissertation. I thank Professor Mahajan for his motivation, wisdom and guidance that has helped me in all the time of research – I could not have imagined a better advisor for my PhD study. I thank David for giving me access to the GENE code and helping me solve issues, big and small, to make all the results in this work possible.

I would like to thank the rest of my dissertation committee: Professor Richard Hazeltine, Professor Francois Waelbroeck and Professor Gary Hallock, for their insightful comments and encouragement. I thank Professor Waelbroeck for kindly stepping in as my advisor in my third year and for supporting my decision to attend the Insight Data Science program in Seattle in the 2018 Spring semester.

My sincere thanks also go to Dr. Rich Groebner, Dr. Ahmed Diallo, Dr. Jerry Hughes and Dr. Amanda Hubbard for providing the experimental data.

I thank Dr. Gabriele Merlo for sharing his knowledge of GENE with me and for setting up GENE on supercomputers.

Also, I thank Professor Michael Barnes who provided me the opportunity to enter the gyrokinetics world.

Last but not the least, I would like to thank my parents for supporting me in pursuing a PhD degree and for their emphasis on hardworking when they raise me up.

Abstract

Gyrokinetic Simulation of Pedestal Turbulence Using GENE

Xing Liu, Doctor of Philosophy

The University of Texas at Austin, 2018

Supervisors: Swadesh M. Mahajan, Richard D. Hazeltine

We present here a study based on gyrokinetic simulations (using GENE) to model turbulence in the pedestals on several well-diagnosed shots: two H-modes on DIII-D and one I-mode on Alcator C-Mod. We match frequencies, power balance, and other transport characteristics in multiple channels with the observations. The observed quasi-coherent fluctuations on the DIII-D shots are identified as Micro Tearing Modes (MTM). The MTMs match frequency and power balance (together with heat loss from Electron Temperature Gradient (ETG) driven turbulence), and cause low transport in the particle, ion heat and impurity particle transport channels – consistent with observed inter-ELM evolution of ion and electron temperature, electron and impurity density or transport analysis of those channels. We find the Weakly Coherent Mode on C-Mod I-mode to be an electrostatic Ion Temperature Gradient/Impurity density gradient (ITG/Impurity) driven mode. The ITG/Impurity mode match frequency and the impurity confinement time observed on the I-mode. Electron scale turbulence, ETG, provides energy transport to match power balance. A novel concept called the transport fingerprints is used throughout this work, which greatly assists in identifying the instabilities. This work shows that the concept should be very valuable in many future investigations of pedestal turbulence.

Table of Contents

Table of Contents vi

List of Tables viii

List of Figures ix

INTRODUCTION 1

CHAPTER I: INVESTIGATIONS OF AN I-MODE PEDESTAL ON ALCATOR C-MOD 3

I-mode introduction 3

Global linear simulations 4

Ion temperature gradient scale length (a/L_{Ti}) scan 5

Density gradient scale length (a/L_{ne}) scan 8

Collisionality scan 9

Impurity density gradient (a/L_{nz}) scan 10

Summary of conclusions for the density transport 12

Diffusivity inferences based on experimental profiles and sources 13

Global simulation grid choice and convergence test 15

Nonlinear global simulations 17

Convergence test 18

Nonlinear ITG/Impurity thermal transport 19

Nonlinear ETG thermal transport 21

Impurity confinement time 24

Synthetic diagnostics and Geodesic Acoustic Modes 27

CHAPTER II: INVESTIGATIONS OF TWO DIII-D PEDESTALS IN ELMY H-MODES.....31

DIIID H-modes Introduction 31

Analysis of DIII-D shots 153674/5 and 98889 32

DIII-D Shot 153674/5 — experimental observations and their implications 34

DIII-D shot 98889 – experimental observations and their implications 41

Summary of conclusions of the experimental comparisons for shots 153674/5 and 98889 44

Equilibrium considerations for DIII-D shots 153674/5 and 98889 44

Gyrokinetic analysis of DIII-D discharges 153674/5 and 98889 46

MHD-like modes 51

Micro-Tearing Modes MTM 63

Electrostatic modes 86

Toroidal Alfven Eigenmode/ Micro Tearing Modes (TAE/MTM) 102

CONCLUSION 107

C-Mod I-mode 107

DIII-D H-modes 107

Reference 109

List of Tables

Table 1.1: Toroidal mode number scan result. 5

Table 1.2: Ion temperature gradient scale length variation result. 6

Table 1.3: Density gradient scale length variation result. k_z is the mode wavenumber along the magnetic field line. 8

Table 1.4: Collisionality scan result. 9

Table 1.5: Impurity density gradient scale length variation result. 11

Table 1.6: Convergence test results. 17

Table 1.7: Nonlinear ETG simulation convergence test. 21

Table 1.8: Radial location scan of heat loss from nonlinear ETG simulations. 22

Table 1.9: τ scan of heat loss from nonlinear ETG simulations at $\rho_t = 0.975$. 23

Table 1.10: η_e scan of heat loss from nonlinear ETG simulations at $\rho_t = 0.97$ and 0.975 23

Table 2.1: Transport Fingerprint for global linear MTM. 75

Table 2.2: Global MTM with and without ExB shear 76

Table 2.3: Table of Global MTM versus mode number n for shot 98889. 79

Table 2.4: Summary of nonlinear MTM simulation results. 84

Table 2.5: Summary of nonlinear ETG simulation results. 89

Table 2.6: Summary of global linear MTM simulation result for DIIID 98889 n=18. ...106

List of Figures

Figure 1.1: Pressure profile and simulation box. 4

Figure 1.2: η_i profile in the pedestal region. 7

Figure 1.3: Absolute value of γ_{ExB} from experimental Er profile in the pedestal region. 7

Figure 1.4: Mode structure of the electrostatic potential (ϕ) in a typical global simulation. 7

Figure 1.5: Electron and ion temperature profiles in the pedestal region. 13

Figure 1.6: Electron density profile in the pedestal region. 13

Figure 1.7: T_e, T_i, n_e profiles and simulation box. Black vertical lines indicate the boundaries of simulation box. Black dashed lines indicate the edges of buffer zone on each side. 16

Figure 1.8: E_r-well and simulation box. Black vertical lines indicate the boundaries of simulation box. Black dashed lines indicate the edges of buffer zone on each side. 16

Figure 1.9: Time series plot of electrostatic heat loss for ion scale nonlinear simulations. 10 mode number simulation is shown in black for ion heat loss, and blue for electron. 16 mode number simulation is shown in green for ion heat loss, and magenta for electron. 18

Figure 1.10: Spectra of electrostatic heat loss for ion scale nonlinear simulations. $\Delta n = 4$ simulation is shown in black for ion heat loss, and blue for electron. $\Delta n = 6$ simulation is shown in green for ion heat loss, and magenta for electron. 19

Figure 1.11: Radial profile of ion electrostatic heat loss for simulations using different impurity profiles. 20

Figure 1.12: Radial profile of electron electrostatic heat loss for simulations using different impurity profiles. 20

Figure 1.13: Nonlinear power loss (MW) from ETG turbulence. Results from η_e scan and τ scan are also added to the graph. 24
Figure 1.14: Impurity profiles in the pedestal for the simulations designed to estimate impurity confinement time.....25
Figure 1.15: Plot of impurity particle loss rate versus total impurity particle number. 26
Figure 1.16(a): An example of results of GPI synthetic diagnostic that matches experiment.....29
Figure 1.16(b): An example of results of GPI synthetic diagnostic that doesn't match experiment.....30
Figure 2.1 DIII-D shot 153674 a) Magnetic spectrogram of the experimentally observed fluctuations, showing measured QCF b) From experimental profiles, frequencies f for: Doppler shift (ω_{ExB}), ω_e*, and the QCF. The circle shows the experimentally inferred maximum amplitude position of the fluctuation. 35
Figure 2.2: DIII-D shot 153674 Inter-ELM evolution of T_e gradient and QCF amplitude showing strong correlation, expected for an MTM b) Evolution of the electron density gradient, which saturates much more quickly, and is unaffected by the growing QCF c) Evolution of T_i and n_{Carbon} after an ELM, for a typical ELM cycle, showing no discernable effect of growing QCFs- consistent with MTMs, but not KBMs. Note the difference between values on two cords is proportional to the average gradient between them. Hence, the gradient of T_i and n_c between the cords is apparently unaffected by the growing QCF.....38
Figure 2.3: DIII-D shot 98889 a) Magnetic spectrogram showing measured QCF b) From experimental profiles, frequencies f for: Doppler shift (ω_{ExB}), ω_e*, and the QCF. 42

Figure 2.4: plots of pressure, q and shat for both equilibria (Left: 98889, Right: 153764) 45
Figure 2.5: Profiles of T_e, T_i and n_e for the case 98889 (left) and 153674/5 (right) 49
Figure 2.6: Modified profiles for case 153674/5. Despite the slight changes, magnetic shear is altered significantly 50
Figure 2.7 (a): Mode growth rates for $k_y\rho_s$ scan for DIIID 153764 base case at ρ_t = 0.972 51
Figure 2.7 (b): $<E_{\|}>$ for $k_y\rho_s$ scan for DIIID 153764 base case at ρ_t = 0.972. 53
Figure 2.7 (c): Ratio of electromagnetic to electrostatic heat flux for $k_y\rho_s$ scan for DIIID 153764 base case at ρ_t = 0.972. 53
Figure 2.7 (c): Ratio of ion to electron thermal diffusivity for $k_y\rho_s$ scan for DIIID 153764 base case at ρ_t = 0.972. 54
Figure 2.7 (d): Ratio of electron particle diffusivity to thermal diffusivity for $k_y\rho_s$ scan for DIIID 153764 base case at ρ_t = 0.972. 55
Figure 2.7 (e): Ratio of impurity particle diffusivity to electron thermal diffusivity for $k_y\rho_s$ scan for DIIID 153764 base case at ρ_t = 0.972. 55
Figure 2.7 (f): Mode frequency (in plasma frame) normalized to ω_e* for $k_y\rho_s$ scan for DIIID 153764 base case at ρ_t = 0.972. 56
Figure 2.7 (g): Mode frequency (in lab frame) for $k_y\rho_s$ <= 0.15 scan for DIIID 153764 base case at ρ_t = 0.972. 57
Figure 2.7 (h): Growth rate vs. (normalized) radial wavenumber $k_x\rho_s$, for both the nominal beta and 1.3 times this value, for the $k_y\rho_s$ of the measured fluctuation. The MHD-like mode only exists over a small range of $k_x\rho_s$, so that it cannot fit into a "box" of the width of a pedestal. 58
Figure 2.8 (a): Mode growth rates for $k_y\rho_s$ scan for DIIID 98889 at ρ_t = 0.95. 59
Figure 2.8 (b): $<E_{\|}>$ for $k_y\rho_s$ scan for DIIID 98889 at ρ_t = 0.95. 59

Figure 2.8 (c): Ratio of electromagnetic to electrostatic heat flux for $k_y\rho_s$ scan for DIIID 98889 at $\rho_t = 0.95$. 60
Figure 2.8 (d): Ratio of ion thermal diffusivity to electron thermal diffusivity for $k_y\rho_s$ scan for DIIID 98889 at $\rho_t = 0.95$. 60
Figure 2.8 (e): Ratio of electron particle diffusivity to thermal diffusivity for $k_y\rho_s$ scan for DIIID 98889 at $\rho_t = 0.95$. 61
Figure 2.8 (f): Ratio of impurity particle diffusivity to electron thermal diffusivity for $k_y\rho_s$ scan for DIIID 98889 at $\rho_t = 0.95$. 61
Figure 2.8 (g): Mode frequency in the lab frame for $k_y\rho_s$ scan for DIIID 98889 at $\rho_t = 0.95$....62
Figure 2.9 (a): Local linear growth rates of shot 153674/5 in the mid-pedestal range ($\rho_t = 0.982$). Results are also shown for the modified profiles at the same radial location.....63
Figure 2.9 (b): Frequency of the MTM in local linear runs at the mid pedestal for 153674/5, normalized to ω_e*; ω is close to ω_e*.....65
Figure 2.9 (c): Mode frequency (in lab frame) for DIIID 153764 at $\rho_t = 0.982$. 65
Figure 2.9 (d): Ratio of electromagnetic to electrostatic heat flux for toroidal mode number scan for DIIID 153764 at $\rho_t = 0.982$. 66
Figure 2.9 (e): Ratio of ion to electron thermal diffusivity for toroidal mode number scan for DIIID 153764 at $\rho_t = 0.982$. 67
Figure 2.9 (f): Ratio of electron particle diffusivity to thermal diffusivity for toroidal mode number scan for DIIID 153764 at $\rho_t = 0.982$. 67
Figure 2.9 (g): Ratio of impurity diffusivity to electron thermal diffusivity for toroidal mode number scan for DIIID 153764 at $\rho_t = 0.982$. 68
Figure 2.9 (h): Growth rate vs. (normalized) radial wavenumber $k_x\rho_s$ for DIIID 153764 base case at $\rho_t = 0.982$ for n = 17. 69

Figure 2.9 (i): Growth rate vs. (normalized) radial wavenumber $k_x\rho_s$ for DIIID 153764 mod1 case at $\rho_t = 0.982$ for n = 13. 70

Figure 2.9 (j): Growth rate vs. (normalized) radial wavenumber $k_x\rho_s$ for DIIID 153764 mod3 case at $\rho_t = 0.982$ for n = 13. 70

Figure 2.9 (k): Growth rate vs. (normalized) radial wavenumber $k_x\rho_s$ for DIIID 153764 mod5 case at $\rho_t = 0.982$ for n = 15 and n = 20. 71

Figure 2.9 (l): Growth rate vs. (normalized) radial wavenumber $k_x\rho_s$ for DIIID 98889 at $\rho_t = 0.972$ for n = 18. 72

Figure 2.9 (m): Global linear growth rates of shot 153674/5 base case and the modified cases. 73

Figure 2.9 (n): Global linear frequencies in the lab frame of shot 153674/5 base case and the modified cases. 74

Figure 2.10 (a): Local linear toroidal mode number scan for DIIID 98889 at ρ_t = 0.972 76

Figure 2.10 (b): Frequencies track ω_e* for toroidal mode number scan for DIIID 98889 at $\rho_t = 0.972$. 77

Figure 2.10 (c): Frequency in the lab frame for toroidal mode number scan for DIIID 98889 at $\rho_t = 0.972$. 77

Figure 2.10 (d) The ratio of quasilinear electromagnetic to electrostatic heat flux for toroidal mode number scan for DIIID 98889 at $\rho_t = 0.972$. Electromagnetic dominates for most n. 78

Figure 2.10 (e): Transport fingerprints for toroidal mode number scan for DIIID 98889 at $\rho_t = 0.972$. 79

Figure 2.11 (a): Time evolution of the space averaged heat flux in GENE, showing the linear growth phase, nonlinear saturation phase, and nonlinear instability phase for the nominal β simulation (Black). Reduced β simulation with longer saturation phase is also shown (Blue). 81

Figure 2.11(b): Profile modifications in nonlinear MTM simulations. Shown is a typical case, mod5 n=15. Note that only the T_e profile is significantly affected. This is consistent with the inter-ELM profile evolution seen on shot 153674/5. Dynamic profiles (solid line) from nonlinear simulation are compared to the equilibrium profiles (dashed line). 82

Figure 2.11(c): Heat flux profile in the pedestal averaged in the nonlinearly saturated state for DIIID 153764 mod5 case, n=15.....82

Figure 2.11(d): Heat flux profile in the pedestal averaged in the nonlinearly saturated state for DIIID 98889, n=16 and n=18. 83

Figure 2.11 (e): Time evolution of the space averaged heat flux in GENE, showing the linear growth phase, nonlinearly crashing phase for mod1, n = 13. 84

Figure 2.12 (a): Growth rates of ETG modes at mid-pedestal locations for the DIII-D pedestals.....86

Figure 2.12 (b): Ratio of ion to electron thermal diffusivity of ETG modes at mid-pedestal locations for the DIII-D pedestals.....87

Figure 2.12 (c): Ratio of electron particle to thermal diffusivity of ETG modes at mid-pedestal locations for the DIII-D pedestals. 87

Figure 2.12 (d): Ratio of impurity diffusivity to electron thermal diffusivity of ETG modes at mid-pedestal locations for the DIII-D pedestals.....88

Figure 2.12 (e): Ratio of ion particle diffusivity to electron thermal diffusivity of ETG modes at mid-pedestal locations for the DIII-D pedestals. 88

Figure 2.13 (a): Heat flux spectra versus $k_x\rho_s$ for nonlinear ETG simulations.....90

Figure 2.13 (b): Heat flux spectrum versus $k_y\rho_s$ for nonlinear ETG simulations.....90

Figure 2.14(a): Growth rate for TEM/ETG modes at mid-pedestal locations for the DIII-D pedestals.....92

Figure 2.14(b): Frequency normalized by electron bounce frequency for TEM/ETG modes at mid-pedestal locations for the DIII-D pedestals.....92

Figure 2.14(c): $k \perp \rho s \; and \; k \perp \rho carbon$ for TEM/ETG modes at mid-pedestal locations for the DIII-D pedestals. 93
Figure 2.14(d): Ratio of ion to electron thermal diffusivity for TEM/ETG modes at mid-pedestal locations for the DIII-D pedestals. 94
Figure 2.14(e): Ratio of electron particle diffusivity to thermal diffusivity for TEM/ETG modes at mid-pedestal locations for the DIII-D pedestals. 95
Figure 2.14(f): Ratio of impurity particle to thermal diffusivity for TEM/ETG modes at mid-pedestal locations for the DIII-D pedestals. 95
Figure 2.14(g): Ratio of ion particle diffusivity to electron thermal diffusivity for TEM/ETG modes at mid-pedestal locations for the DIII-D pedestals. 96
Figure 2.15(a): Growth rate for ITG/TEM modes at top-pedestal locations for DIII-D 98889.....97
Figure 2.15(b): Growth rate and ExB shearing rate for ITG/TEM modes at top-pedestal locations for DIII-D 98889. 97
Figure 2.15(c): Frequency normalized by $k_z \, v_{th,i}$ for ITG/TEM modes at top-pedestal locations for DIII-D 98889. 98
Figure 2.15(d): Frequency normalized by ion bounce frequency for ITG/TEM modes at top-pedestal locations for DIII-D 98889. 99
Figure 2.15(e): Frequency normalized by ion diamagnetic frequency for ITG/TEM modes at top-pedestal locations for DIII-D 98889. The frequency of these modes in pedestals are much less than ω_i*. 99
Figure 2.15(f): Ratio of ion to electron thermal diffusivity for ITG/TEM modes at top-pedestal locations for DIII-D 98889. 100
Figure 2.15(g): Ratio of electron particle diffusivity to ion thermal diffusivity for ITG/TEM modes at top-pedestal locations for DIII-D 98889. 101
Figure 2.15(h): Ratio of impurity diffusivity to ion thermal diffusivity for ITG/TEM modes at top-pedestal locations for DIII-D 98889. 101

Figure 2.16 (a): The frequency normalized to ω_e* and to to $k_{\|}V_A$ for the local linear TAE/MTM in 153674/5 at ρ_t = 0.977 (base case) 103

Figure 2.16 (b): The ratio of electromagnetic to electrostatic heat flux is less than 1, which shows that the mode cannot be an MTM. Also, the $E_{\|}$ cancelation is typical of an MHD-like mode. 104

Figure 2.16(c): Growth rate for TAE/MTM modes for DIII-D 153764 base case at ρ_t = 0.977 and n=13. 105

Figure 2.16 (d): The transport fingerprints of the typical TAE/MTM mode are typical of an MTM. 105

INTRODUCTION

The tokamak H-mode is the leading contender for demonstrating high energy gain from fusion[1]. Its most important fusion relevant characteristic is its high (explicitly expressed through H) energy confinement time: τ_E = Plasma stored energy/Heating power. High τ_E is the main requirement for fusion gain, and this is expressed in the Lawson criterion[2]. The τ_E is high in H-mode because an Edge Transport Barrier (ETB) greatly reduces energy losses. Of course, some energy losses still remain, and it is these that determine how good the energy confinement actually is. An understanding of these "residual" losses, a must for a theoretical understanding of τ_E, constitutes the principal motivation as well as the primary task for this thesis.

Instabilities in the ETB (also known as the pedestal) are generally believed to be the cause of energy losses. We use gyrokinetic simulations to identify the responsible instabilities for two different types of H-modes:

1) The first pedestal to be analyzed is from Alcator C-Mod operating in what is called an I-mode, a relatively new and promising class of ETBs. This work is described in chapter one.

2) Then we analyze two conventional ELMy H-mode pedestals on DIII-D. For these cases, we emphasize a recently developed new concept, the "transport fingerprints", that associates specific transport activity with specific instabilities. This concept, together with gyrokinetic simulations, enables the identification of the modes responsible for transport in the pedestals. The hope is that if one can identify instabilities that cause, for example, anomalous energy losses, we could conceive of ways of minimizing them. This is described in chapter two.

We use the gyrokinetic code GENE and apply it to pedestal equilibria that were reconstructed by the DIII-D and the C-mod teams. Numerical MHD equilibria, from the EFIT code, were used for the magnetic geometry.

The GENE code is a well-benchmarked, very widely used gyrokinetic code[3]. Previous work applying GENE to H-mode pedestal has been performed on ASDEX-Upgrade, JET and other machines[4-8]. Our GENE simulations were varied and extensive:

1) Local linear: These are the most commonly published type of gyrokinetic simulations for pedestals. For these, instabilities are examined at one radial location in a pedestal, and variations of the equilibrium profiles are neglected. Radial direction is Fourier transformed and there's a radial wavenumber k_X and a binormal wavenumber k_Y associated with each calculation.

2) Global linear: the full profile variation of all equilibrium quantities in the pedestal is included. Radial direction in global linear simulations are implemented with finite difference method with Dirichlet boundary conditions on each side setting the perturbed electromagnetic fields and the perturbed distribution function to zero value.

3) Global nonlinear: nonlinearly saturated states of the instabilities are obtained, including the full profile variations. Important physics processes in the global nonlinear runs include: zonal flow, Geodesic Acoustic Mode, nonlinear flattening of the dynamic profiles.

We examine the physical properties of the modes, and attempt to match multiple different observations for these pedestals, including:

1) Energy losses/ power balance

2) Transport in various channels, including impurity density, electron density, and ion temperature.

3) The observed frequency and k (wave number) spectra of pedestal fluctuations

This work breaks new ground in the pedestal simulation area, in that it is the first to try to match observations, simultaneously, of transport in multiple channels, with the spectra of observed fluctuations. We have been quite successful in establishing causality between the "modes" and their transport signatures.

CHAPTER I: INVESTIGATIONS OF AN I-MODE PEDESTAL ON ALCATOR C-MOD

I-mode introduction

I-mode is a promising regime for burning plasmas. It has an edge transport barrier that gives it a high energy confinement time, as in conventional H-modes. But it has several characteristics that are superior to a conventional H-mode: 1) It avoids damaging Edge Localized Modes (ELMs) that are very problematic for ITER and proposed fusion reactors 2) It avoids the build-up of impurities in the plasma that would eventually become unacceptable. It is important to understand the physical mechanisms that operate in I-modes that give it these advantages over H-modes. The I-mode has been observed on several tokamaks, including Alcator C-Mod, DIII-D, and ASDEX-Upgrade. The C-mod tokamak has characterized this mode especially well.

The different character of the I-mode apparently stems from the different transport processes that operate in the pedestal. The energy transport seems to prevent pedestal pressure from reaching an ideal-MHD stability boundary, so that ELMs are avoided. The impurity transport seems to prevent impurity build-up. To understand the I-mode better, we have used the gyrokinetic code GENE to examine the instabilities and transport in the pedestal of a particular high performance I-mode shot on C-Mod.

The C-Mod I-mode pedestals are observed to have a unique fluctuation called a Weakly Coherent Mode (WCM). This is suspected of being at least partially responsible for the unique characteristics of the I-modes. Hence, one of the important goals of our investigation is to find instabilities in the gyrokinetic simulations which match the observed WCM, and, to clarify the physical mechanisms of the fluctuation.

Global linear simulations

We used GENE to perform "global" simulations of the pedestal (Fig. 1.1), which means that the full profile variations in the pedestal region were included. The simulation box was large enough to include the entire pedestal, as indicated below. For all GENE global runs, a "buffer" zone is included near the boundaries, where extra damping is added to ensure good numerical behavior. The radial coordinate we use in the simulations included in this dissertation is the normalized square root of toroidal flux ($\rho_t = \sqrt{\frac{\Psi_t}{\pi B_0}}$).

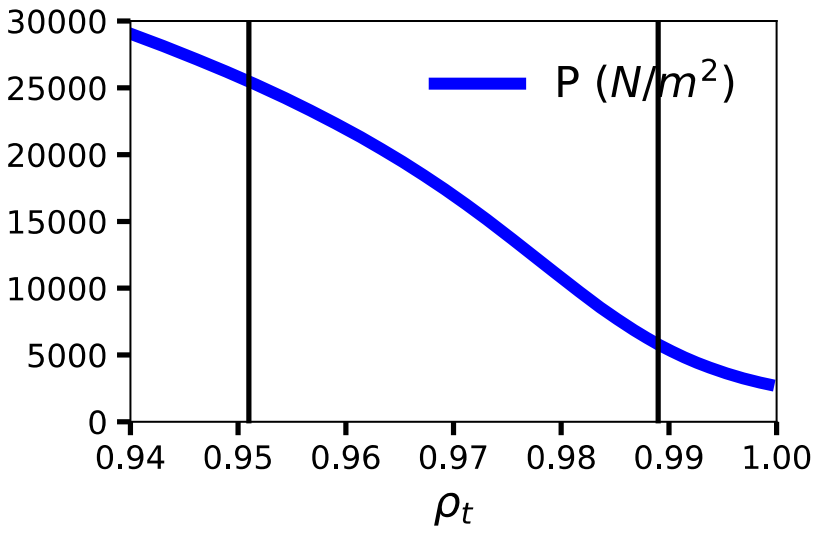

Figure 1.1: Pressure profile and simulation box.

We conduct simulations based on the experimental profiles of T_e, T_i, n_e, n_i and E_r, and the kinetic EFIT files containing the reconstructed MHD equilibrium. For the shot being analyzed, the impurity Z_{eff} is estimated to be 2.8, and the averaged impurity charge Z_{avg} is 10, but there's no direct measurement of the impurity profile. As a starting point, n_i and n_z profiles are so constructed that Z_{eff} is constant across the pedestal. The instabilities found in GENE global simulations, for the toroidal wavenumbers where peak WCMs are observed, are shown in Table 1.1.

Toroidal mode number (n)	Growth rate $\gamma(c_s/a)$	Frequency in lab frame (kHz)	Averaged ExB Doppler shift (kHz)	χ_i/χ_e	D_e/χ_i	D_Z/χ_i	Q_{es}/Q_{em}	$<E_{\|\|}>$	$E_{\|\|,em}/E_{\|\|,es}$
15	0.079	-271.67	-255.74	2.65	0.034	1.4	-25.79	0.96	0.029
16	0.081	-291.06	-273.03	2.58	0.046	1.41	-26.33	0.97	0.025
17	0.082	-310.13	-290.32	2.5	0.055	1.42	-24.3	0.97	0.024
18	0.085	-329.21	-308.14	2.41	0.064	1.42	-22.48	0.98	0.018
19	0.087	-348.49	-325.96	2.34	0.077	1.43	-21.43	0.97	0.023

Table 1.1: Toroidal mode number scan result.

The mode frequencies in the lab frame, where WCM density and magnetic fluctuations are measured to peak, are found to be in the 300 - 400 kHz range. Most of the frequency is due to ExB Doppler shift arising from the radial electric field E_r-well in the pedestal. This is consistent with ITG, since in the plasma frame, the frequency of ITG is, typically, a small fraction of ion diamagnetic frequency (ω_i^*). It could also be possibly consistent with resistive ballooning mode or TEM.

The ion thermal transport is the dominant transport channel affected by this mode. The ratio of the induced ion to electron thermal diffusivity (χ_i/χ_e) is around 2.5. The mode is essentially electrostatic. The ratio of the diffusivity in different channels, which we call the transport "fingerprints", are typical ITG mode fingerprints. We will explain the physic basis of these in more detail in Chapter II. In contrast, MHD-like modes, (which are electromagnetic, and have an inductive $A_{||}$ field to cancel $\nabla_{||}\phi$), generally have similar diffusivities of all quantities (i.e., $\chi_e/\chi_i \sim 1$, $D_e/\chi_i \sim 2/3$, and $D_Z/\chi_i \sim 2/3$).

ION TEMPERATURE GRADIENT SCALE LENGTH (A/L_{T_I}) SCAN

In order to probe further into the nature of the mode, we vary the T_i profile while keeping the other profiles the same. New T_i profiles are made according to the formula,

$$T_i(\rho_t) = T_i(\rho_t = 0.97) \cdot \left[\frac{T_i(\rho_t)}{T_i(\rho_t = 0.97)}\right]^{\alpha}$$

where α = 0.8, 0.9, 1.1 or 1.2. The ion temperature is unchanged at the middle of the pedestal (ρ_t = 0.97). In this way, the normalized ion T gradient scale length, a/L_{Ti}, is varied by a factor of α. Global linear simulations (Table 1.2) find the growth rate of this mode to increase as T_i gets steeper and becomes stable when it becomes less steep (i.e, when a/L_{Ti} is 0.8 times the observed value, the growth rate drops and the dominant instability goes into an ETG mode).

a / L_{Ti} factor	Growth rate $\gamma(c_s/a)$	Frequency in lab frame (kHz)	Averaged ExB Doppler shift (kHz)	χ_i / χ_e	D_e/χ_i	D_z / χ_i	Q_{es}/ Q_{em}	$<E_{\|\|}>$	$E_{\|\|,em}/E_{\|\|,es}$
1.2	0.165	-320.93	-305.00	2.9	0.014	1.16	-17.27	0.98	0.02
1.1	0.127	-325.02	-307.09	2.67	0.039	1.28	-18.52	0.98	0.019
1	0.085	-329.21	-308.14	2.41	0.064	1.42	-22.48	0.98	0.018
0.9	0.033	-333.61	-309.19	2.16	0.1	1.57	-42.45	0.98	0.016
0.8	0.032	-233.83	-246.30	0.44	-0.1	1.86	-19.47	0.94	0.055

Table 1.2: Ion temperature gradient scale length variation result.

Thus, the ion temperature gradient is a significant drive for this mode.

The simulations find that the poloidal structure of this mode (Fig 1.4) is unlike most modes found in the core; it doesn't peak at the outboard midplane (z = 0 is outboard midplane). Radially, the mode peaks at the outer wall of the E_r-well (bottom of the E_r-well is at ρ_t = 0.97) where η_i drive is large enough to overcome shear suppression (γ_{ExB}) (see Fig 1.2 for η_i profile and Fig 1.3 for γ_{ExB} profile). More to the edge, shear suppression becomes too large for the mode to grow while near the core, η_i is not strong enough. Eigenfunctions from global linear simulation (a typical eigenfunction of ϕ shown in Fig 1.4) are consistent with experimental observation of the mode's location.[9]

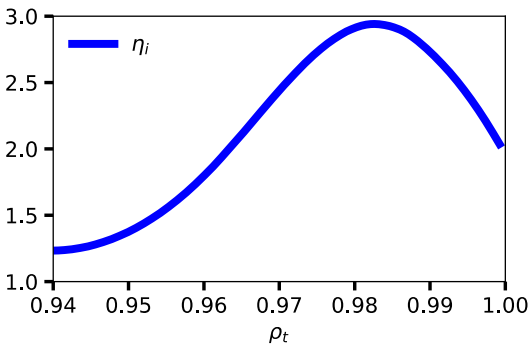

Figure 1.2: η_i profile in the pedestal region.

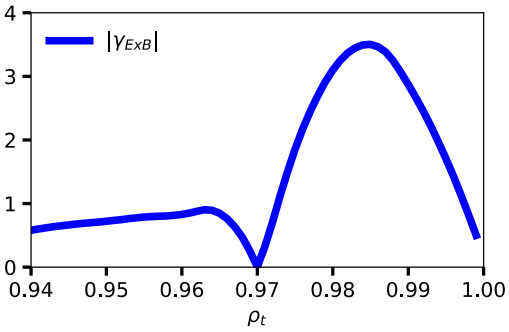

Figure 1.3: Absolute value of γ_{ExB} from experimental Er profile in the pedestal region.

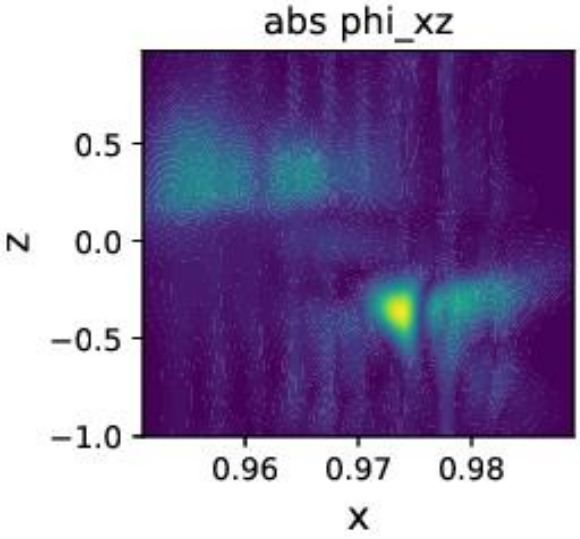

Figure 1.4: Mode structure of the electrostatic potential (ϕ) in a typical global simulation.

DENSITY GRADIENT SCALE LENGTH (A/L_{NE}) SCAN

The next parameter scan is that of the density gradient. Density profiles of all three simulated species are varied together to satisfy quasi-neutrality, and constant Z_{eff} (= 2.8). We also keep total pressure unchanged from the experimental profiles by modifying the temperature profiles accordingly. With total pressure the same, pressure gradient drive of MHD-like modes is kept constant.

a/L_{ne} factor	Growth rate $\gamma(c_S/a)$	Frequency $\omega(c_S/a)$	χ_i/χ_e	D_e/χ_i	D_z/χ_i	Q_{es}/Q_{em}	$\langle k_z \rangle$ ($\lvert\phi\rvert^2$ averaged)
0.8	0.181	-3.031	2.73	-0.07	0.99	-16.85	0.24
0.9	0.136	-3.088	2.62	0.005	1.19	-18.08	0.25
1	0.085	-3.141	2.41	0.064	1.42	-22.48	0.25
1.1	0.017	-3.189	1.97	0.14	1.59	-62.81	0.25
1.2	-0.004	-3.34	2.55	0.1	2.21	128.2	0.31

Table 1.3: Density gradient scale length variation result. k_z is the mode wavenumber along the magnetic field line.

As expected, the growth rate decreases when the density gradient is increased (see results in Table 1.3); the mode becomes stable when a/L_{ne} is 20% above the experimental value. This provides additional evidence that we are dealing with an ITG mode driven by η_i; a pressure gradient driven MHD-like mode would not be stabilized. After computing the mode wavenumber k_z (along the magnetic field line) from the eigenfunction ϕ, we find that the mode frequency in the plasma frame, is close to $k_z v_{th,i}$, *indicating that ion thermal resonance is important for this instability*. Kinetic treatment is therefore, necessary in identifying/explaining this mode. This could be the reason why the fluid treatment of Liu et. al. did not find this mode[10]. Passing electrons, however, could be considered adiabatic since $k_z v_{th,e}$ is much larger than the mode frequency. Adiabatic electron response would explain why D_e/χ_i is small for this mode.

COLLISIONALITY SCAN

Experiments found that I-mode discharges have low collisionality pedestals ($\nu^*_{95} \sim 0.1$) compared to H-mode with the same pedestal temperature[11] and WCM signal is clearest on diagnostics in low ν^* pedestals[12]. To study the effects of pedestal collisionality on the mode's growth rate, new profiles are created by multiplying the temperature profile by a given factor and dividing the density profile by the same factor. In this way, collisionality is modified while total pressure is kept constant and consistent with the MHD equilibrium in the EFIT file. (Note that the GENE simulations use the 'Sugama' collision operator whenever possible, which has the best numerical properties).

Collisionality factor	Growth rate $\gamma(c_S/a)$	Frequency $\omega(c_S/a)$	Frequency in plasma frame $f_{pl}(c_S/a)$	$\langle\nu_{ei}\rangle$	$\nu_{eff}/\lvert\omega_{pl}\rvert$	$\langle\omega_{bounce,e}\rangle$	$\langle\nu^*\rangle$
0.1	0.109	-1.216	0.396	0.272	1.69	6.434	0.108
0.8	0.09	-2.977	-0.177	1.297	16.63	4.441	0.744
1	0.085	-3.141	-0.202	1.630	18.94	4.329	0.959
1.2	0.081	-3.278	-0.223	1.974	21.19	4.256	1.181
2	0.077	-3.593	-0.281	3.03	26.44	4.148	1.859
4	0.074	-4.077	-0.34	5.83	42.82	4.099	3.621

Table 1.4: Collisionality scan result.

In Table 1.4, electron bounce frequency is $\omega_{bounce,e} = \sqrt{\epsilon}\frac{v_{th,e}}{qR}$ and $\langle\ldots\rangle$ denotes weighted average by eigenfunction ϕ. f_{pl} is the frequency of the mode in the plasma frame in normalized units. $|\omega_{pl}|$ is the absolute value of the complex frequency of the mode in the plasma frame.

By changing collisionality from the experimentally observed value, we found that the modes tend to become slightly more stable at higher collisionality. This is in contrast with the resistive ballooning mode that has a higher growth rate at higher collisionality. To quantify the importance of collisions for the trapped electrons, we normalize ν_{eff} ($\nu_{eff} = \nu_{ei}$

/ε , is the collisional electron de-trapping rate, as in neoclassical theory) by the absolute value of the complex frequency of the mode in the plasma frame, $\nu_{eff}/|\omega_{pl}|$. Since this value for the experimental profile is much larger than 1 (~ 20), it means that collisions detrap electrons much more frequently than mode frequency of this mode. Hence trapped electron effect is weak. Note that mode frequency in plasma frame is much smaller than electron bounce frequency. Even though ν^* is on the order of 1, the relevant definition of collisionality for this mode, $\nu_{eff}/|\omega_{pl}|$, show that this regime is too collisional for the trapped electrons to be a dominant effect on this instability.

This also indicates that the non-adiabatic trapped electron effects are small. Since both passing and trapped electron non-adiabaticity is weak, it follows that the electron particle transport is weak for this mode, i.e., D_e/χ_i is small.

Hence this is a slab-like ITG where curvature drive and trapped electron drive is not of primary importance.

IMPURITY DENSITY GRADIENT (A/L_{NZ}) SCAN

Since impurity density profile (difficult to measure in the experiment) is known to affect the instability of ITG, we run simulations to probe the sensitivity of this factor and look for the most probable impurity density n_Z profile in the steady state. (There's proposal in the literature that an impurity mode could explain WCM[13]). In our scan of the gradient of the impurity density profile, we go from one extreme to the other – form a flat profile to one slightly steeper than the electron density profile. The electron density profile is fixed at the measured value, and main ion density profile is adjusted accordingly to satisfy quasi-neutrality. This shows that low impurity density n_Z gradient, destabilizes the mode. (Note that, since n_e decreases as the LCFS is approached, but n_Z is nearly constant, Z_{eff} is rising toward the LCFS). This destabilizing trend is consistent with the effect of impurities on ITG[14].

a / L_{nz} factor	Toroidal mode number (n)	Growth rate $\gamma(c_s/a)$	χ_i/χ_e	D_e/χ_i	D_z/χ_i	Q_{es}/Q_{em}	$<E_{\|\|}>$	$E_{\|\|,em}/E_{\|\|,es}$
0	18	0.168	2.56	0.01	-∞	-18.67	0.98	0.019
0.2	18	0.154	2.55	0.016	-0.9	-19.1	0.98	0.018
0.3	18	0.147	2.54	0.021	0.066	-19.4	0.98	0.018
0.4	18	0.139	2.54	0.027	0.55	-19.74	0.98	0.018
0.8	18	0.103	2.47	0.052	1.28	-21.46	0.98	0.018
1	18	0.085	2.41	0.064	1.42	-22.48	0.98	0.018
1.2	18	0.065	2.35	0.076	1.52	-23.5	0.98	0.018

Table 1.5: Impurity density gradient scale length variation result.

The ion thermal diffusivity is used to normalize particle diffusivities to get a dimensionless value that reflects the mode's relative transport strength in different channels. We compute the "effective" particle diffusivity by dividing the quasilinear particle flux by the density gradient. We don't split the diffusive term (D dn/dx) and the inward pinch term (Vn) in the particle fluxes because there's no clear procedure to do this for instability caused transport. Therefore, if inward pinch dominates, we would have a negative value for the effective particle diffusivity.

The impurity particle diffusivity is found to be very sensitive on impurity density gradient. When a/L_{nz} is equal to or slightly larger than a/L_{ne}, the ratio of impurity particle diffusivity to ion thermal diffusivity (D_z/χ_i) could be as high as ~ 1.5. This implies that this mode is an effective channel in expelling impurities and flattening impurity density gradient if impurities accumulate inside the pedestal. The value a/L_{nz} is reduced to be a small fraction of a/L_{ne} to reveal the pinch term, since the effective impurity particle diffusivity becomes negative, indicating a weak inward impurity pinch caused by this mode. In a steady-state discharge such as I-mode, since there's no significant impurity particle source inside the plasma, the flux of impurity particles must be close to zero. Therefore, based on the quasilinear particle flux from these linear simulations, the most

probable impurity density profile, based on the D_z/χ_i produced by the mode, is the one with $a/L_{nz} \sim 0.3 * a/L_{ne}$, where a/L_{ne} is the observed electron density profile scale length.

SUMMARY OF CONCLUSIONS FOR THE DENSITY TRANSPORT

This results above are fully consistent with the observed electron density profile. The density gradient at which D_e/χ_i goes to zero is with the density profile modification that makes $a/L_{ne} \sim 0.9$ times the observed value, i.e., very close to the experimental value in steady-state. The results above can be interpreted as showing that the low particle loss for this mode is sustained by a small outward diffusion and small inward pinch. (This is consistent with the small particle source inferred for I-mode.)

We found that, as impurity density gradient (a/L_{nz}) and ion temperature gradient (a/L_{Ti}) is varied, this mode has a low ratio of electron particle diffusivity to ion thermal diffusivity (D_e/χ_i). This is to be expected since particle transport only appears when electrons are non-adiabatic. As is described above, the passing electrons are adiabatic because $k_z\, v_{th,e} >> \omega$. Trapped electron effect is weak because they are detrapped by collisions ($\nu_{eff}/|\omega_{pl}| > 1$). In addition to that, ϕ doesn't peak at outboard midplane where electrons were trapped, which further reduces the coupling of this mode to trapped electrons. *Low particle transport is therefore unavoidable consequence of the basic physics of this mode.*

We now examine the consistency of this observation with experimental inferences.

DIFFUSIVITY INFERENCES BASED ON EXPERIMENTAL PROFILES AND SOURCES

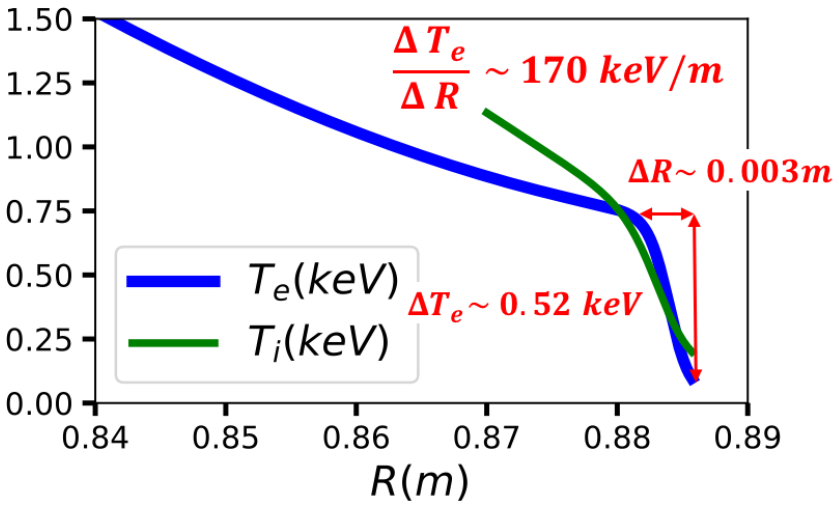

Figure 1.5: Electron and ion temperature profiles in the pedestal region.

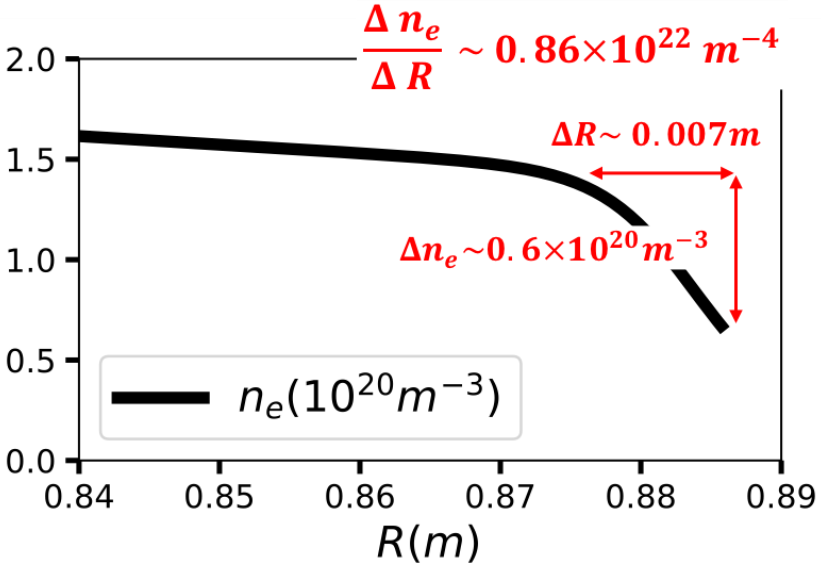

Figure 1.6: Electron density profile in the pedestal region.

We estimate the pedestal thermal diffusivity using the energy flux through the last closed flux surface (LCFS), and the electron temperature gradient in the pedestal. The energy flux through the pedestal is estimated using $P_{Net} = P_{ICRF} + P_{Ohmic} - P_{Radiation} \sim$ 4 MW and surface area ($A \sim 7\ m^2$):

$$Q \sim \frac{P_{heating}}{A_{LCFS}} = \frac{4 \times 10^6\, W}{7\, m^2} \sim 0.57 \times 10^6\, Wm^{-2}$$

The electron density in the middle of the pedestal and the average temperature gradient are, respectively, estimated as $n_e \sim 1.0 \times 10^{20}\ m^{-3}$, and $\frac{\Delta T_e}{\Delta R} \sim 170\ keVm^{-1}$, $\frac{\Delta T_i}{\Delta R} \sim \frac{1}{2}\frac{\Delta T_e}{\Delta R}$ (See the Fig 1.5 and Fig 1.6). If the electron thermal diffusivity dominates, the thermal diffusivity is found to be $\chi^{eff} = 0.2\, m^2 s^{-1}$; if the electron and ion thermal diffusivities are the same, the thermal diffusivity is found to be $\chi^{eff} = 0.13\, m^2 s^{-1}$.

If $\chi_e \gg \chi_i$,

$$Q = \chi^{eff}\, n\, \frac{dT_e}{dR} \sim \chi^{eff}\, n\, \frac{\Delta T_e}{\Delta R}$$

$$\chi^{eff} = \frac{Q}{n\frac{\Delta T_e}{\Delta R}} = \frac{0.57 \times 10^6\, Wm^{-2}}{1.0 \times 10^{20}\, m^{-3} \times 170\, keVm^{-1}} \sim 0.2\, m^2 s^{-1}$$

If $\chi_e = \chi_i$,

$$Q = \chi^{eff}\, n\, \left(\frac{dT_e}{dR} + \frac{dT_i}{dR}\right) \sim \chi^{eff}\, n\, \left(\frac{\Delta T_e}{\Delta R} + \frac{\Delta T_i}{\Delta R}\right)$$

$$\chi^{eff} = \frac{Q}{n\left(\frac{\Delta T_e}{\Delta R} + \frac{\Delta T_i}{\Delta R}\right)} = \frac{0.57 \times 10^6\, Wm^{-2}}{1.0 \times 10^{20}\, m^{-3} \times 1.5 \times 170\, keVm^{-1}} \sim 0.13\, m^2 s^{-1}$$

We estimate the effective electron particle diffusivity (D_e^{eff}) using the particle flux through the LCFS, and the electron density scale length in the pedestal region. The shot we analyze, here, has plasma current of Ip = 1.2 MA. Then, from Table 5.1 in Dominguez Ph.D thesis[15], the electron particle flux through the LCFS, Γ_{LCFS} is calculated, based on measurements, to be $\Gamma_{LCFS} = 1.2 \times 10^{20} \sim 1.5 \times 10^{20}\ m^{-2}s^{-1}$. The shot we analyze here has somewhat more gas puffing than in the Dominguez data set, nonetheless, we use his estimate as the best that is available. We estimate the average density gradient to be $0.86 \times 10^{22}\ m^{-4}$ (See the Fig 1.6). The effective electron particle diffusivity (D_e^{eff}), found to be in the range $D_e^{eff} = 0.014 \sim 0.017\, m^2 s^{-1}$, is over an order of magnitude smaller than the effective thermal diffusivity,

$$\Gamma_{LCFS} = D_e^{eff}\, \frac{dn_e}{dR} \sim D_e^{eff}\, \frac{\Delta n_e}{\Delta R}$$

$$D_e^{eff} = \frac{\Gamma_{LCFS}}{\frac{\Delta n_e}{\Delta R}} = \frac{1.2 \times 10^{20} \sim 1.5 \times 10^{20}\, m^{-2}s^{-1}}{0.86 \times 10^{22}\, m^{-4}} = 0.014 \sim 0.017\, m^2 s^{-1}$$

It should be noted that there is significant uncertainty as to the particle source in this shot. Nonetheless, it seems to us, that the order of magnitude of the difference between D_e^{eff} and χ^{eff} make it difficult to conclude anything other than D_e^{eff} is considerably smaller than χ^{eff}, which is at least qualitatively consistent with the basic physics of the mode we find.

Total impurity flux out from the LCFS (Γ_z) is evaluated by dividing the total impurity particles inside by the impurity confinement time and the LCFS area. The former is obtained by multiplying the average impurity density in the core by the volume within the LCFS ($V \sim 0.88\ m^3$), while the impurity confinement time is estimated to be $\tau_z \sim 30$ ms.[16]

$$\Gamma_z = \frac{V \cdot n_{z,core}}{\tau_z \cdot A_{LCFS}}$$

Another way of computing the impurity flux is through using the pedestal diffusivity,

$$\Gamma_z = D_z \frac{dn_z}{dx} \sim D_z \frac{n_{z,ped}}{2\, w_{ped}}$$

Since the core impurity profile is flat, we assume that the impurities are mainly confined by the pedestal. Therefore, the two ways of calculating impurity flux should be equal,

$$\frac{V \cdot n_{z,core}}{\tau_z \cdot A_{LCFS}} = D_z \frac{n_{z,ped}}{2\, w_{ped}} \Longrightarrow D_z \geq \frac{V \cdot 2\, w_{ped}}{\tau_z \cdot A_{LCFS}}$$

Here we assume $n_{z,core} \geq n_{z,ped}$ and scale length of the impurity density profile to be same as the electron density scale length: $w_{ped} \sim 0.01$ m. We find the lower bound of $D_z^{eff} >= 0.08\ m^2 s^{-1}$. This means that the impurity particle diffusivity is several times higher than the electron particle diffusivity.

As we will see below, our nonlinear simulations reach this same conclusion. In particular, they are able to reproduce the relatively short impurity lifetime observed in laser blow-off experiments in I-modes on C-mod.

GLOBAL SIMULATION GRID CHOICE AND CONVERGENCE TEST

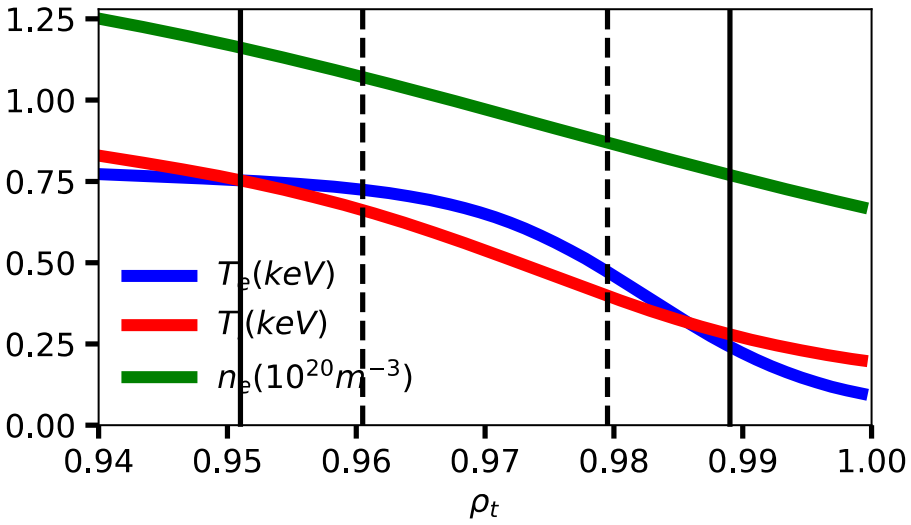

Figure 1.7: T_e, T_i, n_e profiles and simulation box. Black vertical lines indicate the boundaries of simulation box. Black dashed lines indicate the edges of buffer zone on each side.

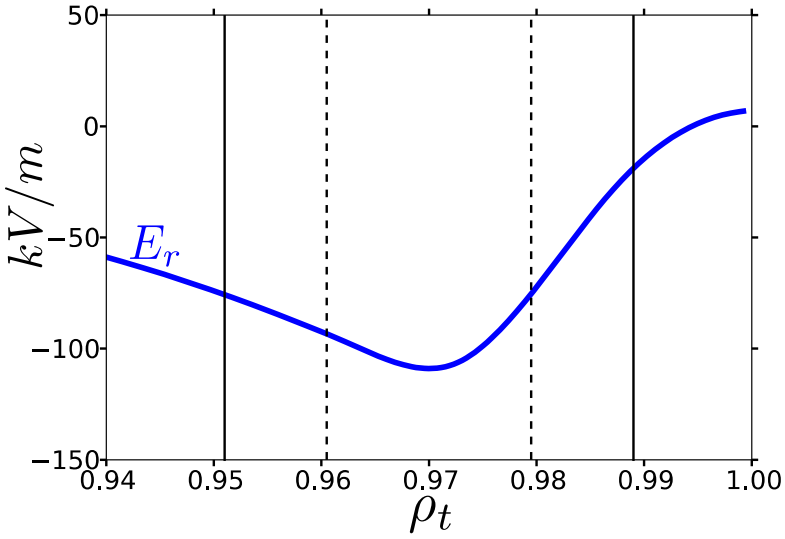

Figure 1.8: E_r-well and simulation box. Black vertical lines indicate the boundaries of simulation box. Black dashed lines indicate the edges of buffer zone on each side.

Now we will explain some technical aspects of our simulation. The radial simulation box, centered at $\rho_t = 0.97$ (location of the E_r-well bottom), extends between $\rho_t \sim (0.95, 0.99)$; the simulation box is about 16 gyroradii (16 ρ_s) wide. The actual simulation

zone lies between ρ_t ~ (0.96, 0.98) flanked by a buffer zone of width $\Delta\rho_t$ ~ 0.01 on each side.

Global simulations are done on a simulation grid of (128, 72, 48, 32) in terms of (nx, nz, nv, nw). The desirable number of grid points in each dimension is determined by performing convergence tests, increasing resolutions in x, z, and velocity space (v and w) by 1.5 times each. The results are summarized in the table below. Since the growth rates and frequencies found in higher resolution runs don't deviate from the original case by more than 10%, we decide to use the original resolutions.

nx	nz	nv	nw	Growth rate $\gamma(c_S/a)$	Frequency $\omega(c_S/a)$
128	72	48	32	0.085	-3.141
192	72	48	32	0.084	-3.142
128	72	72	48	0.090	-3.124
128	108	48	32	0.082	-3.152

Table 1.6: Convergence test results.

Nonlinear global simulations

Having identified the dominant instability, we turn to nonlinear global simulations to work out its nonlinear consequences, in particular, the transport caused by the ITG/Impurity mode. The idea is to compare it to the experimental input power of this shot: $P_{Net} = P_{ICRF} + P_{Ohmic} - P_{Radiation}$ ~ 4 MW.

Note that these nonlinear simulations include the full kinetic dynamics of n=0 perturbations. In particular, they include zonal flows, Geodesic Acoustic Modes and other acoustic modes, and local profile modifications. They do not include multi-scale interactions of ETG modes and ion-scale modes. Simulations that include multi-scale effects are extremely computationally expensive and are left to future work.

CONVERGENCE TEST

Linear global simulation results show that the ITG/impurity is unstable for a continuum of toroidal mode numbers. Since it consumes too much computational time to run a nonlinear global simulation including every mode number, we do a convergence test on the wavenumber intervals and the range of wavenumbers to use in nonlinear simulations for the results to be valid.

We start by using an interval of $\Delta n = 4$, and test 10 (16) toroidal mode numbers. The resulting simulation grid will span mode numbers [0, 4, 8, …, 36] ([0, 4, 8, …, 60]). With the set of profiles having the same density gradient for all species, the total heat loss from the 10 mode number simulation is 0.08 WM (0.05 WM from ions, 0.03 WM from electrons, and 0 WM from the impurities), while the total heat loss from the 16 case increases to 0.14 WM (0.07 WM from ions, 0.06 WM from electrons, and 0.01 WM from the impurities). Time evolution of these two runs are shown in Fig 1.9.

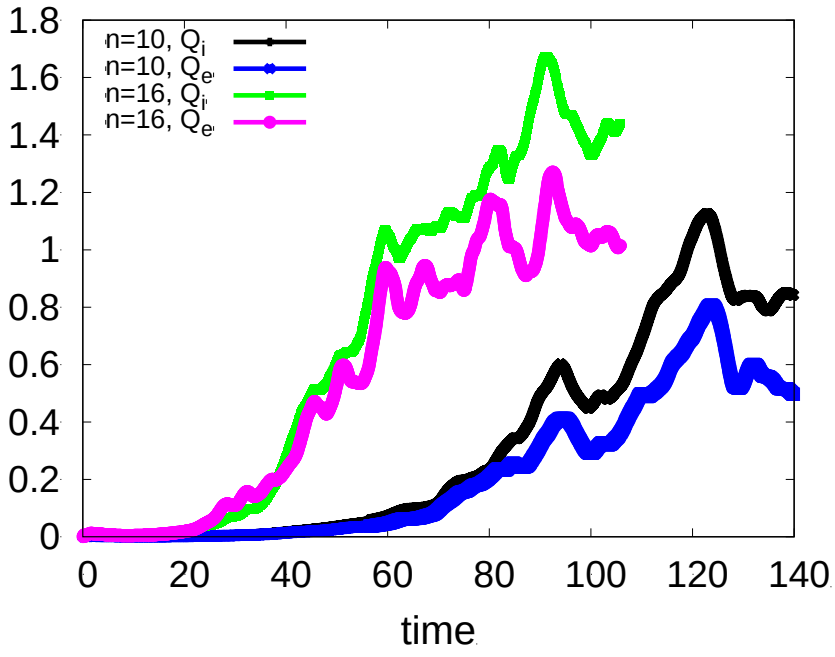

Figure 1.9: Time series plot of electrostatic heat loss for ion scale nonlinear simulations. 10 mode number simulation is shown in black for ion heat loss, and blue for electron. 16 mode number simulation is shown in green for ion heat loss, and magenta for electron.

Next, we test if extending toroidal mode number grid affects the simulation results. We increase the mode number interval from $\Delta n = 4$ to $\Delta n = 6$, keeping the total number of mode numbers the same. The new toroidal mode number grid in the simulation becomes [0, 6, 12, 18, …, 90]. As can be seen from Fig 1.10, heat spectrum increases toward higher k_y for both cases. This could indicate the simulation is not fully numerically resolved and should include even higher k_y modes. However, the lack of separation of ion-scale and electron-scale turbulence is often what happens for ion scale nonlinear simulations with strong ETG drive, as is certainly true for I-mode. Since total heat loss is the same between these two grids for this test, we decide to use $\Delta n = 4$ as the standard grid spacing.

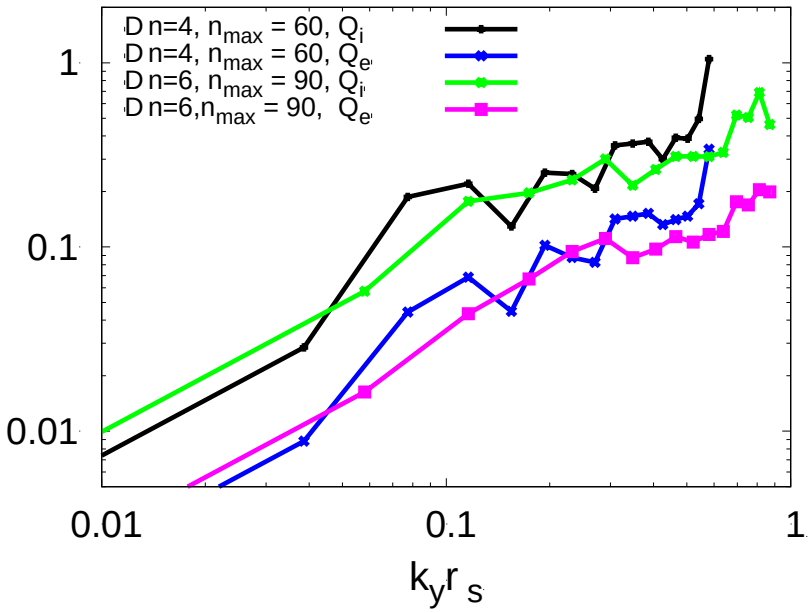

Figure 1.10: Spectra of electrostatic heat loss for ion scale nonlinear simulations. $\Delta n = 4$ simulation is shown in black for ion heat loss, and blue for electron. $\Delta n = 6$ simulation is shown in green for ion heat loss, and magenta for electron.

NONLINEAR ITG/IMPURITY THERMAL TRANSPORT

With the set of parameters determined, we move on to compute the total heat loss from this instability. Radial profile of heat loss for three impurity profiles are shown in Fig 1.11 and Fig 1.12. As an upper bound, the largest amount of heat loss found in the nonlinear

runs is with the profile where impurity profile is flat ($a/L_{nz} = 0$). It also has the highest linear growth rate in the a/L_{nz} scan above. For this case, peak heat loss is ~ 0.65 MW (0.5 MW from ions, 0.15 MW from electrons). Peak heat loss for the impurity profile (a/L_{nz} ~ 0.4 * a/L_{ne}) which is close to what we think is steady state is ~ 0.45 MW (0.35 MW from ions, 0.1 MW from electrons). Since the total net power coming into pedestal for this shot is about 4 MW, ITG/Impurity mode is an order of magnitude too low to match power balance.

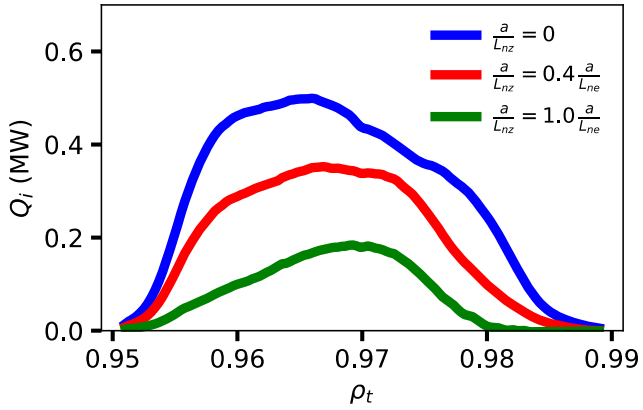

Figure 1.11: Radial profile of ion electrostatic heat loss for simulations using different impurity profiles.

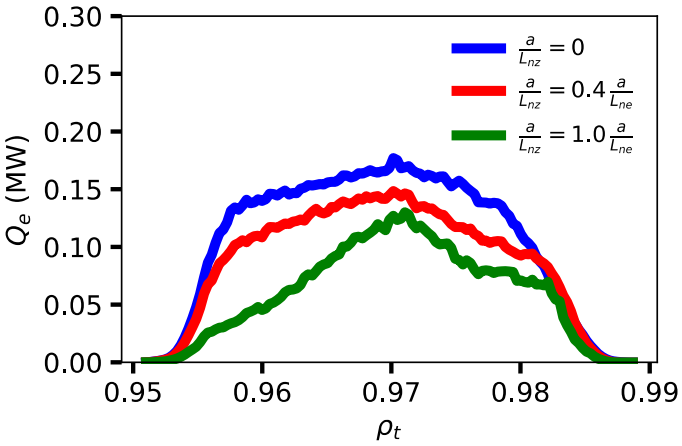

Figure 1.12: Radial profile of electron electrostatic heat loss for simulations using different impurity profiles.

NONLINEAR ETG THERMAL TRANSPORT

We run local nonlinear ETG simulations to find the heat loss from electron scale turbulence. In the nonlinear ETG simulations described here, the main ion and impurity species are assumed adiabatic and their effect enters into the simulation in the parameter τ, $\left(\tau = z_{eff} \cdot \frac{T_e}{T_i}\right)$. In the following sections, convergence test is presented, followed by heat loss from ETG turbulence at several locations in the pedestal. The dependence of heat loss from ETG turbulence on τ and η_e is also discussed.

ETG convergence test

nz	edge_opt	Other params	Q_{es} (MW)
384	2		1.34
384	4		1.33
384	6		1.37
512	2		1.44
512	6	nky*2, ky/2	1.52
512	6	nx*1.5, lx*1.5	1.57
768	6		1.4
1024	2		1.55
1024	6		1.47
1248	6		1.55

Table 1.7: Nonlinear ETG simulation convergence test.

We notice that the mode structure of nonlinear ETG simulations of I-mode pedestal, eigenfunctions develop fine structure in the z dimension (slab-like). We run a series of simulations increasing the number of grid points in the z dimension to find out an optimum number to use. Additionally, we tried to use different values of the *edge_opt* parameter to adjust the locations of grid point in z – the higher the value, the more crowded grid points are at the outboard midplane. The results are in Table 1.7. The total heat flux slightly increased with larger number, the effect is not significant.

In terms of resolution in other dimensions, we used $k_y\rho_s$ = 5, nky = 48 and lx = $2.9\rho_s$, nx = 128 as the base case parameters. To test y dimension parameters, one simulation with $k_y\rho_s$ = 2.5, nky = 96 is run for nz = 512 without finding a significant change in total heat loss. To test x dimension parameters, one simulation with nx = 192 and lx = $4.5\rho_s$ is run and it also produced similar amount of total heat loss compared to the base case.

Based on these convergence tests, we choose to use nz = 512, kymin = 2.5, nky = 72 for the nonlinear ETG runs at different radial location, and do a τ, and an η_e scan.

Radial profile of parameters and heat loss

The local nonlinear ETG simulations are conducted for 4 chosen radial locations: ρ_t = 0.97 is at the top of the electron temperature (Te) pedestal; ρ_t = 0.975 is where we see ITG/Impurity mode to peak for WCM related toroidal mode numbers; and ρ_t = 0.985 is about where the middle of electron pressure pedestal is.

We use Zeff = 2.8 to start with for all radial positions. Since Ti / Te >~ 0.8 for ρ_t = 0.97, 0.975 and 0.98, the parameter τ is as high as ~ 3.4 for these locations.

As is shown in Table 1.8, The ETG caused heat flux at ρ_t = 0.98 and 0.985 is, respectively, 3.7 MW and 7.2 MW. These values of heat flux are close to (or higher than) the input power through the pedestal (~ 4 MW).

ρ_t	$\hat{s}$	η_e	τ	Q_{es} (MW)
0.97	4.23	1.74	3.38	0.1
0.975	3.58	2.86	3.45	1.0
0.98	3.42	4.32	3.30	3.7
0.985	4.99	5.75	2.88	7.2

Table 1.8: Radial location scan of heat loss from nonlinear ETG simulations.

τ dependence

As mentioned above, we define the parameter $\tau = z_{eff} \cdot \frac{T_e}{T_i}$, which determines the strength of the adiabatic ion response in ETG simulations. The two factors making up this parameter are both hard to measure accurately in the experiments. We therefore run a set of cases at ρ_t = 0.975 to determine the τ dependence of the total heat loss; the heat loss goes up from 1. 0MW to 1.26 MW when τ goes down from 3.45 to 1.0 (Table 1.9).

τ	Q_{es} (MW)
1.	1.26
2.8	1.11
3.45	1.0

Table 1.9: τ scan of heat loss from nonlinear ETG simulations at ρ_t = 0.975.

η_e dependency

ρ_t	η_e	Q_{es} (MW)
0.97	1.74	0.1
0.97	2.09	0.3
0.975	3.58	1.0
0.975	3.43	1.8

Table 1.10: η_e scan of heat loss from nonlinear ETG simulations at ρ_t = 0.97 and 0.975.

We increase η_e by 20% for the two radial locations, ρ_t = 0.97 (ρ_t = 0.975), where nominal ETG nonlinear heat loss is enough (a little lower than) to satisfy power balance. The heat loss is boosted up 3 (2) times the nominal η_e value. This ETG heat transport in the pedestal is, therefore, stiff and is in the right range to match power balance (with a minor contribution from the ITG/impurity mode).

In summary, ETG turbulent transport can, in principle, match power balance for this shot in the middle of the pedestal (Fig 1.13).

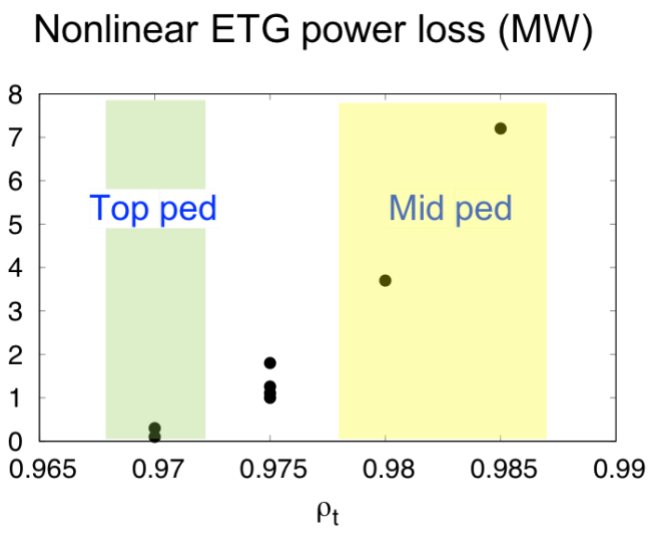

Figure 1.13: Nonlinear power loss (MW) from ETG turbulence. Results from η_e scan and τ scan are also added to the graph.

IMPURITY CONFINEMENT TIME

High Z impurity laser blow-off experiments[16] show that the core impurity transport is anomalous (D_z^{eff} >> D_{nc}) for I-modes. Experiments also find the following scalings of the impurity confinement time (τ_z) with plasma parameters: τ_z increases with plasma current and decreases with input ICRF power. The I-mode case we simulated (IM_s), has Ip = 1.2 MA, and P_{ICRF} = 5 MW. The experimental point, closest to IM_s, has τ_z ~ 30 ms. The IM_s has higher power and slightly higher current. The experimental scaling, then, will predict that these two effects are likely to roughly cancel. Therefore, we estimate the impurity confinement time to τ_z ~ 30 ms. (Note that this is on the same scale of energy confinement time[11].)

In the impurity injection experiments, one encounters two types of impurities: the intrinsic population, and externally injected impurities from the laser blow-off. The average charge of the intrinsic impurities is estimated to be Z_{ave} = 10. The laser injected Calcium happen to have about the same charge for pedestal temperatures in this shot. Hence our pedestal simulations assume only a single impurity species of Z = 10. We model the

impurity injection experiments as follows: for t < 0 we presume that the pedestal plasma is at a steady state with no impurity flux; at t = 0, the impurities are injected to raise the impurity density at the top of pedestal and inside in the plasma core. The experiment observe that impurity profile is flat in the core[16] and we assume that as well. However, the impurity density at SOL is assumed to be unperturbed during the decay phase of impurity injection. This is reasonable since impurity life time in the SOL is extremely short and the SOL impurity density is determined by the balance of rapid loses due to parallel motion and impurities source due to sputtering from plasma facing components. These processes are extremely complex and effectively impossible to calculate accurately. However, it is reasonable to assume that the SOL impurity density is essentially unperturbed by the laser blow-off since the impurities introduced by laser will be very rapidly flushed out from the SOL. Hence the ambient impurity density in SOL will not be strongly affected.

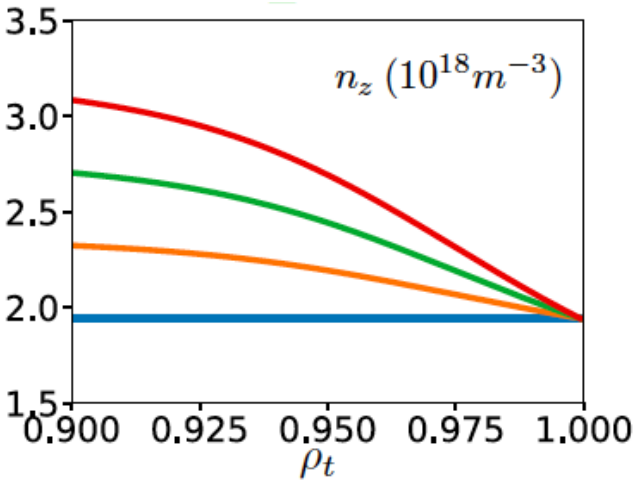

Figure 1.14: Impurity profiles in the pedestal for the simulations designed to estimate impurity confinement time.

We designed a set of impurity profiles (Fig 1.14) to reproduce the decay phase of impurity injection in laser blow-off experiments. It is assumed that the impurity density at the SOL is same for all. The effect of impurity laser blow-off, therefore, is to boost up the impurity density gradient in the pedestal $n_{z,\,ped}$ since the impurity density in the pedestal

(and inside) increases while the separatix density remains essentially unperturbed. We use nonlinear simulation, then, to calculate the increased impurity flux from this boosted gradient and go on to calculate the core impurity decay rate for comparison with experimentally measured decay rate.

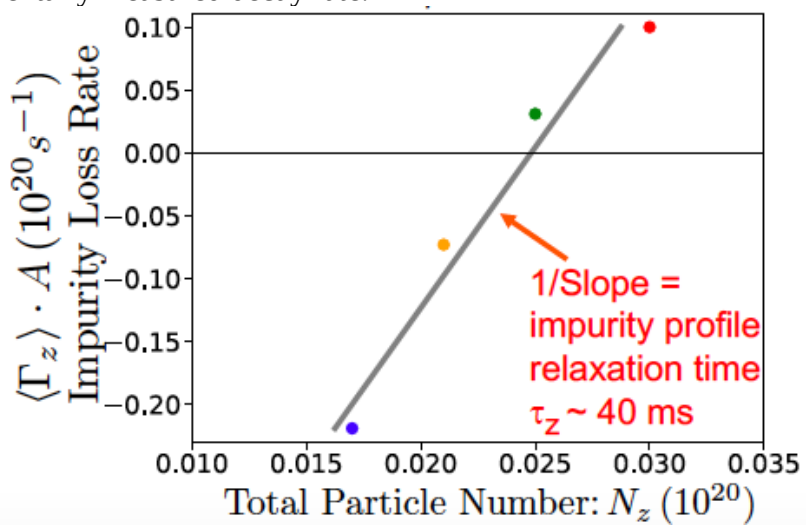

Figure 1.15: Plot of impurity particle loss rate versus total impurity particle number.

Impurity particle loss from global nonlinear simulations with these profiles are used to compute the impurity confinement time from ITG/impurity modes, as follows:

Because the impurity profile is flat in the core, the total number of impurities in the plasma, the inventory, N_Z is about plasma volume V times the impurity density at the top of the pedestal $n_{z,\,ped.}$

The rate of change of impurity inventory is determined by the impurity flux from the pedestal:

$$\frac{d\,\Delta N_z}{d\,t} = < \Gamma_z > \cdot A$$

where $<\Gamma_Z>$ is the surface averaged impurity flux. If the RHS is a linear function of N_z, then this equation describes an exponential decay to a steady state constant value. The steady state value is when the RHS =0, as indicated above. The decay rate can be found by plotting the RHS against N_Z, and examining the slope of the line. We can estimate (from

the inverse slope) the impurity confinement time: τ_Z ~ 40 ms; this value is quite close to the experimental measured value.

SYNTHETIC DIAGNOSTICS AND GEODESIC ACOUSTIC MODES

Geodesic-acoustic modes (GAM) and WCM are observed in I-mode on C-Mod using Gas-Puff-Imaging (GPI) based diagnostics[17], which mainly measures density fluctuations. The pattern of I-modes is similar: there is a spectral peak corresponding to a WCM, and an even stronger peak near $k_\theta \sim 0$ with frequency ~ $(2T_e/m_i)^{1/2}/R$, which are Geodesic Acoustic Modes (GAMs). GAMs are measured to exist approximately at the same location as the Er-well and WCM and interact with WCM[17].

We construct a synthetic diagnostic for GPI to see if our GENE simulations give similar results. There was no GPI measurement for our particular shot, so we can only expect qualitative agreement with GPI results from other I-mode shots.

Fig 9(a) in Ref. 12 shows the emission fluctuations measured by GPI at the horizontal midplane during an I-mode phase of C-Mod discharge 1100204022 (1.3 MA, 5.8 T, upper single null). A weakly coherent mode is visible, centered at about f ~ 220 kHz, $k_\theta \sim 1.25$ cm^{-1} (electron diamagnetic direction). There's also even higher intensity at $k_\theta \sim 0$ and frequency ~ 20 - 50 kHz, which are GAMs.

To construct a synthetic diagnostic, we first take note of the character of GPI. It takes pictures on a 2D array and the third dimension is integrated over the line of sight. Due to misalignment of its sightline with the local magnetic field line (θ_{mis} ~ 6 degree) as well as variation of magnetic field line pitch angle within the gas cloud, there's a finite spatial resolution of the GPI diagnostics[18] and higher wavenumber fluctuations along the line of sight are averaged out.

We implement our synthetic diagnostic for GPI to be convenient for GENE coordinates. The fluctuations we get from GENE simulations are expressed as

$$f \sim f(\theta, r) e^{i n (\zeta - q \theta)}$$

where θ and ζ are the magnetic coordinates for poloidal and toroidal angle and r is the radial coordinate. The coordinates and representation used in GENE is chosen so that the scale of variation of θ is on the order of the parallel correlation length. Rapid variations on the scale of $k_\perp$are due to the eikonal. The GPI image is in the (r, θ) plane averaging over the line of sight. This requires us to find an appropriate way to average over ζ. To simplify the problem, we Taylor expand the magnetic angle coordinates in the small gas cloud volume, which is a good approximation since the gas cloud dimensions is small compared to the magnetic equilibrium scales. We consider the origins of coordinates for all spatial distances to be at the center of the gas cloud. We expand $(\zeta - q\ \theta)$, obtaining $(\zeta - \frac{B_{tor}}{B_{pol}} \cdot \frac{y}{R})$, where y is the distance in the poloidal direction tangential to a flux surface. We then put this in terms of the toroidal distance (l), which is nearly the same as the sightline distance: $(l - \frac{B_{tor}}{B_{pol}} \cdot\ y)/R$. For convenience, we define the pitch angle of magnetic field line to be $\tan(\theta_B) = \frac{B_{tor}}{B_{pol}}$. The GPI averages over the line of sight, which we approximate to be given by the line $y = \tan(\theta_{sight}) \cdot l$. For every toroidal mode number n, we integrate along the sightline the assumed gas cloud emissivity profile:

$$I(l) \sim \frac{1}{r^2 + l^2}$$

where r is the perpendicular distance from gas nozzle to the observation point], and include the eikonal phase variation:

$$\int dl\ I(l)\ e^{i\,n\,\zeta}$$

Then the final synthesized density perturbation, as it would appear in the 2D GPI image, is

$$n(r,\theta) = \sum I_n\ n_n(r,\theta)\ e^{-i\,n\,q\theta}$$

where $I_n = e^{-n\frac{r|\theta_{sight} - \theta_B|}{R\quad\theta_B}}$, where $\theta_{sight} - \theta_B$ is the mis-alignment angle between light of sight and true magnetic field direction. (We have also approximated tan θ ~ θ, since all the angles are small.) Notice if there's no misalignment, $\theta_{sight} - \theta_B = 0$, then there's no reduction of resolution via the reduction of higher wavenumbers, since all $I_n = 1$.

This result is approximately what the GPI would observe by averaging over the sightline. Note that an additional level of signal processing, Velocimetry, is usually implanted for the GPI image of density fluctuations, and we have not implemented this.

The density fluctuation spectra in the nonlinear saturation state under different simulation conditions are not the same. For one simulation shown in Fig 1.16(a), we were able to reproduce qualitatively similar spectrum to the experimentally observed ones, with both WCM and GAM, at about the frequencies expected. The peak of the frequency is around 200-250 kHz which is slightly lower than the WCM (~ 300-400 kHz), as measured for this shot. The GAM frequency is ~ 20 - 50 kHz, as expected. For other simulations (an example shown in Fig 1.16(b)), we see a broad band of unstable modes each with comparable density fluctuation level. Same procedure of GPI filtering applied to those runs doesn't give us clear peak to match the observed WCM. Mismatch between the density fluctuations frequency spectrum and that of the observed WCM could arise from box parameters in our simulations, and experimental error in profiles. We leave more systematic sensitivity test to future work.

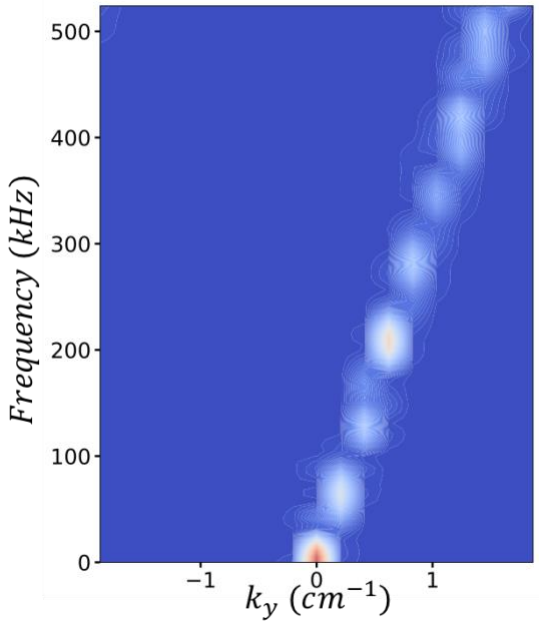

Figure 1.16(a): An example of results of GPI synthetic diagnostic that matches experiment.

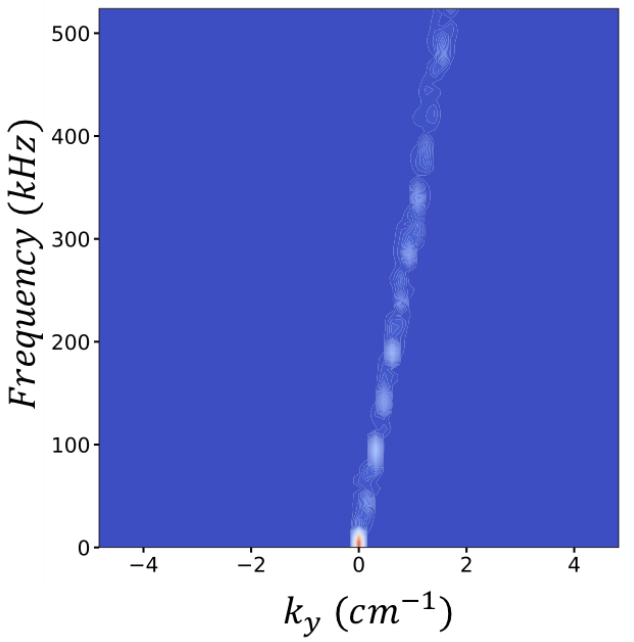

Figure 1.16(b): An example of results of GPI synthetic diagnostic that doesn't match experiment.

CHAPTER II: INVESTIGATIONS OF TWO DIII-D PEDESTALS IN ELMY H-MODES

DIIID H-modes Introduction

In this chapter, in addition to simulations, we emphasize a new concept called the "transport fingerprints", and show how it can be used to help identify the instabilities responsible in H-mode pedestals. We apply this concept to two ELMy H-modes on DIII-D, where the experimental pedestals have been diagnosed especially well.

The transport fingerprints of a particular instability is the ratio of the diffusivities it causes in different transport channels. For example, we can *define* a diffusivity as the ratio between the flux and gradient for quantities such as T_e, T_i, n_e, and the impurity density n_z. With this definition, it can be shown that many modes have a particular ratio of the diffusivities among the various quantities.

Basic theoretical considerations can be used to indicate the qualitative nature of the fingerprint. Here, we use gyrokinetic simulations to compute the ratios, and we find that they conform to the expected values. We apply these ideas, in detail, to two DIII-D pedestals, where good experimental diagnosis of pedestal behavior have been published: the identical pair of shots 153674 and 153675, which we refer to as shot 153674/5[19], and shot 98889[20]. The gyrokinetic analysis we give here allows us to determine, with good confidence, which modes are responsible for energy transport in these pedestals.

Certain instabilities that have been frequently mentioned in the literature as possible causes of energy transport in pedestals: ideal MHD-like modes (including Kinetic Ballooning Modes (KBM)), Electron Temperature Gradient (ETG) modes, Micro-Tearing Modes (MTM) and Ion Temperature Gradient/Trapped Electron Modes (ITG/TEM). Each of these modes has very different

1. stability and transport trends
2. mode frequencies in the plasma frame.
3. relative effects on various transport channels.

We use all of these properties to identify pedestal instabilities, based on the transport that is observed and the frequency of fluctuations that is measured. The observed transport can be inferred either from the inter-ELM evolution of the plasma profiles or from multi-channel transport analysis. DIII-D shot 153674/5 is an example of the former and shot 98889 is an example of the latter.

Analysis of DIII-D shots 153674/5 and 98889

We consider two DIII-D shots here, each with different types of observations:

1) Shot 153674/153675. Detailed observations of inter-ELM profile evolution were published for these shots[19]. Also, the time behavior of some profiles was highly correlated to fluctuation intensity of Quasi-Coherent Fluctuations (QCFs). The very different time behavior of profiles for temperatures and densities is strongly indicative of differences in transport in these channels.

2) Shot 98889. In this shot, a detailed transport analysis of the pedestal was done for T_e, T_i, and n_e [20]. This is the most straightforward type of analysis for application of transport fingerprints. However, such transport analyses are difficult and time consuming to perform for pedestals, so they are not usually available. In addition, for this shot, magnetic spectrograms are available that show QCFs as well.

To facilitate the identification of the mode or modes responsible for transport, we group instabilities into the following categories. These will be identified in pedestal profiles using GENE in the following section. We summarize the properties of each mode, as found by GENE.

MHD-like modes: This includes Kinetic Ballooning modes (KBM), peeling-ballooning modes, etc. These modes cause comparable diffusivity in all transport

channels. These modes are electromagnetic so that they can be detected on magnetic diagnostics. They have a relatively low frequency in the plasma frame, compared to the other main magnetic mode, Micro-Tearing Modes (MTM).

Micro Tearing Modes (MTM): These magnetic modes cause transport in the electron thermal channel, and relatively low transport in other channels. Their frequency in the plasma frame is of order ω_e^*, computed by including both density and temperature gradients.

Electron Temperature Gradient (ETG) modes: These modes have spatial scales less than an ion gyroradius. They cause transport in the electron thermal channel, and relatively low transport in other channels. Their spatial scales are too small for them to be detectable on most diagnostics.

The modes that are not suppressed by velocity shear in these pedestals are the MHD-like modes, the MTM and ETG.

Electro-static modes with $k_y\rho_s < 1$:

TEM/ETG modes: There are electron modes with $k_y\rho_s < 1$ that have frequencies of order or less than the electron bounce frequency ω_b. These Trapped Electron Modes (TEM), for the pedestals examined here, are found by GENE to have high radial wavenumber k_x so that $k_x\rho_s > 1$. These modes are a variant of the ETG mode, and have the same properties.

ITG/TEM modes: These modes are driven mainly by ion temperature gradient, and produce ion thermal conduction. They can also cause significant transport in other channels. For example, the ratio of the ion

thermal heat diffusivity χ_i to the electron value χ_e, χ_i / χ_e, is usually greater than 1 but can be of order 1 as well.

TAE/MTM modes: In a pedestal, because of steep gradients, the diamagnetic frequency ω_e^* can also be the same as the frequency of Alfven eigenmodes. Thus, we find that hybrid TAE/ MTM modes appear. Like MTM, these modes produce predominantly electron thermal transport. However, the transport has a substantial electrostatic component as well as an electromagnetic component. We can consider these to be a variant of MTM. Their growth rates are often less than MTM, and they might be suppressed by velocity shear.

DIII-D SHOT 153674/5 — EXPERIMENTAL OBSERVATIONS AND THEIR IMPLICATIONS

This case has an extensive diagnosis of inter-ELM behavior. Magnetic diagnostics and Beam Emission Spectroscopy (BES) find a Quasi-Coherent Fluctuation (QCF), which is strongly correlated with T_e evolution (Fig 2.1). In some ELM periods, there is a second band of QCF in the spectrogram as well.

We use two independent methods to identify this QCF: a) it's frequency in the plasma frame b) the transport it produces in multiple channels. These properties imply that the fluctuation is an MTM, not a KBM. Extensive simulations using GENE are used to verify these properties. In addition, we verify that c) simulations find that such instabilities can, and likely do, reach an amplitude where they produce substantial transport, carrying most of the pedestal heat losses. Hence, they saturate the pedestal evolution, as is indicated by the experimental observations.

a) Mode frequency in the plasma frame

The dominant QCF has f ~140kHz, in the electron direction (another QCF with f ~100kHz is sometimes present). It is found on magnetic diagnostics and BES. The BES is

used to identify the poloidal wavenumber k_y to be ~ 0.18 - 0.2 cm^{-1}. To identify the mode by frequency, it is crucial to establish the frequency in the plasma frame. In Fig 2.1, we plot the Doppler shift from the measured E_r and k_y and ω_e^*. Even for the *maximum* Doppler shift $\omega_{ExB}(r)$, the shift is much less than the lab f - *hence, f must be in the electron direction in the plasma frame, wherever the mode is "located".* The measured f is consistent with ω_e^* for the experimentally inferred position of the mode, but with a large uncertainty.

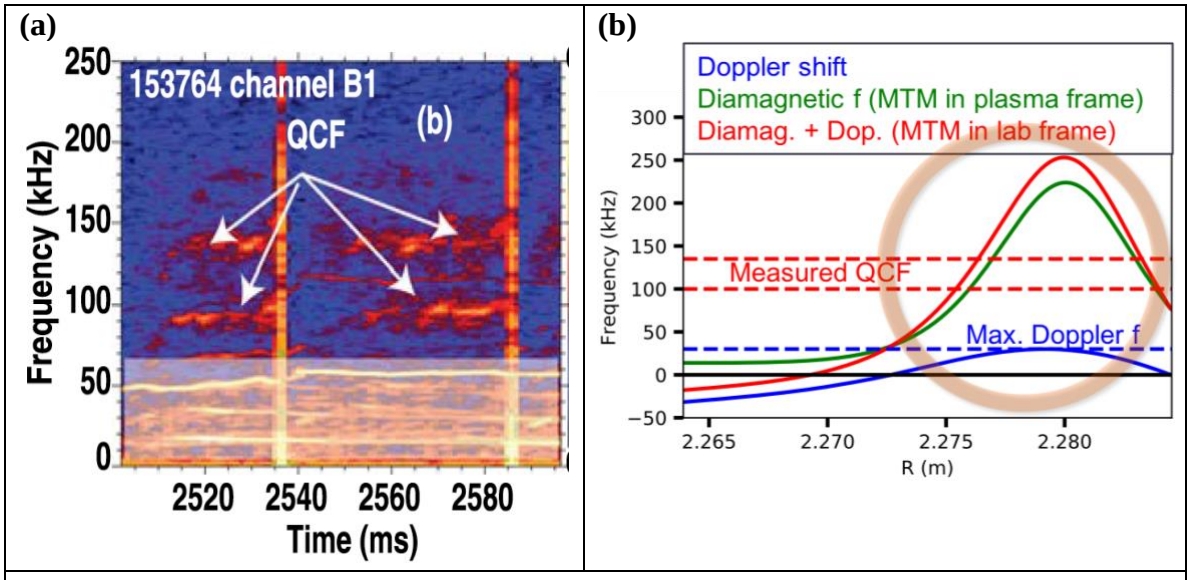

Figure 2.1 DIII-D shot 153674 a) Magnetic spectrogram of the experimentally observed fluctuations, showing measured QCF b) From experimental profiles, frequencies f for: Doppler shift (ω_{ExB}), ω_e^*, and the QCF. The circle shows the experimentally inferred maximum amplitude position of the fluctuation.

We now summarize the results regarding frequency that are discussed in detail in the section on gyrokinetic analysis. We start with local simulations with GENE. These find MTM with k_y roughly in the range of the experimental value, and frequency in the plasma frame ~ ω_e^*. They also find KBM near the top of the pedestal. Adding the Doppler shift at the location where the mode is unstable, the frequency of the KBM in the lab frame is ~ 30-40 kHz for the observed k_y value, which is about 4-5 times lower than the measured

QCF frequency. The MTM found, at the observed k_y value, have a frequency which is too high by about a factor of about 2.

Linear global simulations were also performed with GENE. For the given experimental profiles, there are MTM instabilities, but these have a k_y that is about 50% higher than the measured value. KBM instabilities were not found in any of the global simulations for shot 153674/5.

We have considered three cases where pedestal profiles of n_e and T_e are varied slightly, within the likely error bars, and where new, self-consistent MHD equilibrium were computed. With these, MTM instabilities can be found in global simulations where there is one clearly dominant instability with k_y within ~ 10% of the measured value for the QCM.

A qualitative feature of the instability spectrum found with GENE matches the observations. Rather surprisingly, the toroidal mode numbers of instabilities are isolated: only a few n are unstable, and these are usually separated by several mode numbers which are stable. The frequencies of these instabilities are therefore also distinctly isolated. This type of instability spectrum can lead to quasi-coherent modes with isolated frequency bands- which is what is observed, as seen in the Fig 2.1.

In addition to a dominant instability, for many profiles, there is a second weaker MTM with lower n and frequency. This roughly matches the observed magnetic spectrogram, which often has two frequency bands: one at about 140 kHz and another at about 100 kHz.

The spectrum which might have been obtained could have consisted of a band of instabilities. This would have led to a broad frequency band of fluctuations, unlike the isolated bands that are observed.

Hence, the qualitative nature of the spectrum, in addition to being surprising, also matches the experimental observations.

The global MTM usually have maximum amplitude in the region of steeper profile gradients, where ω_e^* is larger, consequently, their linear mode frequency in the lab frame (with the measured $\omega_{ExB}(r)$ profile included in the simulation) is larger than the QCF frequency by a factor ~ 1.8. Nonlinear simulations find a strong downshift in the frequency to be ~ 200 KHz, which is much closer to the values observed, but still too high by a factor of about 40%.

In the original paper on these shots[19], it was suggested that the QCF was a KBM, based on the consistency of pedestal pressure with EPED, and local gyrokinetic simulations using the gyrokinetic code gs2. As noted above, the frequency of the local linear KBM in the lab frame is too low by a factor of 3-4. Also, KBM instabilities have not been found in global simulations. As discussed in the gyrokinetic section, the local modes are found to be insufficiently robust to "fit" within the spatially limited domain of a pedestal. (However, we must add the caveat that the version of GENE that was used did not include some MHD effects that are not present in lowest order gyrokinetics, and which might lead to MHD instabilities.)

Hence, simulations with GENE find that MTM modes are the most robust instabilities in this pedestal for k_y in the range seen. Using global simulations, by making slight variations in the profiles (likely within the error bars), MTM can be found which are unstable only for the observed k_y range seen (within ~ 10%), and hence should lead to QCF-like modes. The frequencies of the linear modes are too high by ~ 2x. However, nonlinear simulations find saturated MTM instabilities with a frequency within ~ 40% of the observed value.

Thus, simulation results for the frequency and spectrum of the instabilities match with MTM fairly well, and do not match with KBM.

b) Inter-ELM evolution of pedestal profiles

We now turn to consider the transport channels affected by the instabilities, and comparisons with observations.

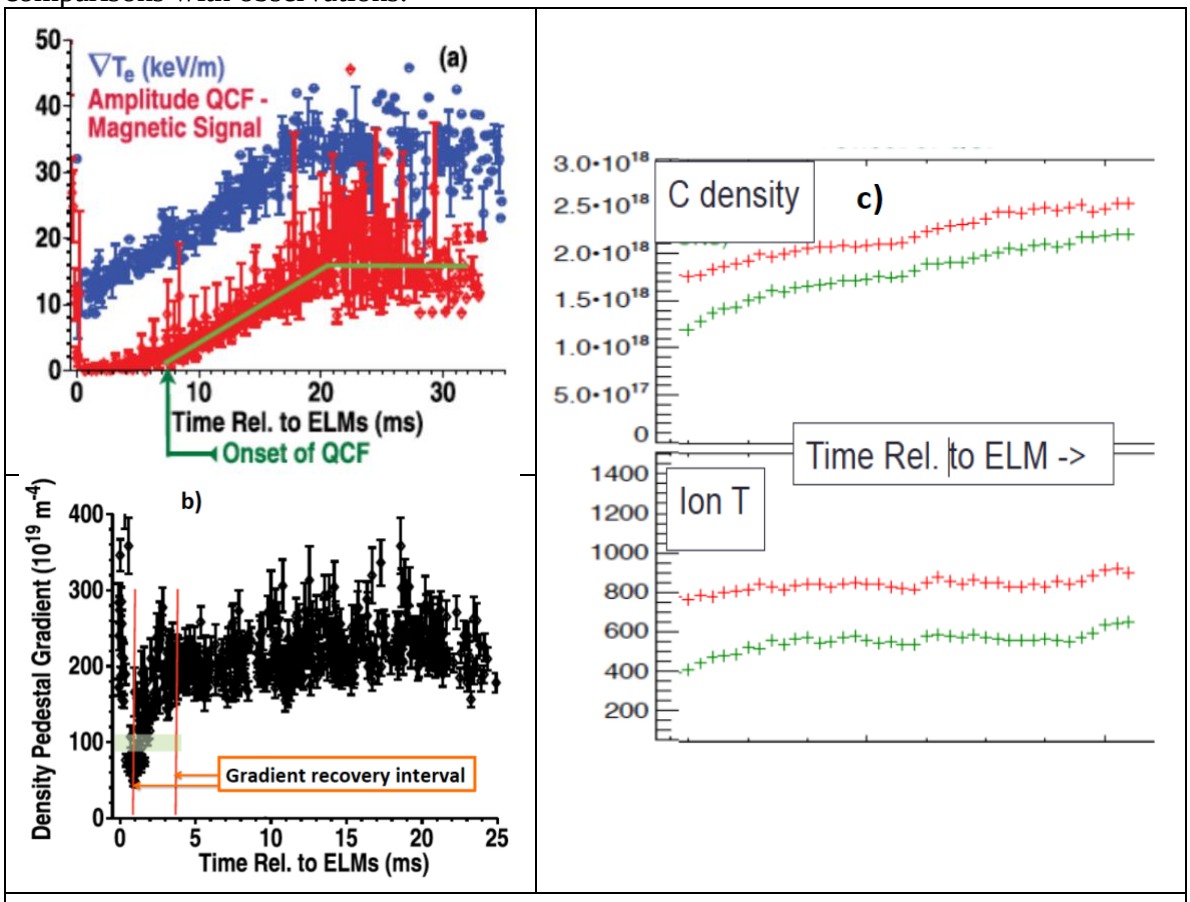

Figure 2.2: DIII-D shot 153674 Inter-ELM evolution of T_e gradient and QCF amplitude showing strong correlation, expected for an MTM b) Evolution of the electron density gradient, which saturates much more quickly, and is unaffected by the growing QCF c) Evolution of T_i and n_{Carbon} after an ELM, for a typical ELM cycle, showing no discernable effect of growing QCFs- consistent with MTMs, but not KBMs. Note the difference between values on two cords is proportional to the average gradient between them. Hence, the gradient of T_i and n_C between the cords is apparently unaffected by the growing QCF.

As emphasized in the published analysis of this, the growth of the magnetic signals is strongly correlated with the evolution of the T_e gradient (see Fig 2.2 (a)). This strongly suggests that the QCF is driven by T_e gradient, and/or, causes substantial transport in that channel. It is also seen that as the QCF reaches sufficient amplitude, it saturates at about

the same time as the T_e gradient saturates, further strengthening the likelihood of a physical link between them.

However, the QCF appears to have no effect on the evolution of the density gradient (see Fig 2.2 (b)). Electron density gradient saturates well before the onset of the QCF, and the growing QCF has no apparent effect on it. An MHD-like mode would be expected to be driven by, and to try to relax, density gradients. On the other hand, an MTM would be driven by, and only affect, T_e gradients. Hence, the lack of correlation between the density gradient evolutions and the QCF is not expected behavior for an MHD-like mode, but is expected for an MTM.

The GENE results also show that the KBM instability, which is often considered as a source of transport in pedestals, is found in local linear simulations has comparable diffusivity in all channels: T_e, n_e, T_i, and n_C.

We are thus led to examine the inter-ELM evolution of the T_i, and n_C channels. Consider pedestal measurements of T_i and the impurity density of Carbon n_C. These are shown in Fig 2.2(c), for a representative inter-ELM period. We show data from two separate chords in the pedestal. Of course, the spatial separation between the cords do not change, so the difference in the signal between the cords is proportional to the average plasma gradient of the quantity between the cords. As can be seen, this difference is very nearly constant over the inter-ELM period, for both T_i and n_C. An MHD-like mode would be expected to cause comparable diffusivities in these channels, as compared to the T_e channel. Hence, the lack of an effect of the growing signal on these channels in not the expected behavior for an MHD-like mode. It is, however, totally consistent with the behavior expected for an MTM.

One might raise an objection that the observed signal may simply not be causing sufficient transport to affect various channels. We think this is an implausible objection, for the following reason. The magnetic signal was observed with great regularity in essentially every inter-ELM phase of this discharge. Suppose this signal was an MHD-like

mode. Such modes, including KBM, are very strong instabilities. Once the threshold of an instability is crossed by even a very small amount, it is expected to create every large transport to enforce marginal stability. It is not plausible to suppose that the inter-ELM profiles repetitively crossed the stability boundary by a minuscule amount every ELM period, so that it rarely caused significant transport, but was nonetheless always present. The only plausible hypothesis is that, the stability boundary was regularly crossed, giving substantial transport that ultimately enforced marginal stability. Hence, if this signal were a KBM, it is not plausible that it was not causing substantial transport. Hence, there should have been some effect on the profiles of n_e, T_i, and n_C. The lack of evidence for this is therefore inconsistent with this signal being a KBM.

In summary, the evolution of T_e, n_e, T_i, and n_C in this pedestal is not consistent with the signal being a KBM, but is very consistent with it being an MTM that likely caused significant transport.

Thus, we conclude that the observed fluctuation is an MTM, based on both its frequency and on the profile evolution of T_e, T_i, n_e and n_C in the inter-ELM period.

c) Heat loss from nonlinear simulations

The nonlinear analysis of this shot find that power balance can be matched by a combination of MTM and ETG instabilities. By making slight adjustments of the profiles within the error bars, the relative importance of the MTM and ETG changes. So we cannot specify the relative importance of these.

Importantly, note that ETG have the same transport fingerprint as the MTM- the electron thermal channel is, by far, the most strongly affected. Hence, any transport caused by ETG as the T_e gradient increases is also consistent with the observed inter-ELM profile evolution of n_e, T_i, and n_C.

DIII-D SHOT 98889 – EXPERIMENTAL OBSERVATIONS AND THEIR IMPLICATIONS

We now turn to shot DIII-D 98889, where an extremely valuable transport analysis is already available[20]. A summary of the conclusion is as follows.

a) The inferred χ_e is about twice the magnitude of χ_i

b) The latter (χ_i) is roughly consistent with neoclassical or paleoclassical expectations.

c) The inferred electron diffusivity *D_e is an order of magnitude lower than χ_e*

From just these considerations, we can conclude that MHD-like modes cannot be predominantly responsible for energy transport. This conclusion can be reached by considering inferred diffusivities in either the n_e or the T_i channel. Consider n_e first. Most transport comes through the anomalous electron channel. If this were due to an MHD-like mode, there would be an anomalous particle diffusivity $D_e \sim \chi_e$. However, the inferred D_e is an order of magnitude less, so this is not possible. In fact, if all the anomalous D_e was due to an MHD-like mode, that could only contribute ~ 1/10 of the anomalous χ_e.

Now consider the ion thermal channel. If most of the anomalous χ_e was due to an MHD-like mode, there would be a comparable anomalous χ_i. However, the inferred χ_i is about half the χ_e. Furthermore, apparently, most of the χ_i can be accounted for by ion neoclassical diffusivity χ_{neo}. Hence, the anomaly in the ion channel, $\chi_i - \chi_{neo}$, is even substantially smaller compared to χ_e than ½. Hence, considerations of ion thermal transport also imply that MHD-like modes cannot be responsible for most of the energy transport.

The observed transport is, however, consistent with some combination of MTM and ETG being responsible for anomalous energy transport.

We expect that ITG/TEM modes are probably strongly suppressed in this pedestal, since their growth rates are much smaller than the ExB shear rate (the latter can be obtained from the measured E_r). However, even if they were, somehow, present, they cannot be a dominant contributor to anomalous energy transport. Recall that these modes have a turbulent χ_i that is on order of, or larger than, turbulent χ_e. The same argument we used above for MHD-like modes, by considering the ion thermal channel, applies for ITG/TEM:

since the anomaly in the ion χ, χ_i - χ_{neo}, is considerably smaller than χ_e, ITG/TEM transport cannot be responsible for the anomalous χ_e.

Hence, the only consistent candidates for anomalous energy transport are MTM and/or ETG.

Note that a magnetic spectrogram for this shot (see Fig 2.3(a)), shows QCFs that are correlated with the ELMs, and which grow in strength as the inter-ELM phase proceeds. An upper band has modes with f ~ 180 and 220 kHz in the electron direction, and a lower band has f ~ 40 and 60 kHz. The k_y could not be experimentally determined. However, we can make the following argument based on a bound for k_y. Magnetic perturbations exponentially decay in the vacuum, with an e-folding length scale of ~ 1/ k_y. The magnetic diagnostic was located ~ 20 cm away from the plasma edge, so one can estimate that the largest k_y that might be detected corresponds to $k_y \sim 0.5$ cm^{-1}. This maximum bound on k_y allows us to compute an upper bound on the Doppler shift from the measured E_r. This maximum is only about 40% of the frequency in the high f bands. Hence, the signal must be strongly in the electron diamagnetic direction, which is consistent with MTM, and probably inconsistent with KBM.

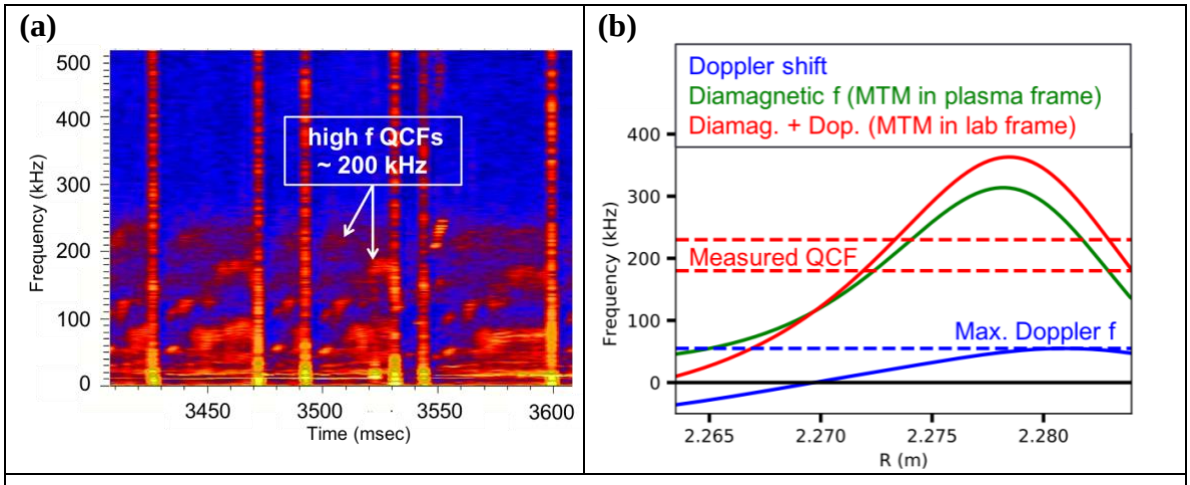

Figure 2.3: DIII-D shot 98889 a) Magnetic spectrogram showing measured QCF b) From experimental profiles, frequencies f for: Doppler shift (ω_{ExB}), ω_e*, and the QCF.

We now summarize the gyrokinetic simulations of this pedestal.

Local linear runs find primarily MTM in the mid pedestal region. These modes, in the plasma frame, have $\omega \sim \omega_e^*$, and cause almost exclusively electron thermal transport. KBM modes are not found.

Global linear runs find MTM with n = 16, 18, and 21; as was the case for the shot 153764/5, the unstable n numbers are separated by stable numbers in between. These modes have f ~ 280-330 kHz, which is about 50% above the observed frequency of QCFs on the magnetic spectrogram. However, nonlinear runs reduce this to within ~ 40% of the experimental observations. The energy transport for the n=16 is ~ 1.0 MW, together with ~ 0.6 MW from n = 18, the MTM transport power totals to 1.6 MW. Together with ETG transport, as noted below, this can match power balance for this shot.

In addition, ETG modes are found within the pedestal. However, the $\eta_e = d \log T_e / d \log n_e$ for these is rather low (< 2), so they are relatively weak. Nonlinear runs find that they only produce ~ 0.1 MW of transport power. However, if η_e is increased by 20%, which is likely within the error bars, this increases to ~ 0.3 MW.

Thus, the combination of MTM plus ETG can match power balance. The turbulent losses are virtually entirely though the electron thermal channel, which is consistent with the transport analysis.

Linear ITG/TEM modes are found near the pedestal top. The growth rate γ of the modes is less than the local ExB shearing rate γ_E. As discussed in the gyrokinetic results, we expect that such modes produce little transport. For these modes, $\chi_i / \chi_e \sim$ 3-4. Hence, these modes could not explain the observed anomalous transport in any case, which this is mainly in the electron thermal channel.

SUMMARY OF CONCLUSIONS OF THE EXPERIMENTAL COMPARISONS FOR SHOTS 153674/5 AND 98889

For both shots, the energy transport is mainly from MTM and ETG modes, not MHD-like modes. Also, high frequency QCF bands in the magnetic spectrograms of these shots are a good match to MTMs, but not to KBMs.

In both cases, the observed transport in channels other than T_e, is not consistent with MHD-like modes, or ITG-like modes, being the cause of most of the energy transport. If such modes were responsible for most energy losses, transport would have been substantial in the channels for n_e, T_i, and n_C (in the case of 153674/5), and this was not observed in the experiments.

Gyrokinetic simulations find that small adjustments in the profiles can lead to transport levels that match power balance for these shots. In both cases, the transport levels are sensitive to fairly small changes in the profiles.

EQUILIBRIUM CONSIDERATIONS FOR DIII-D SHOTS 153674/5 AND 98889

GENE was used to simulate pedestal modes in equilibrium reconstructions of DIII-D shots 153674 and 98889. Measured profiles of n_e, T_e, T_i and n_C (carbon density) were used, together with magnetic equilibria as EFIT files.

For shot 98889, the same EFIT reconstruction is used for GENE simulations as was used for the transport analysis, for consistency. The pedestal for 98889 is nearly twice as wide as for 153674/5, so the relative resolution of the EFIT file (128 x 128) was considerably better in the case of 98889.

The EFIT obtained for shot 153674 did not have many grid points in the pedestal region, leading to concern about the accuracy of the equilibria for gyrokinetic calculations. Hence, we reconstructed a higher resolution equilibrium for case 153674/5. There was also a bonus to implementing this procedure for 153674/5: it was also easier to perform sensitivity analysis of the results to small profile variations, while employing a self-

consistent MHD equilibrium. This capability was used to examine three slightly modified equilibria.

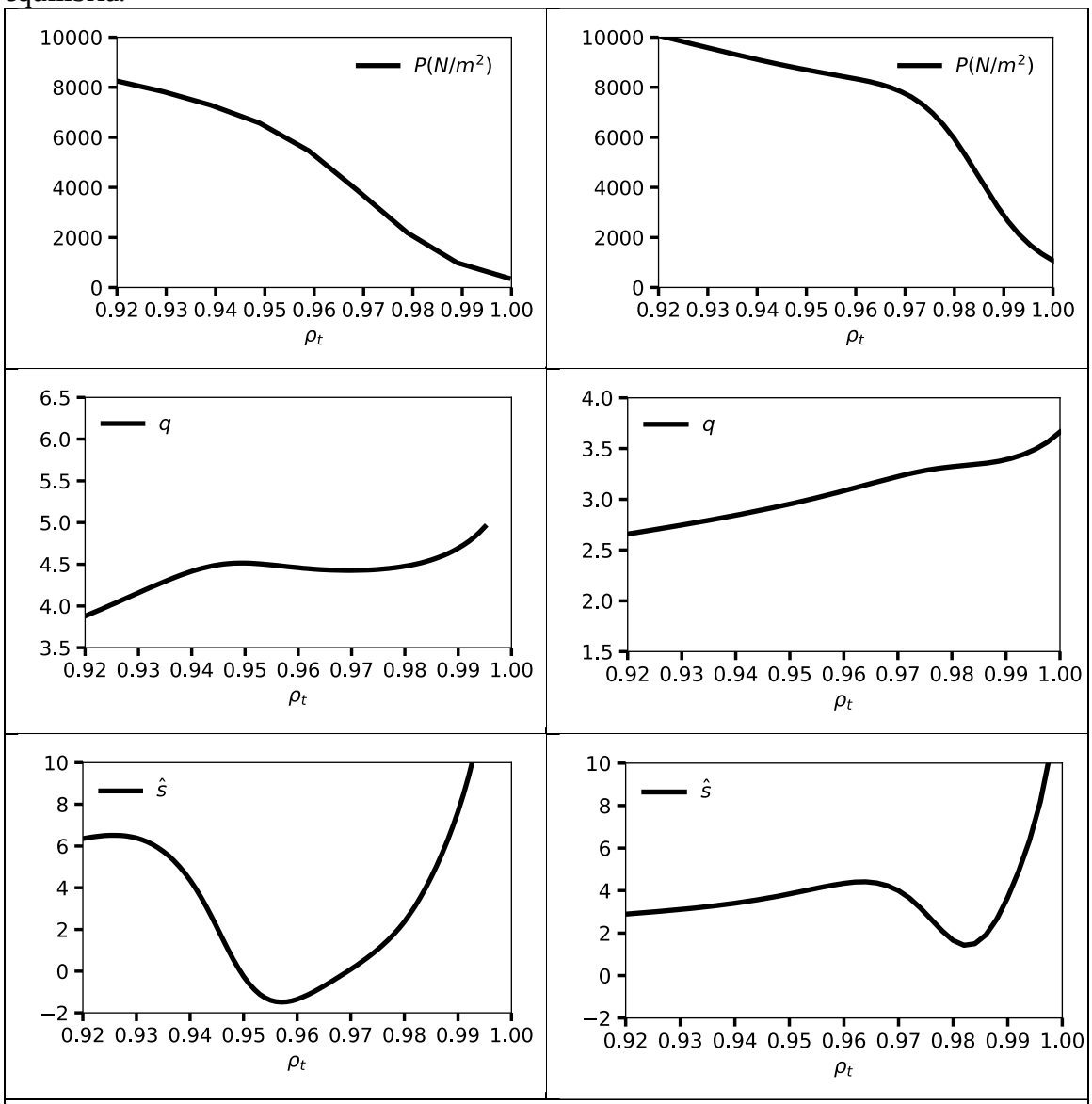

Figure 2.4: plots of pressure, q and shat for both equilibria (Left: 98889, Right: 153764)

The procedure for improving the accuracy was as follows: the boundary shape of the 99.5% flux surface from EFIT was used as the boundary for the VMEC code[21]. The equilibrium was recomputed with VMEC using much higher resolution: 500 radial grid points. The current profiles were computed by adding the bootstrap current to the Ohmic current computed using neoclassical theory. The value of the loop voltage was adjusted to

match the total current of the experimental case. Bootstrap current and Ohmic current were computed using the Sauter formula[22]. These formulas have often been used for pedestal studies, in particular, for recent DIII-D pedestal reconstructions. The collisionality of the pedestal 153674 is rather low, so this formula is expected to be acceptably accurate for this case[23].

The procedure just mentioned also enables an analysis of the sensitivity of shot 153674 to small variations of the equilibrium profiles within the likely error bars. The profiles of density and temperature could be changed slightly, and then these were used (with the self-consistent bootstrap current and Ohmic current) to create new equilibria. This is an important level of self-consistency, since many of the instabilities we consider are sensitive to the magnetic shear, and this is changed by altering the profiles that lead to the bootstrap current. This level of consistency is often neglected in pedestal sensitivity studies, so the present analysis is an improvement in this regard.

We will consider three profile modifications in detail, shown below. We also show the associated modifications of the magnetic shear. As can be seen, the mod1 and mod5 cases are quite small changes in the n and T profiles, and we certainly expect them to be within the error bars. Nonetheless, they lead to substantial changes in the magnetic shear. We also consider an additional case, mod3, which is likely at the limit of the error bars, or perhaps slightly beyond. These profiles lead to significant changes in the instabilities found, particularly in the case of MTM. We note that a quantitative analysis of the profile error bars for case 153674 is presently under consideration[34].

Gyrokinetic analysis of DIII-D discharges 153674/5 and 98889

We have performed multiple levels of analysis on the equilibria described above using the multiple capabilities of GENE. We consider local linear simulations (using the conventional ballooning transformation), global linear simulations where full profile variations are taken into accounts, and global nonlinear simulations.

For linear cases, it is conventional to report the growth rates for linear instabilities, and for nonlinear simulations, the transport heat loss. We go well beyond this in the results reported here. We also report other crucial quantities, which have not usually been considered in gyrokinetic analysis:

The transport fingerprints of the modes: This is the ratio of diffusivities in various channels. For linear modes, these are the quasi-linear (Q-L) ratios. (The Q-L ratio is independent of the mode amplitude).

The mode frequency in the lab frame: This includes the Doppler shift from the measured E_r. In the case of local simulations at a given radius, the Doppler shift using the measured E_r at that same radius is used. The resulting frequency in the lab frame is crucial for comparisons to fluctuation diagnostic measurements. Despite its importance, the locally Doppler shifted frequency in the lab frame is not usually reported for local linear gyrokinetic calculations. In the case of global simulations, the full E_r profile is used, so that the frequencies found correspond to the lab frame. Frequencies found on diagnostics, such as Mirnov coils, Beam Emission Spectroscopy, etc., can be compared with the frequencies just described.

Whether the mode can fit into a box of the pedestal width: This is an important consideration which applies only to local linear calculations, and is considered for the first time for pedestals (to our knowledge) in this work. Local linear calculations are the most commonly reported type for gyrokinetic simulations of pedestals. It is well known that such local calculations, which use the lowest order ballooning transformation, should have a next order calculation to decide if eigenmodes are actually present.[24, 25] The next order theory is virtually never applied in practice, because it is an extremely large increase in the complexity of the calculation.

Nonetheless, such considerations are particularly pertinent to a pedestal, where equilibrium quantities can vary rapidly in space.

Here, we present an approximate criterion, suitable for practical calculations, that is motivated by more complete next-order theories. The latter imply that the next order theory can be considered a Fourier transform convolution. Here, we find the width in k_x, Δk_x, over which the mode is unstable. The product of this with the pedestal width must satisfy $\Delta k_x\, w > 2$ (as in the Heisenberg uncertainty principle) for the mode to fit into a box of the width of a pedestal.

Such a criterion has never been considered before. As we will see, it rules out many of the instabilities that are found in local calculations. Indeed, the mode that survives this criterion most consistently, in the pedestals we analyze, is the MTM. The criterion should be considered a necessary, but not sufficient, criterion for the presence of an instability. Global linear calculations bear this out: local modes that fail to satisfy $\Delta k_x\, w > 2$ are not found in global calculations. Modes such as MTM that satisfy it are sometimes seen, and also, sometimes not. This may be due to the fact that the criterion is often not satisfied by a large margin.

Whether velocity shear is likely to suppress the mode: The edge transport barrier exists because ExB shear is able to suppress turbulence. Hence, to estimate whether a mode is likely to be able to avoid suppression, we compare the linear growth rate to the ExB shearing rate γ_E (obtained from the measure E_r). Many pedestal modes have a short radial scale Δx compared to their poloidal scale Δy. Shear suppression theories find that this should reduce the effect of shearing, so that the growth rate should be compared to $\gamma_E\, \Delta x / \Delta y$.[25-27] To estimate this for linear modes, we use

the numerically computed eigenfunction to compute average $<k_\perp^2>$, and we estimate $\Delta x/\Delta y \sim (k_y^2/<k_\perp^2>)^{1/2}$.

We will organize the gyrokinetic results below by the mode type.

To clarify the relationship between the radial coordinate and the pedestal profiles, we show the profiles vs the normalized toroidal flux (ρ_t) below.

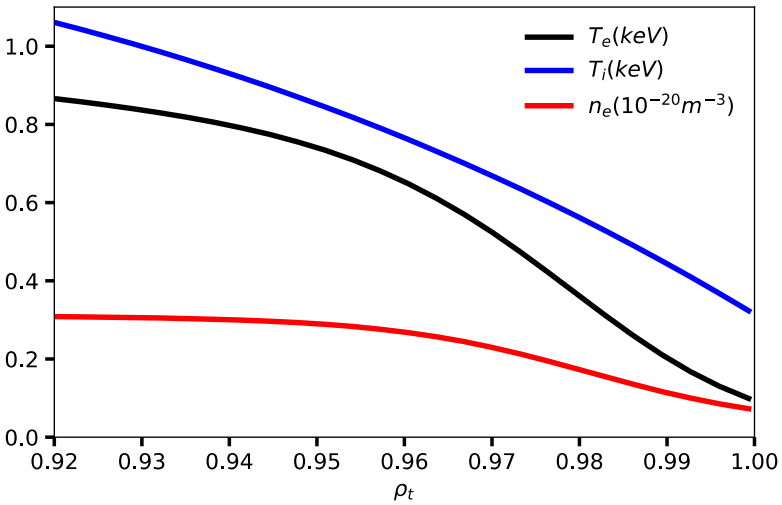

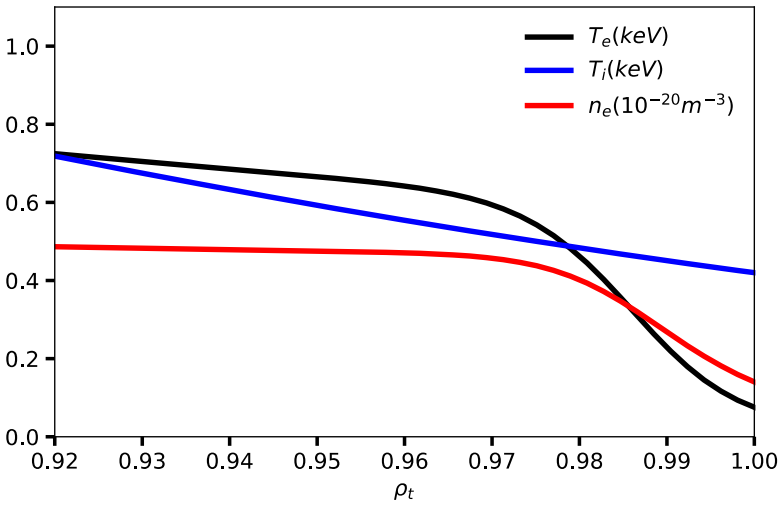

Figure 2.5: Profiles of T_e, T_i and n_e for the case 98889 (left) and 153674/5 (right)

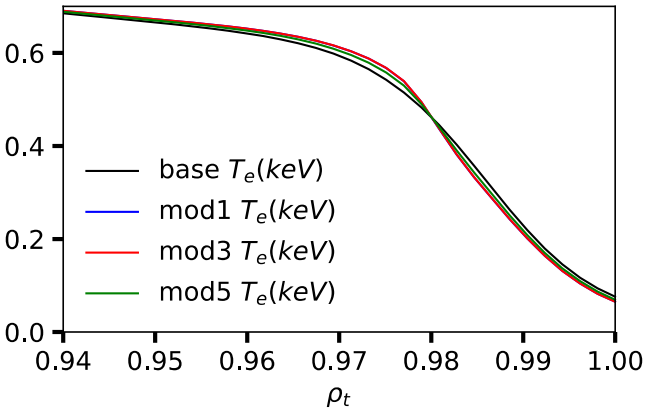

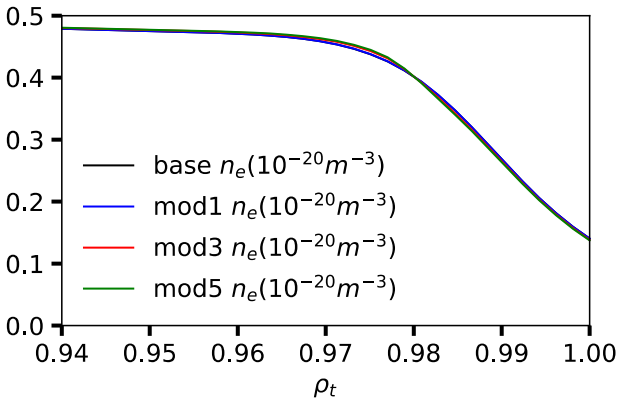

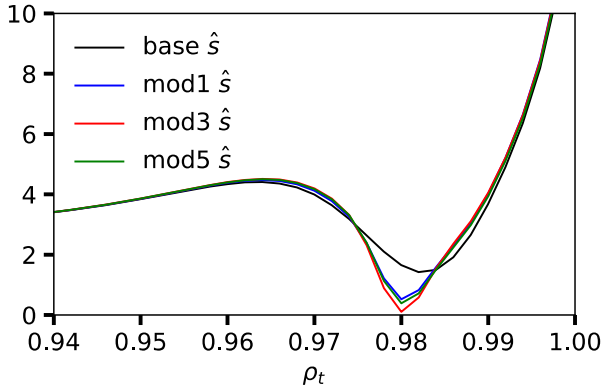

Figure 2.6: Modified profiles for case 153674/5. Despite the slight changes, magnetic shear is altered significantly

MHD-LIKE MODES

DIIID 153764/5 Local linear simulations

Growth rates increase rapidly with β

Such modes were found in shot 153674/5 near the top of the pedestal (for $k_X = 0$) Such modes were found in previous local linear gyrokinetic simulations of this pedestal using gs2[19]. Below, we show a scan of growth rate vs $k_y\rho_s$. We use a common procedure to vary the strength of MHD-like instabilities; we artificially increase β in the simulation [28, 29, 19]. As can be seen in Fig 2.7 (a), small increases in β result in large and rapid increases in the growth rate in the range $k_y\rho_s < 0.4$. This is strongly indicative that this is a KBM instability. (Note the definition of $k_y\rho_s$ used by GENE is not the value at outboard midplane, and different from the definition used in gs2 results reported for this shot.)

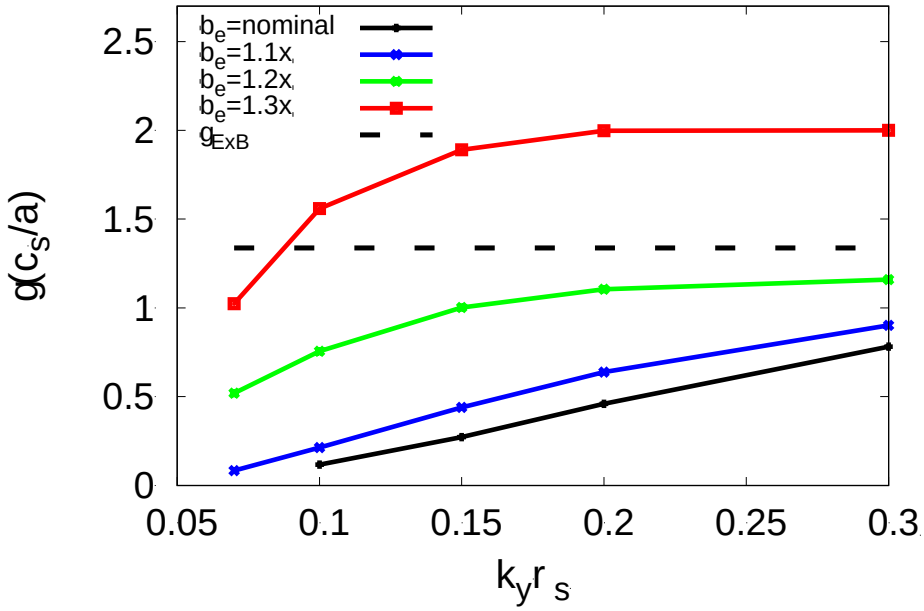

Figure 2.7 (a): Mode growth rates for $k_y\rho_s$ scan for DIIID 153764 base case at $\rho_t = 0.972$.

These results indicate that, for local linear calculations, the mode is fairly close to the marginal stability threshold near the top of the pedestal, in agreement with previous calculations for this shot[19].

Modest increases in instability (here implemented by increasing beta) can produce instability growth rates that exceed the ExB shearing rate (as is proposed in the EPED model[30]). Hence, these modes should be considered a candidate for producing pedestal transport and the experimentally observed fluctuations.

Hence, we proceed to analyze its characteristics in detail. As indicated in the section above, we will ultimately conclude that this mode is inconsistent with the observations, as regards its frequency and transport fingerprint.

Strong parallel electric field < $E_{||}$ > cancellation

To further verify the mode identification, we compute the eigenfunction averaged $E_{||}$ as in Ref.6. This quantity is small, indicating that there is strong cancelation between the electrostatic and electromagnetic contributions to $E_{||}$: a signature of an MHD-like mode. Furthermore, this cancellation gets stronger as the mode becomes more unstable, as expected of KBM: the ideal MHD limit is approached more closely as the mode becomes more unstable[31].

As the beta multiplier exceeds about 1.1 to 1.2, there is a distinct jump in the growth rate, and the $E_{||}$ becomes distinctly smaller. This behavior is expected for a KBM.

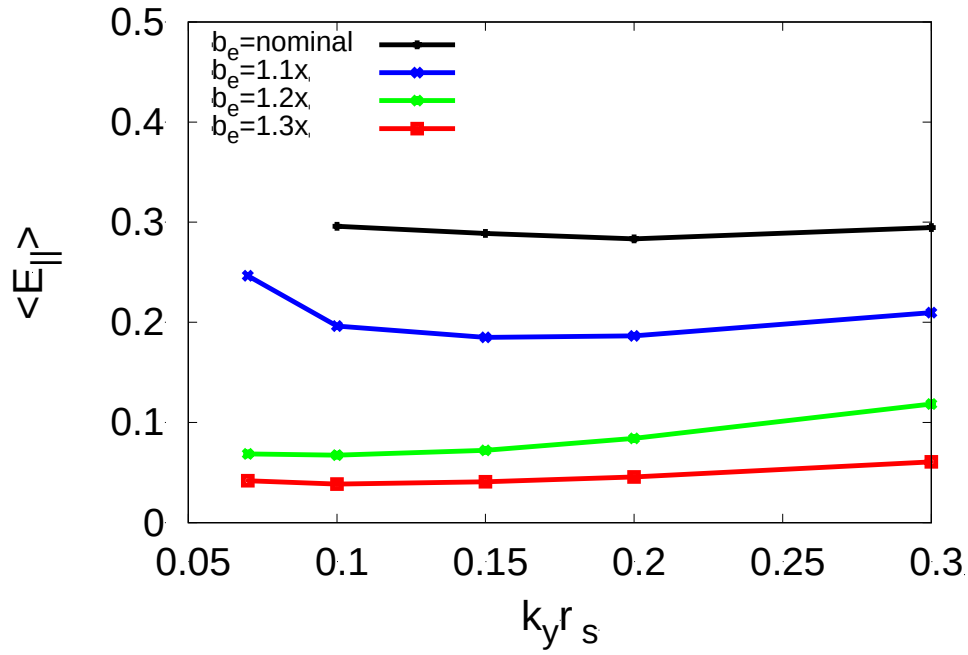

Figure 2.7 (b): $<E_{||}>$ for $k_y\rho_s$ scan for DIIID 153764 base case at $\rho_t = 0.972$.

Mainly electrostatic heat loss

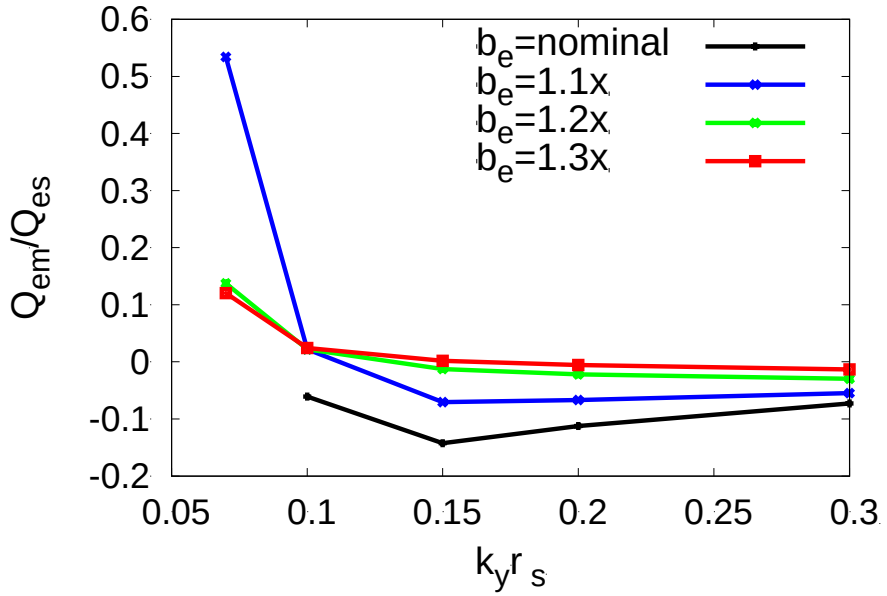

Figure 2.7 (c): Ratio of electromagnetic to electrostatic heat flux for $k_y\rho_s$ scan for DIIID 153764 base case at $\rho_t = 0.972$.

Also note that the electrostatic flux is much larger than the electromagnetic flux, even for electrons, which is another characteristic of an ideal MHD mode.

Transport Fingerprint: all diffusivities are comparable

The transport fingerprint of this mode agrees with the expectations of an MHD-like mode: all diffusivities are comparable as the mode goes into the MHD unstable regime. That is, when growth rates exceed the ExB shear, i.e., β is multiplied by ~ 1.1- 1.2 or more, or $k_y\rho_s$ becomes > 0.15, all diffusivities are comparable.

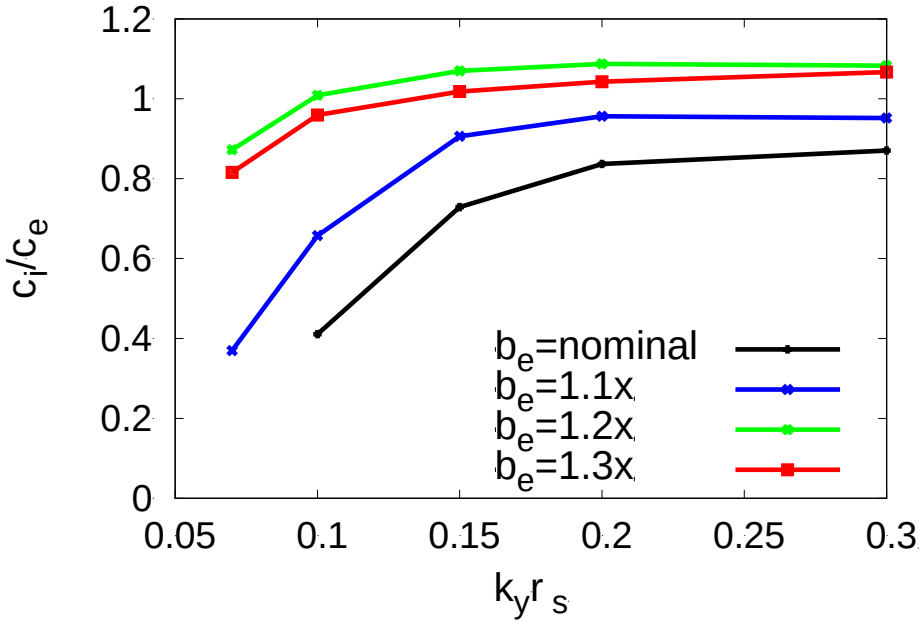

Figure 2.7 (c): Ratio of ion to electron thermal diffusivity for $k_y\rho_s$ scan for DIIID 153764 base case at $\rho_t = 0.972$.

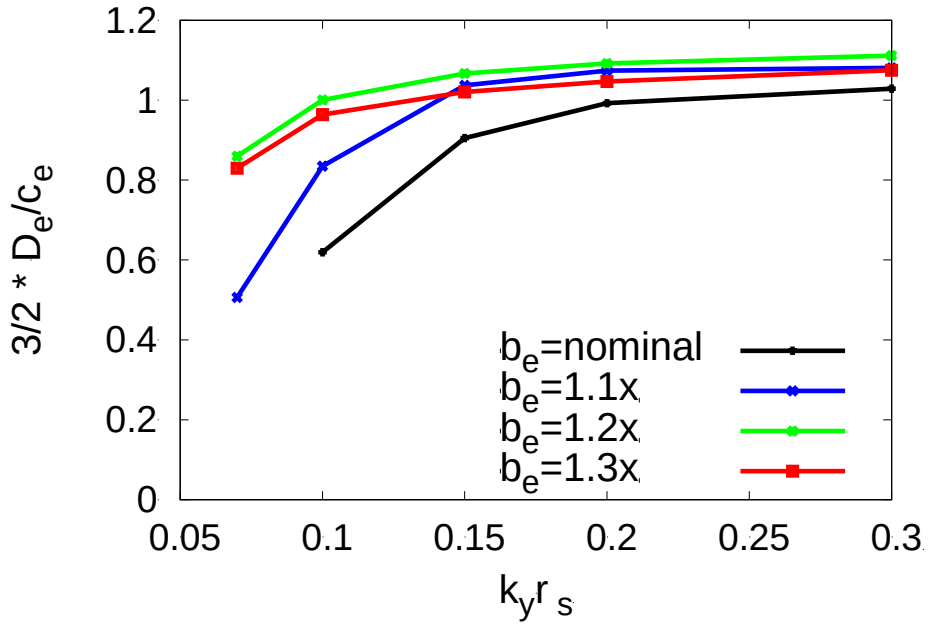

Figure 2.7 (d): Ratio of electron particle diffusivity to thermal diffusivity for $k_y\rho_s$ scan for DIIID 153764 base case at $\rho_t = 0.972$.

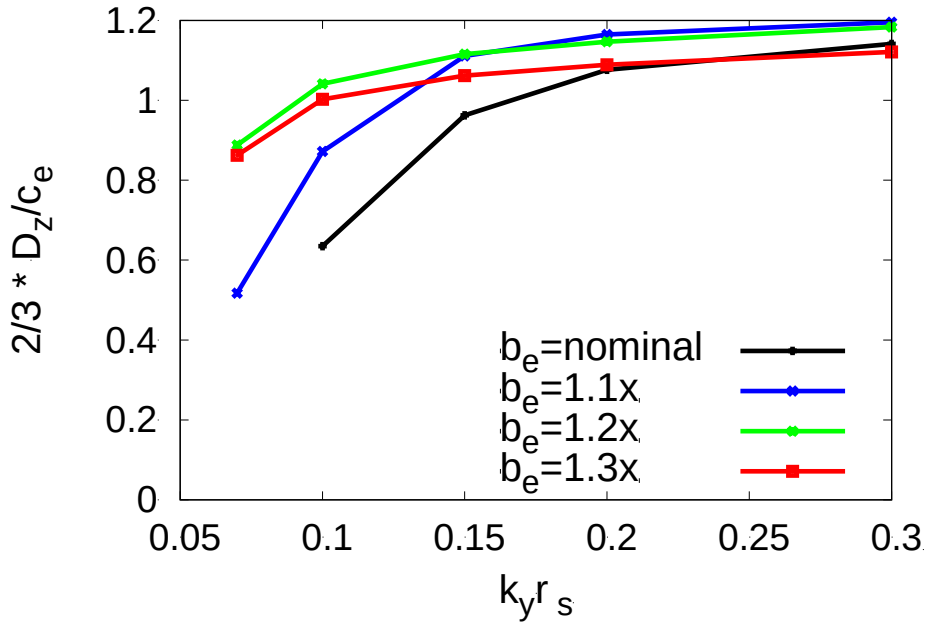

Figure 2.7 (e): Ratio of impurity particle diffusivity to electron thermal diffusivity for $k_y\rho_s$ scan for DIIID 153764 base case at $\rho_t = 0.972$.

The transport fingerprint of the KBM conforms to the expectations for an MHD-like mode. However, this is incompatible with the observed inter-ELM pedestal evolution, as indicated in the section above.

Frequency too low to match observed QCFs

Note that the mode frequency in this local calculation is not always in the ion diamagnetic direction. This same characteristic has been noted in other local gyrokinetic calculations of pedestals [28, 29,19]. However, the mode frequency is still much smaller than the characteristic frequency of an MTM: ω_e^* computed with both density and temperature gradients. Hence, the mode frequency of an MTM can still be readily distinguished from an MTM.

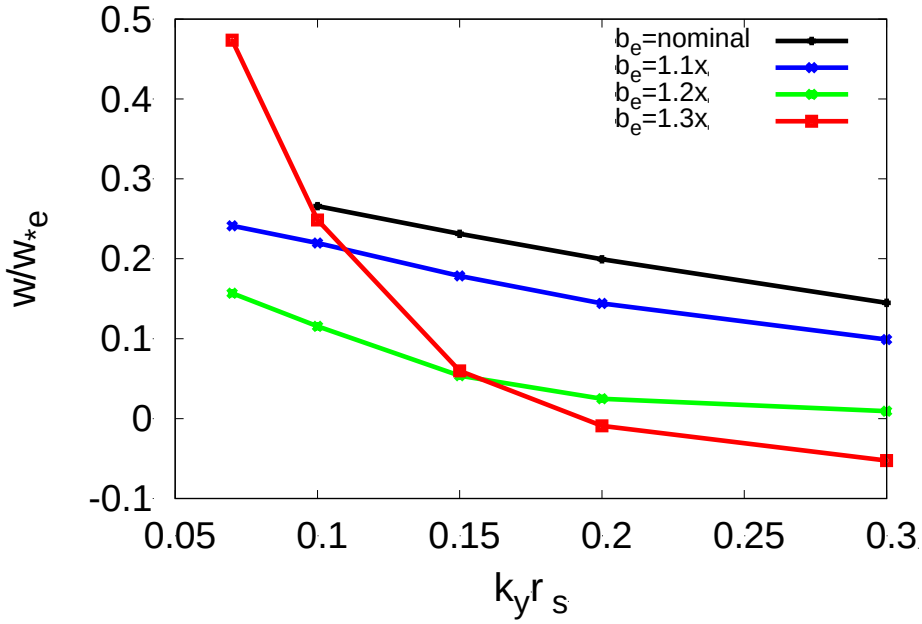

Figure 2.7 (f): Mode frequency (in plasma frame) normalized to ω_e^* for $k_y\rho_s$ scan for DIIID 153764 base case at $\rho_t = 0.972$.

To compare with experimental observations, we compute the frequency in the lab frame, adding the Doppler shift from the measured value of E_r at this location. This is

strongly incompatible with the observed frequency of ~ 140 kHz, even if we consider including k_y values within a factor of 0.7 to 1.5 of the measured value.

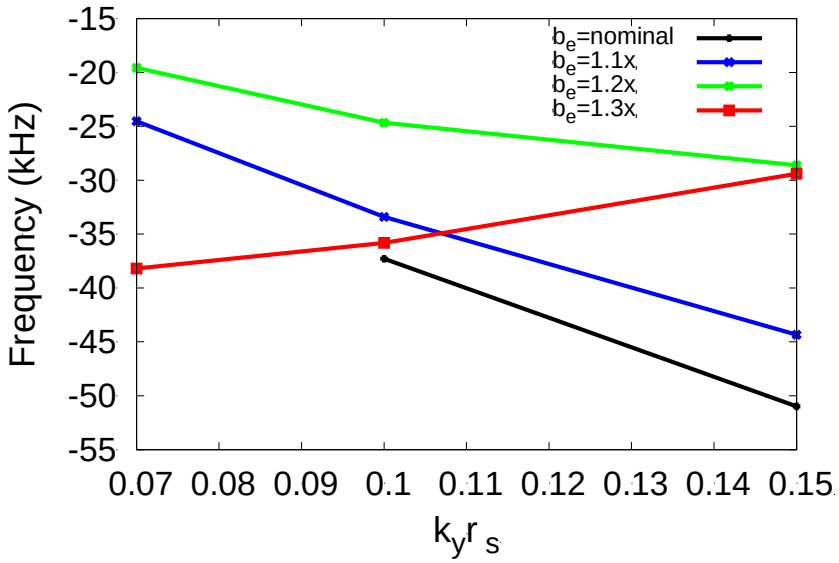

Figure 2.7 (g): Mode frequency (in lab frame) for $k_y\rho_s <= 0.15$ scan for DIIID 153764 base case at $\rho_t = 0.972$.

Can't fit in pedestal: unstable in small $k_x\rho_s$ range

We now consider the important question of whether these modes are likely to be able to fit inside a box of the width of a pedestal. Below, we show the growth rates vs. $k_x\rho_s$. Due to periodicity, within the ballooning framework, the range of $k_x\rho_s$ is between $-\pi \hat{s} k_y$ to $+\pi \hat{s} k_y$, where $\hat{s}$ is the shear in the coordinate ρ_t, $\hat{s} = (\rho_t/q)(dq/d\rho_t)$[24]. For the parameters of the DIIID 153764 base case at $\rho_t = 0.972$, this range is ±1.52. As can be seen, the mode is only unstable over a very small fraction of this range.

In normalized units of the gyroradii, the pedestal width is w ~ 15. Hence Δk_x w ~ 0.75, i.e., much less than 2. Hence, the mode likely cannot fit in the pedestal. This result agrees with global linear calculations, which fail to find a KBM in any of the pedestals considered. Hence, even though the mode appears in local linear calculations, it is apparently unable to fit within these narrow pedestals, so there is no actual instability.

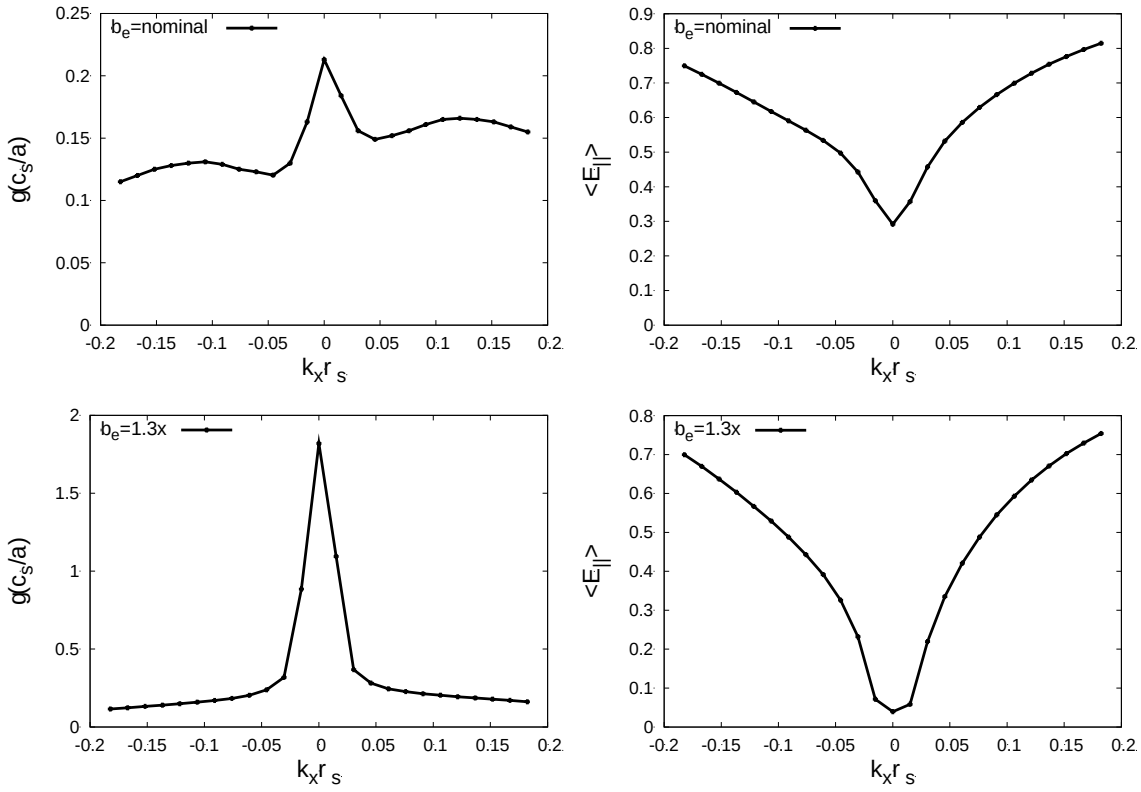

Figure 2.7 (h): Growth rate vs. (normalized) radial wavenumber $k_x\rho_s$, for both the nominal beta and 1.3 times this value, for the $k_y\rho_s$ of the measured fluctuation. The MHD-like mode only exists over a small range of $k_x\rho_s$, so that it cannot fit into a "box" of the width of a pedestal.

DIIID 98889 Local linear simulations

We have to increase β by a large factor, which is probably outside of the experiment error bars, to find MHD-like mode for DIIID 98889. Results from 1.6 times, 1.8 times and 2 times the nominal β at $\rho_t = 0.95$ are presented in Fig 2.8 (a-g). Missing results for $k_y\rho_s > 0.15$ and beta = 1.6 times and 1.8 times are not MTM or ITG modes and are thus not shown. The characteristics of the modes are similar to those for DIIID 153764/5 above.

Growth rates increase rapidly with β

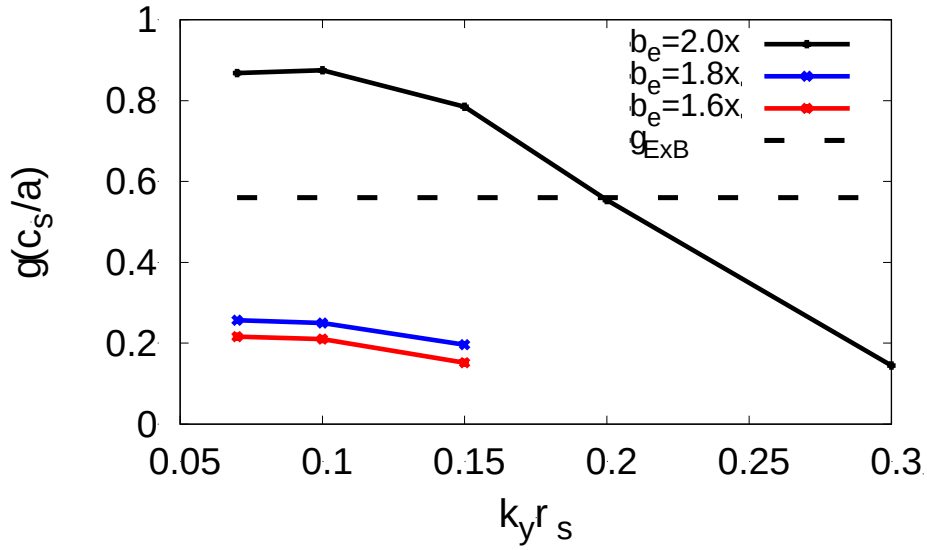

Figure 2.8 (a): Mode growth rates for $k_y\rho_s$ scan for DIIID 98889 at $\rho_t = 0.95$.

Strong parallel electric field $< E_{||} >$ cancellation

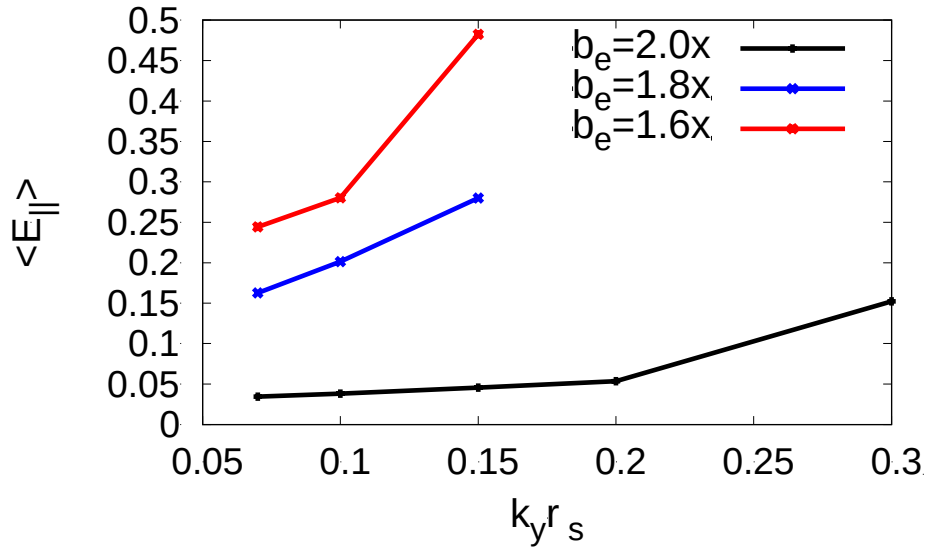

Figure 2.8 (b): $<E_{||}>$ for $k_y\rho_s$ scan for DIIID 98889 at $\rho_t = 0.95$.

Mainly electrostatic heat loss

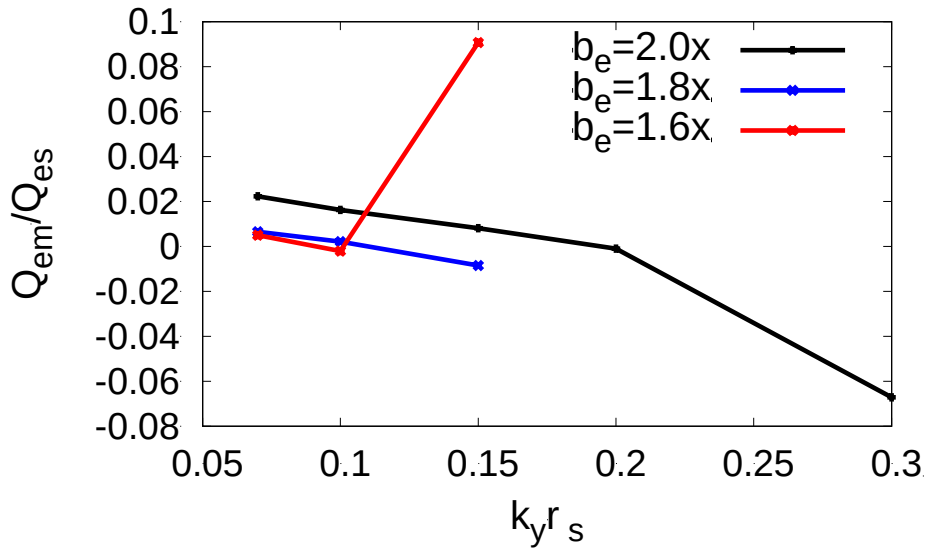

Figure 2.8 (c): Ratio of electromagnetic to electrostatic heat flux for $k_y\rho_s$ scan for DIIID 98889 at $\rho_t = 0.95$.

Transport Fingerprint: all diffusivities are comparable

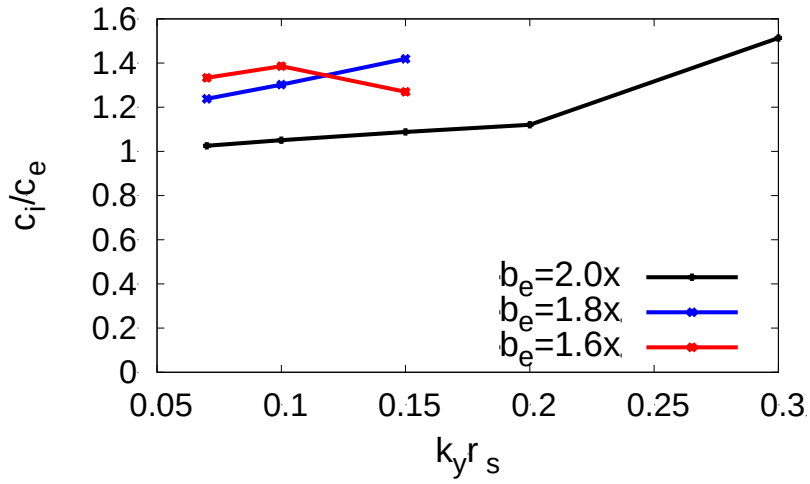

Figure 2.8 (d): Ratio of ion thermal diffusivity to electron thermal diffusivity for $k_y\rho_s$ scan for DIIID 98889 at $\rho_t = 0.95$.

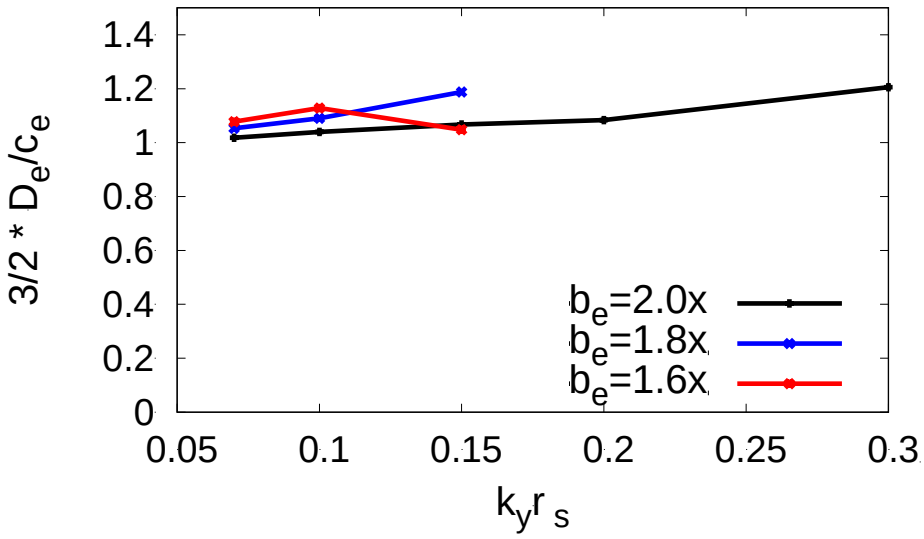

Figure 2.8 (e): Ratio of electron particle diffusivity to thermal diffusivity for $k_y\rho_s$ scan for DIIID 98889 at $\rho_t = 0.95$.

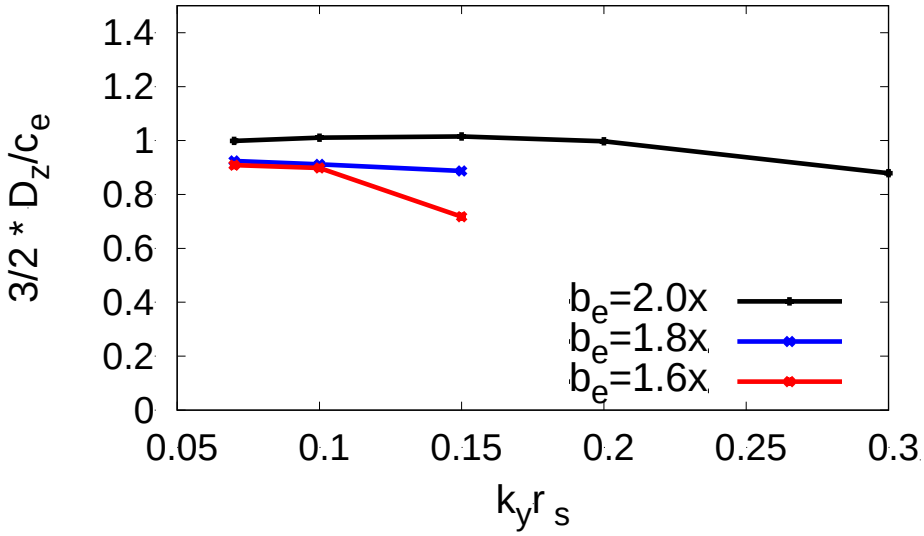

Figure 2.8 (f): Ratio of impurity particle diffusivity to electron thermal diffusivity for $k_y\rho_s$ scan for DIIID 98889 at $\rho_t = 0.95$.

Frequency too low to match observed QCFs

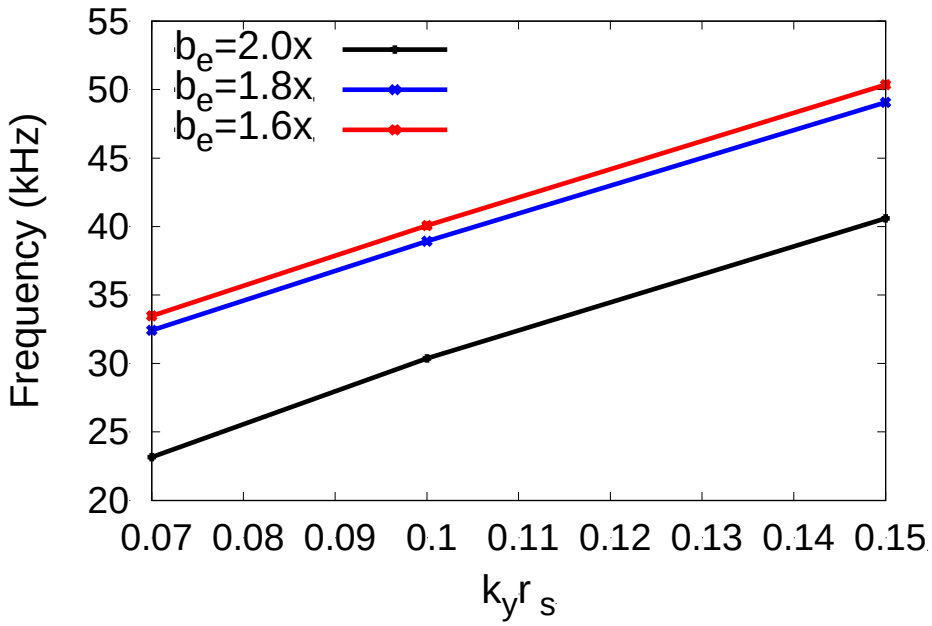

Figure 2.8 (g): Mode frequency in the lab frame for $k_y\rho_s$ scan for DIIID 98889 at ρ_t = 0.95.

Caveat: GENE missing relevant terms in MHD stability

However, GENE does not include the kink term (this has been added recently, but it remains to be benchmarked[33]). Also, the present version of the code uses Dirichlet boundary conditions at the plasma boundary, rather than matching to a vacuum magnetic solution. Both of these effects are stabilizing, so we cannot rule out the presence of an MHD-like instability in this pedestal.

Conclusion: KBM can't be the dominant energy transport agent

No KBM has been found in local or global calculations for shot 98889. However, the same caveats noted above apply, so we cannot rule out the presence of MHD-like instabilities for this case as well.

However, the transport fingerprint concept, can still be applied to these cases. This is inconsistent with the observed characteristics of the transport for both the 153674/5 shots

and the 98889 shot. In addition, the mode frequency is inconsistent with the fluctuation in shot 153674/5 that is strongly correlated with T_e evolution. Hence, we conclude that KBM are not the dominant energy transport agents for these shots.

MICRO-TEARING MODES MTM

We will find that MTM are indeed the likely agents responsible for transport in these shots. Hence, we consider their properties in gyrokinetic simulations in detail.

DIIID 153764/5 Local linear simulations

Growth rate higher than ExB shearing rate

We first consider local linear runs. These found MTM in both 153674 and 98889, in much of the range from the mid-pedestal to the top of pedestal. We show below results for toroidal mode numbers in the range around the observed fluctuation seen in 153674/5, which was at n = 13-14.

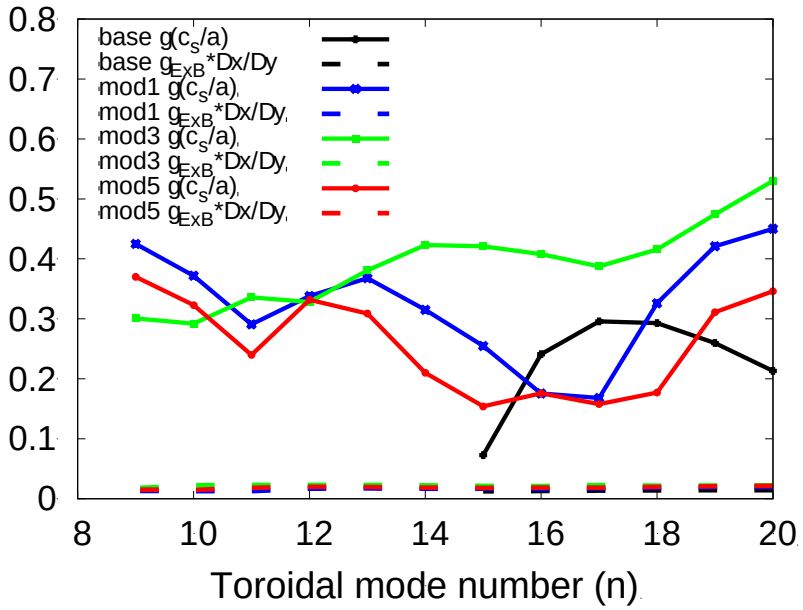

Figure 2.9 (a): Local linear growth rates of shot 153674/5 in the mid-pedestal range (ρ_t = 0.982). Results are also shown for the modified profiles at the same radial location.

For the base case, we show instabilities for $\theta_0 = -0.6$, which is close to the peak of γ as found by θ_0 scan (Fig 2.9 (h)). The modified profiles are more robustly unstable and have γ roughly independent of θ_0 (Fig 2.9(i), Fig 2.9(j), Fig 2.9(k)), so results for $\theta_0 = 0$ are shown.

We now estimate whether these local modes would be able to cause transport in the presence of the large ExB shear of the pedestal. For this, we compute the shearing rate, adjusted for the radial mode width $\Delta x/\Delta y$. Theory indicates that modes with short radial scales are more resistant to velocity shear.[25, 26, 27] This certainly applied to MTM, where the instability is driven in a relatively narrow current layer, with small $\Delta x/\Delta y$. To estimate the relative radial to poloidal scale length for these modes, we use the numerically computed eigenfunction average $\langle k_\perp^2 \rangle$ for the perturbed current, which is considerably larger than k_y^2. We estimate $\Delta x/\Delta y \sim (k_y^2/\langle k_\perp^2 \rangle)^{1/2}$. As can be seen above, this is quite small compared to the growth rates found. Hence, MTM are a candidate to explain pedestal transport in the presence of the large ExB shear.

Frequency in the lab frame is on the same order of QCFs

We now compare the frequencies of these modes to ω_e^* (computed with both density and temperature gradients). As can be seen in the Fig 2.9 (b), the modes do indeed track ω_e^* closely.

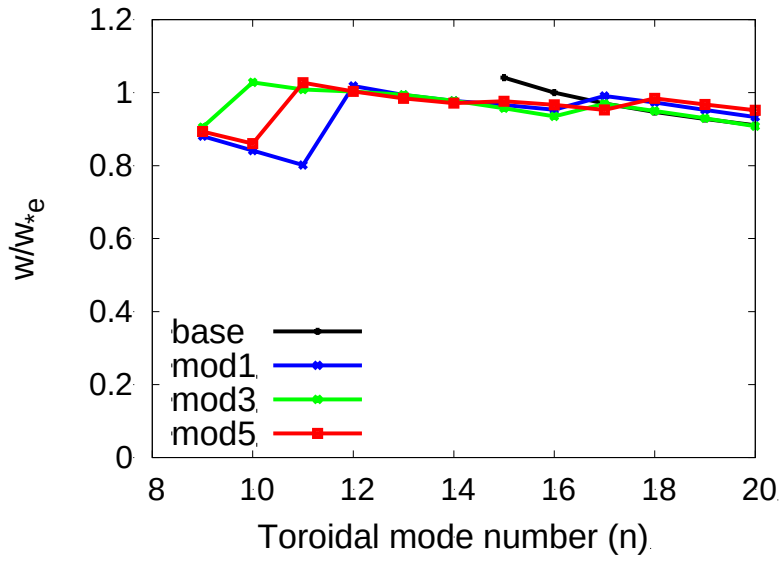

Figure 2.9 (b): Frequency of the MTM in local linear runs at the mid pedestal for 153674/5, normalized to ω_e^*; ω is close to ω_e^*.

We now consider the frequency of these modes in the lab frame, including the Doppler shift from the measured E_r. These are all strongly in the electron direction, as observed on magnetic diagnostics and BES. In the case of 153674, for the measured value of k_y, the frequency is about a factor of two higher than the observed QCF.

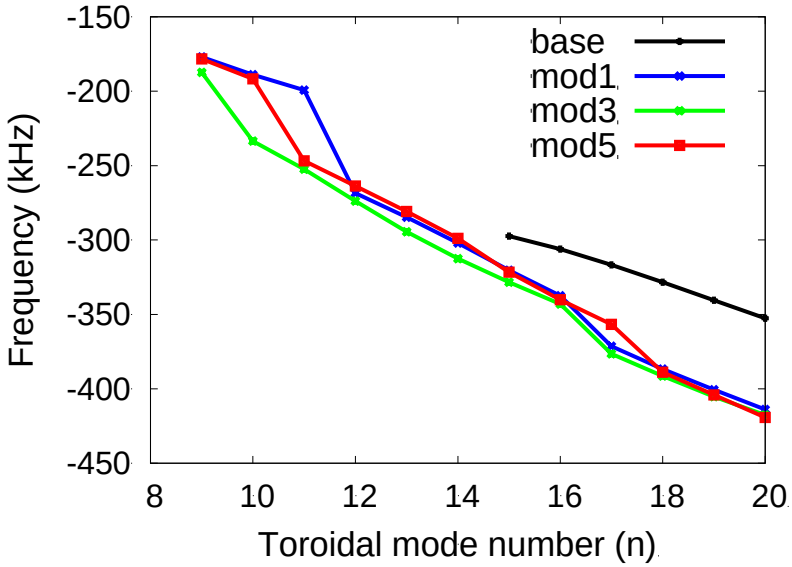

Figure 2.9 (c): Mode frequency (in lab frame) for DIIID 153764 at $\rho_t = 0.982$.

Mainly electromagnetic heat loss

We found the electromagnetic heat diffusivity strongly dominates, as expected for an MTM.

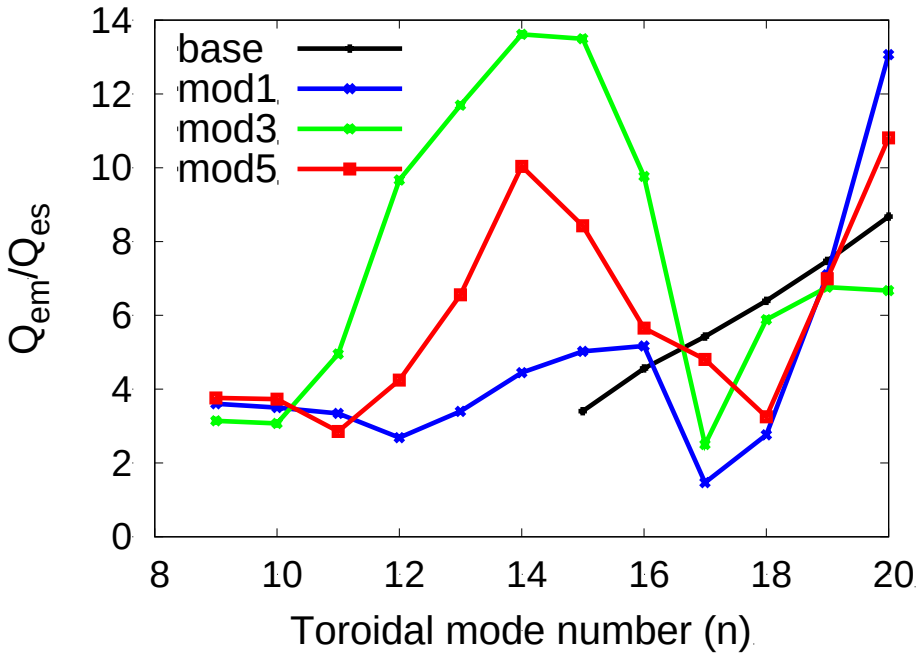

Figure 2.9 (d): Ratio of electromagnetic to electrostatic heat flux for toroidal mode number scan for DIIID 153764 at $\rho_t = 0.982$.

Transport Fingerprint: χ_e is the dominant diffusivity

We now turn to the fingerprints for these modes; χ_e is much larger than all other diffusivities.

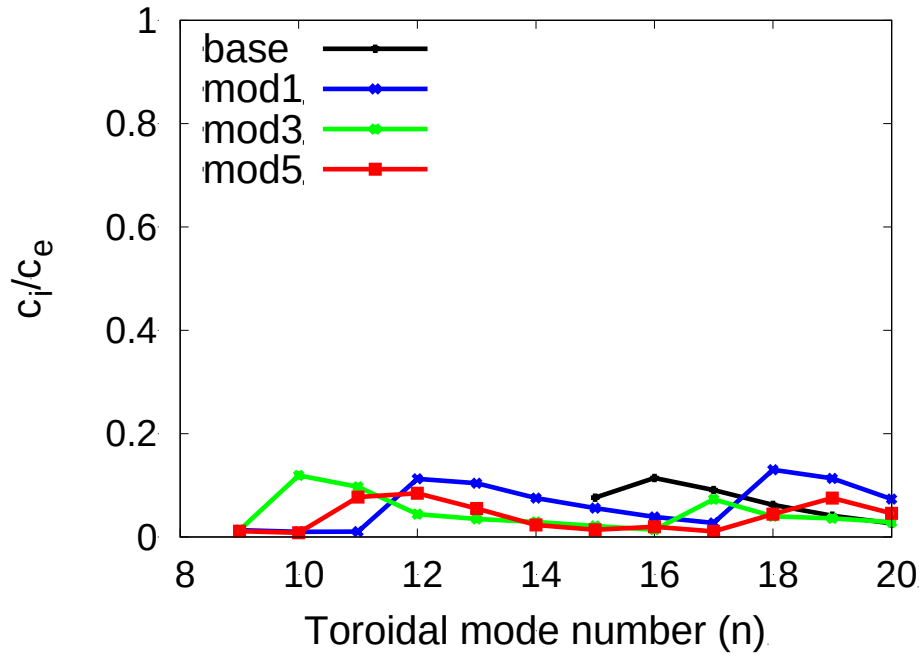

Figure 2.9 (e): Ratio of ion to electron thermal diffusivity for toroidal mode number scan for DIIID 153764 at $\rho_t = 0.982$.

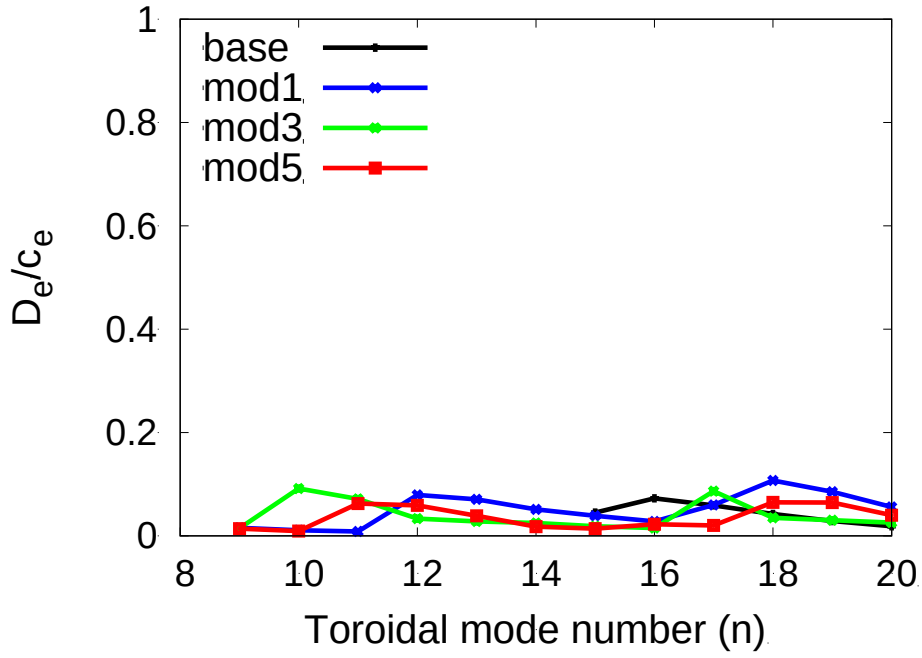

Figure 2.9 (f): Ratio of electron particle diffusivity to thermal diffusivity for toroidal mode number scan for DIIID 153764 at $\rho_t = 0.982$.

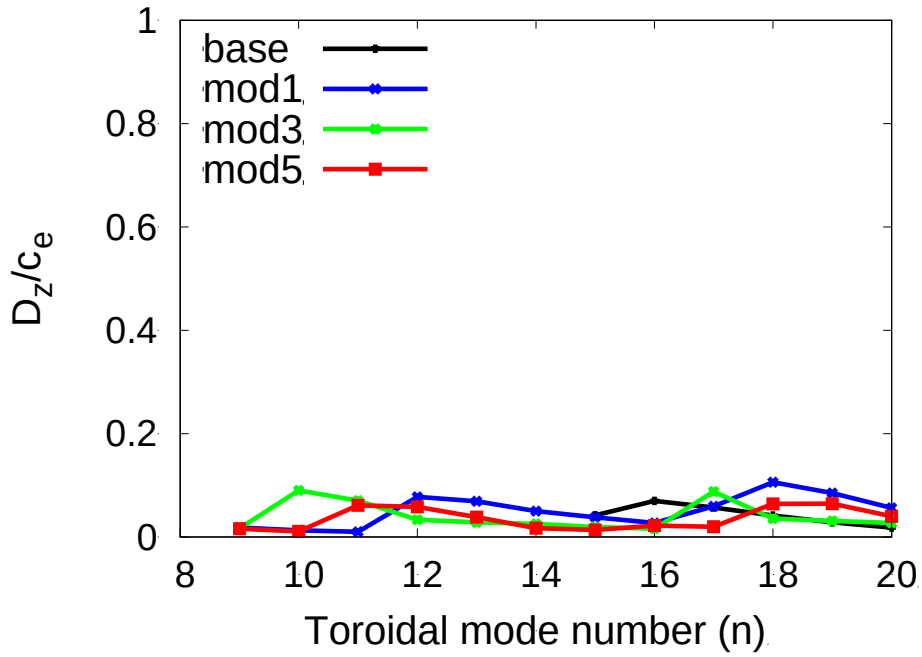

Figure 2.9 (g): Ratio of impurity diffusivity to electron thermal diffusivity for toroidal mode number scan for DIIID 153764 at $\rho_t = 0.982$.

Due to space, we do not show the fingerprints for shot 98889, but they are qualitatively the same as shown above.

Possible to fit in pedestal: unstable in a wide range of $k_x\rho_s$

We now consider $k_x\rho_s$ scans of the local linear runs. We start with 153674/5, for the unmodified profiles. For n = 17, there is a broad range of k_x unstable (Fig 2.9 (h)), with $\Delta k_x w \sim 4.5$. And indeed, global runs do find an instability at n = 17.

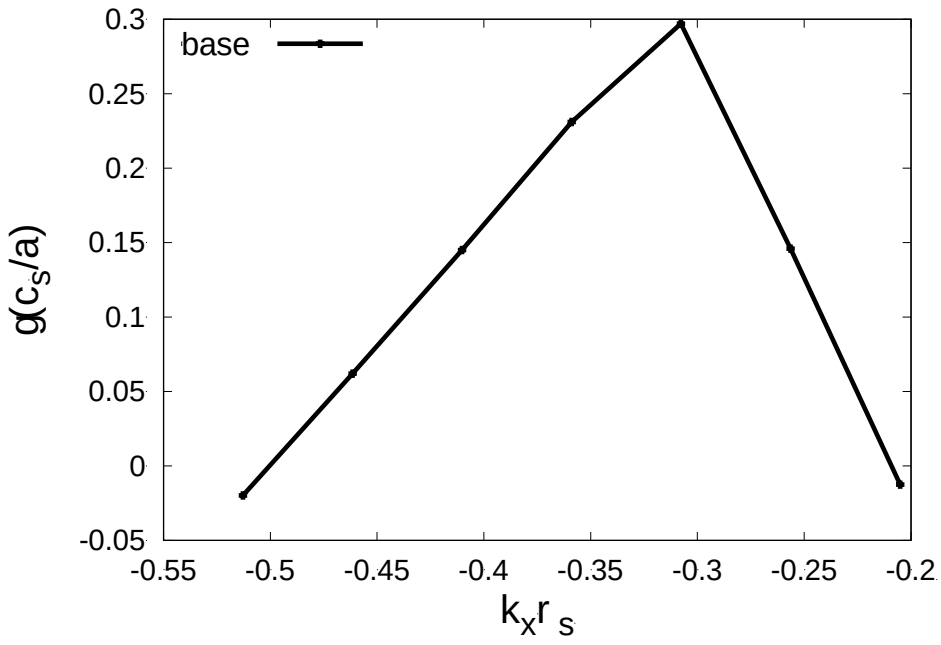

Figure 2.9 (h): Growth rate vs. (normalized) radial wavenumber $k_x\rho_s$ for DIIID 153764 base case at $\rho_t = 0.982$ for n = 17.

Now we consider the modified cases mod1, mod3 and mod5. These have MTM which are unstable across the whole range of $k_x\rho_s$, and there is little variation in the growth rate with $k_x\rho_s$. This is the behavior expected for slab-like modes, where toroidicity is not a dominant aspect of the instability drive. For these cases, Δk_x w ~ several times larger than needed to fit in the box. And indeed, global simulations find instabilities for some $k_y\rho_s$ in the range of local linear instability.

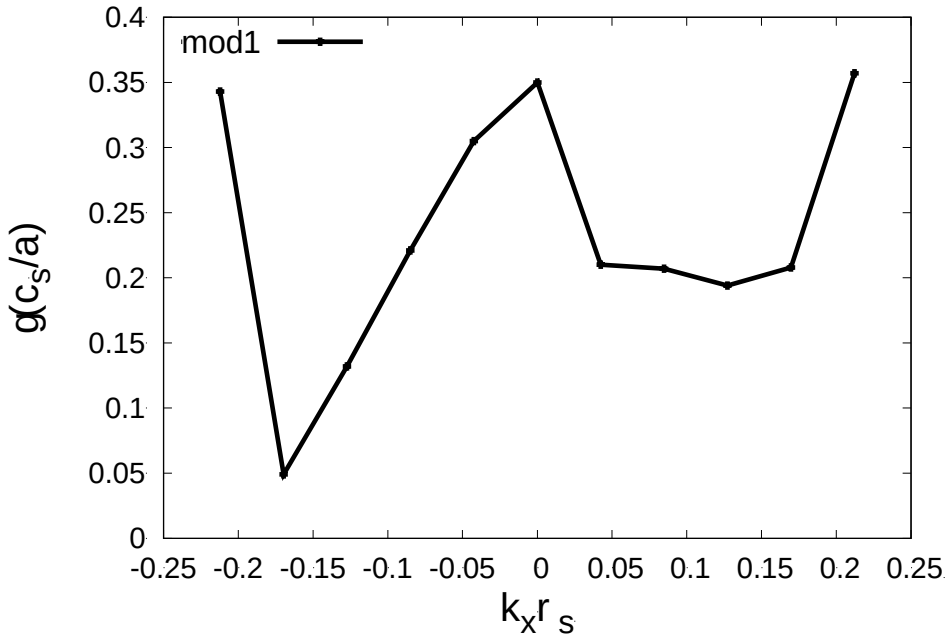

Figure 2.9 (i): Growth rate vs. (normalized) radial wavenumber $k_x\rho_s$ for DIIID 153764 mod1 case at $\rho_t = 0.982$ for n = 13.

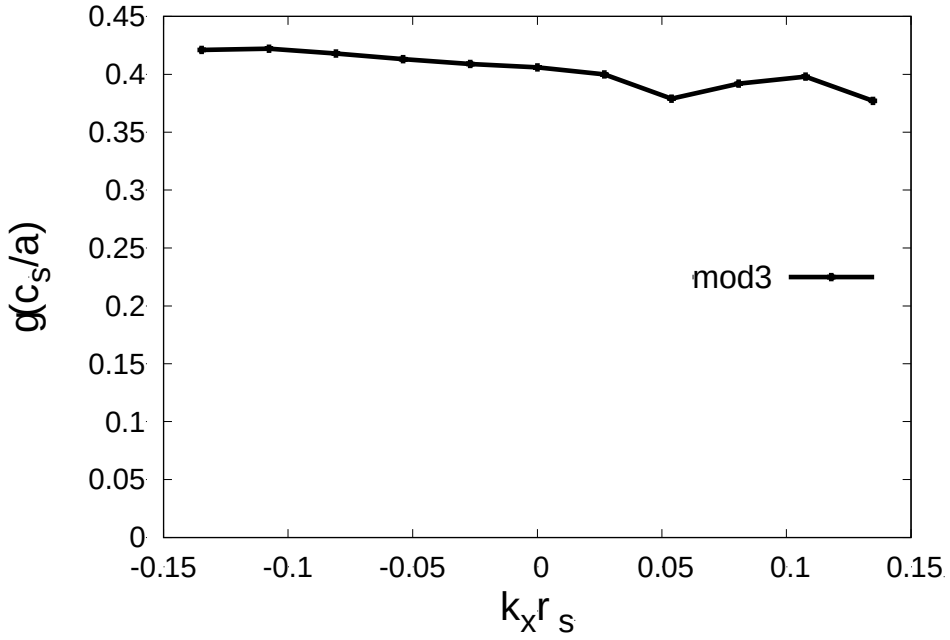

Figure 2.9 (j): Growth rate vs. (normalized) radial wavenumber $k_x\rho_s$ for DIIID 153764 mod3 case at $\rho_t = 0.982$ for n = 13.

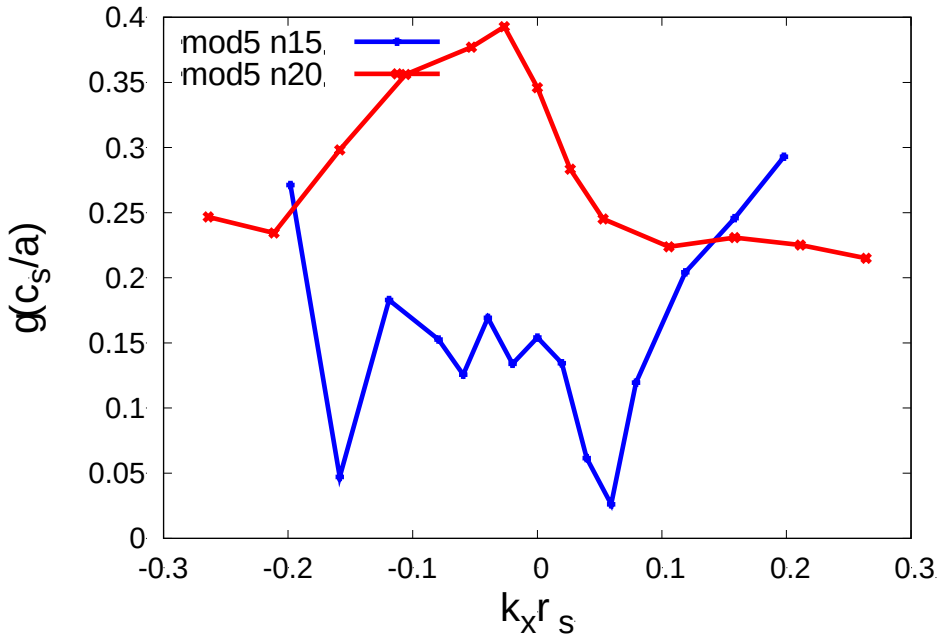

Figure 2.9 (k): Growth rate vs. (normalized) radial wavenumber $k_x\rho_s$ for DIIID 153764 mod5 case at $\rho_t = 0.982$ for n = 15 and n = 20.

For shot 98889, as well, MTM are unstable over a considerable range of $k_x\rho_s$, and Δk_x w is several times larger than needed to fit in the box. An example from local linear is ($\rho_t = 0.972$) is shown below; Global modes are found for these cases as well.

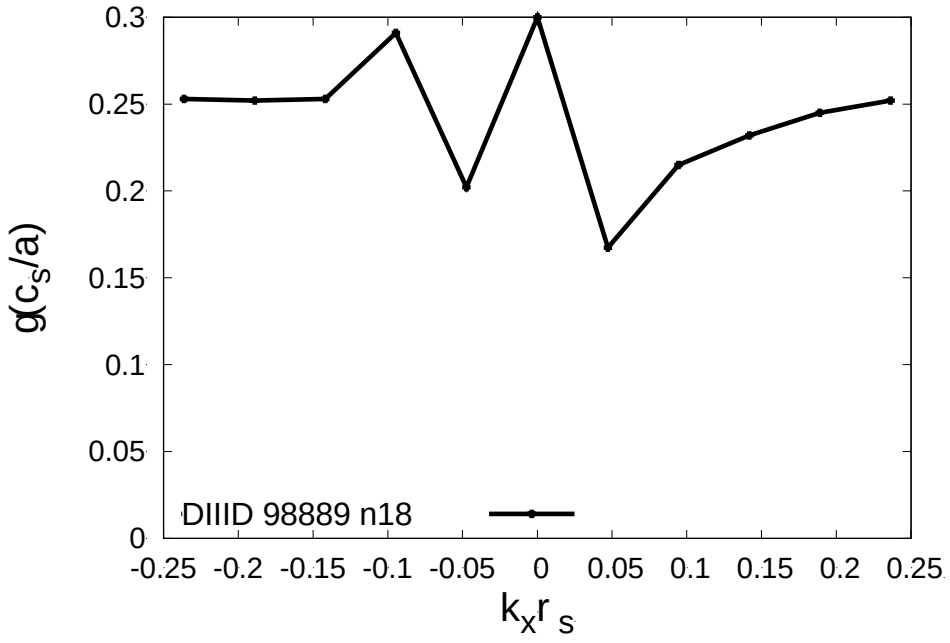

Figure 2.9 (l): Growth rate vs. (normalized) radial wavenumber $k_x\rho_s$ for DIIID 98889 at $\rho_t = 0.972$ for n = 18.

DIIID 153764/5 Global linear simulations

MTM unstable at discrete mode numbers

We now turn to global linear simulations of these modes. For shot 153674/5, there are instabilities found within the range toroidal mode number n from 10 to 20, for both the base case and the modified profiles. Surprisingly, however, these instabilities only occur for isolated, discrete values of n (see Fig 2.9 (m)). Based on the local runs, and the criterion, $\Delta k_x w > 2$, we would expect MTM to be globally unstable over a broad range of n numbers. We have not been able to discern any pattern for which n numbers are unstable in the global runs, and which are not.

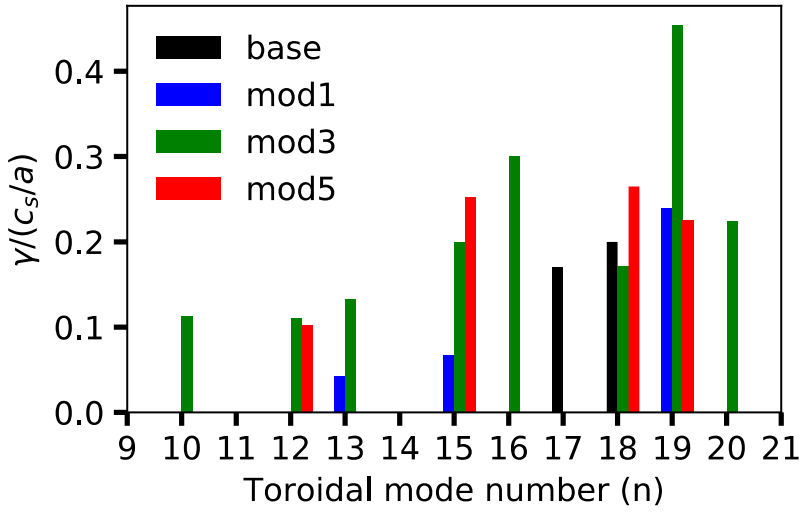

Figure 2.9 (m): Global linear growth rates of shot 153674/5 base case and the modified cases.

The qualitative character of the instability spectrum is surprising: the instabilities often appear at only two or three toroidal mode numbers in this range, and these n values are usually separated by several n values where no instabilities are found. We do not have a theoretical explanation for this unusual spectrum.

However, we note that the qualitative character of the spectrum found in global simulations is consistent with the observed character of the fluctuations. Instead of a broad band of fluctuation frequencies, the observed modes appear in discrete, fairly narrow frequency bands- Quasi Coherent Modes.

For some of the profile variations above, the dominant n number that is unstable is close to the observed QCF with n ~ 13-14. But we do not understand what types of profile variations lead to a particular n numbers being unstable.

Frequency in the lab frame is larger than observed QCFs

The frequency in the lab frame, shown in Fig 2.9(n), is about twice as high as the QCF observations. As we will see, nonlinear simulations bring the frequency much closer to the observed QCFs.

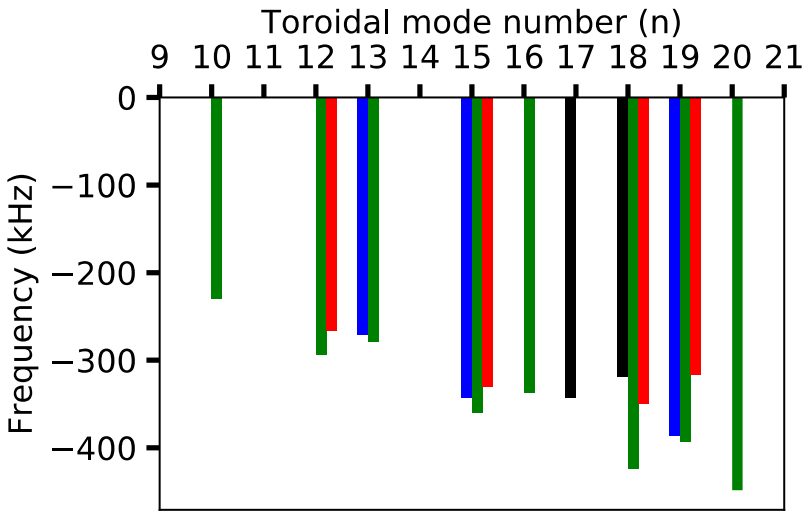

Figure 2.9 (n): Global linear frequencies in the lab frame of shot 153674/5 base case and the modified cases.

Transport Fingerprint similar to local linear MTM: χ_e is the dominant diffusivity

The quasilinear fingerprints of the global modes are qualitatively very similar to the local linear results (Table 2.1).

Case	Toroidal mode number (n)	χ_i / χ_e	$De/\chi e$	$Dz/\chi e$	Q_{es}/Q_{em}
base	17	0.049	0.026	0.017	0.086
base	18	0.097	0.033	0.029	0.216
mod1	13	-0.021	-0.002	0.019	0.037
mod1	15	0.035	0.045	0.010	-0.094
mod1	19	0.067	0.031	0.028	0.105
mod3	10	-0.008	0.008	0.004	0.276
mod3	12	0.052	0.035	0.009	-0.026
mod3	13	0.014	0.012	0.009	-0.005
mod3	15	0.059	0.044	0.016	-0.061
mod3	16	0.026	0.031	0.014	0.085
mod3	18	0.028	0.043	0.007	-0.002
mod3	19	0.088	0.048	0.039	0.059
mod3	20	0.008	0.009	0.013	0.006
mod5	12	0.049	0.020	0.011	0.194
mod5	15	0.010	0.038	0.011	-0.073
mod5	18	0.074	0.035	0.021	-0.017
mod5	19	0.050	0.021	0.014	0.182

Table 2.1: Transport Fingerprint for global linear MTM.

Global linear MTM not affected by ExB shear

Finally, we consider the effect of the E_r profile. Local linear results indicated that ExB shear should not be able to suppress these modes. Global simulations come to qualitatively the same conclusion (Table 2.2).

Case	Toroidal mode number (n)	ExB shear	Growth rate $\gamma(c_s/a)$
mod1	13	with	0.042
mod1	13	without	0.094
mod1	15	with	0.067
mod1	15	without	0.027
mod5	12	with	0.102
mod5	12	without	0.138
mod5	15	with	0.252
mod5	15	without	0.21

Table 2.2: Global MTM with and without ExB shear

DIIID 98889 Local linear simulations

We now turn to MTM linear results for shot 98889. We start with local linear results. MTM are found at most radii. A typical example is shown below.

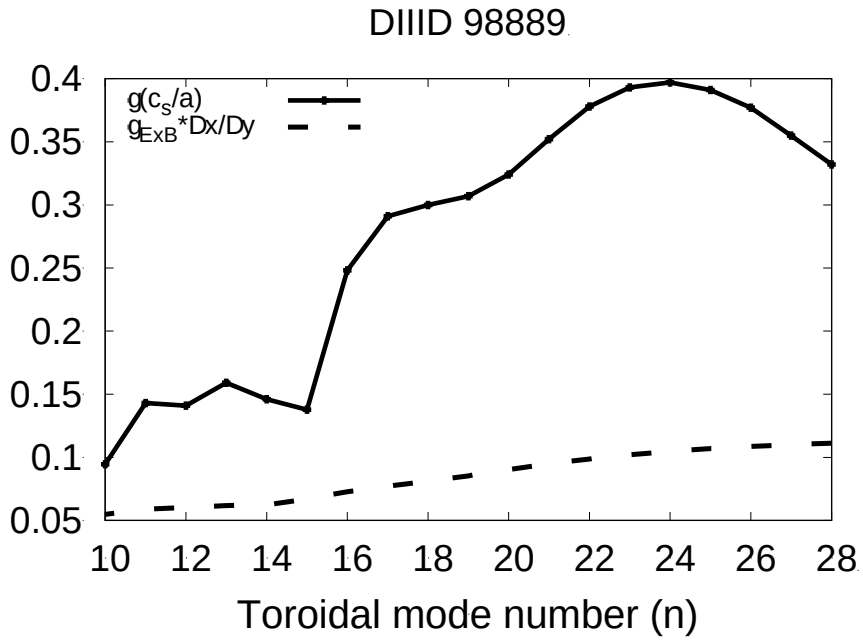

Figure 2.10 (a): Local linear toroidal mode number scan for DIIID 98889 at $\rho_t = 0.972$.

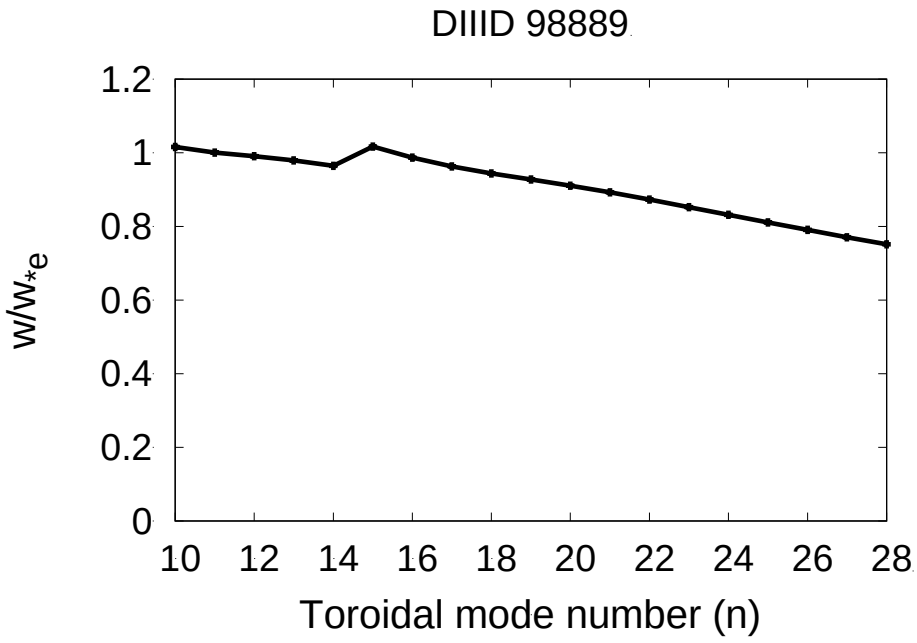

Figure 2.10 (b): Frequencies track ω_e* for toroidal mode number scan for DIIID 98889 at $\rho_t = 0.972$.

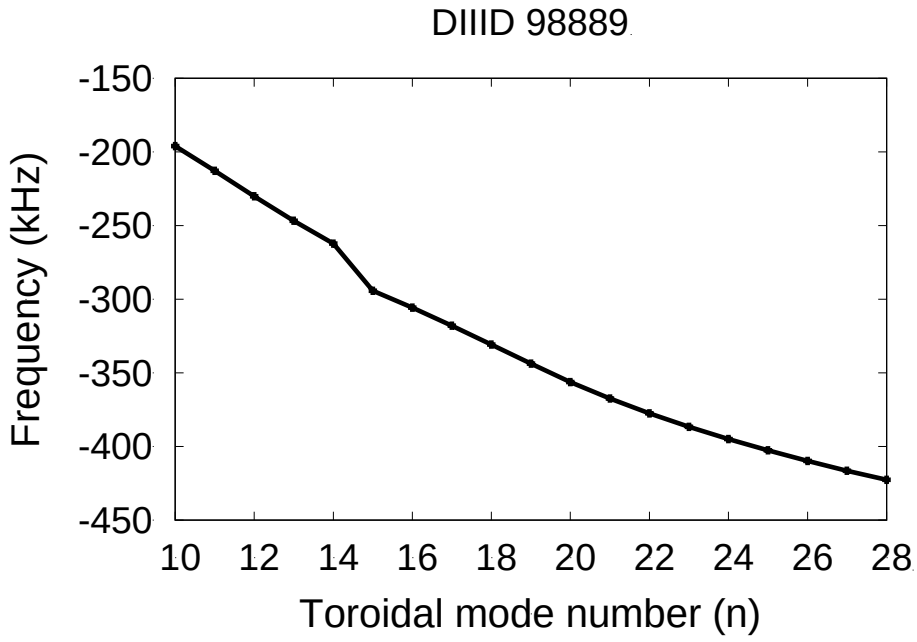

Figure 2.10 (c): Frequency in the lab frame for toroidal mode number scan for DIIID 98889 at $\rho_t = 0.972$.

The frequency in the lab frame is in the same range as the QCF observed on the magnetic spectrogram (f ~ 220 kHz and 180 kHz), or somewhat higher.

The transport fingerprints of the MTM are shown below. The electron heat diffusivity is strongly dominant.

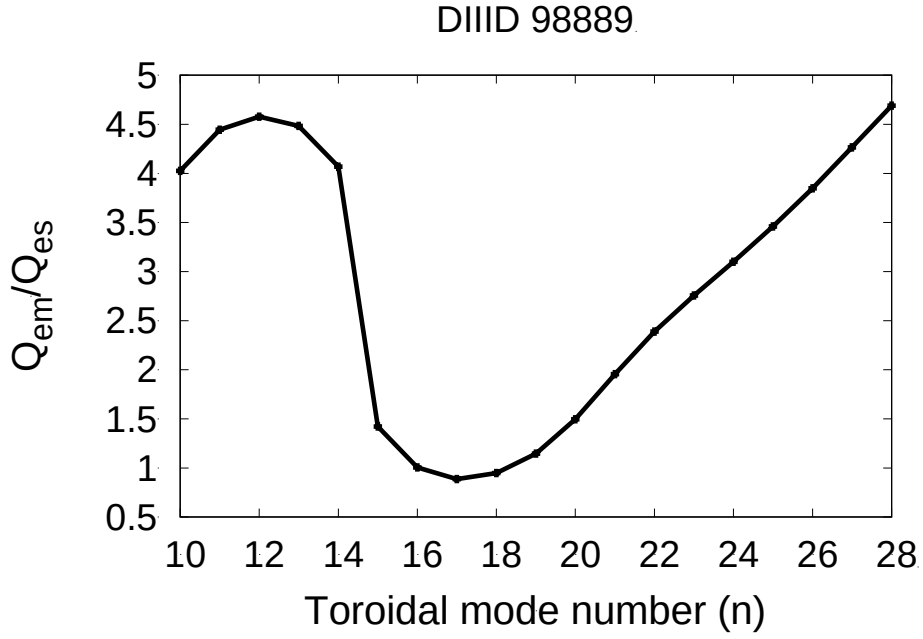

Figure 2.10 (d) The ratio of quasilinear electromagnetic to electrostatic heat flux for toroidal mode number scan for DIIID 98889 at $\rho_t = 0.972$. Electromagnetic dominates for most n.

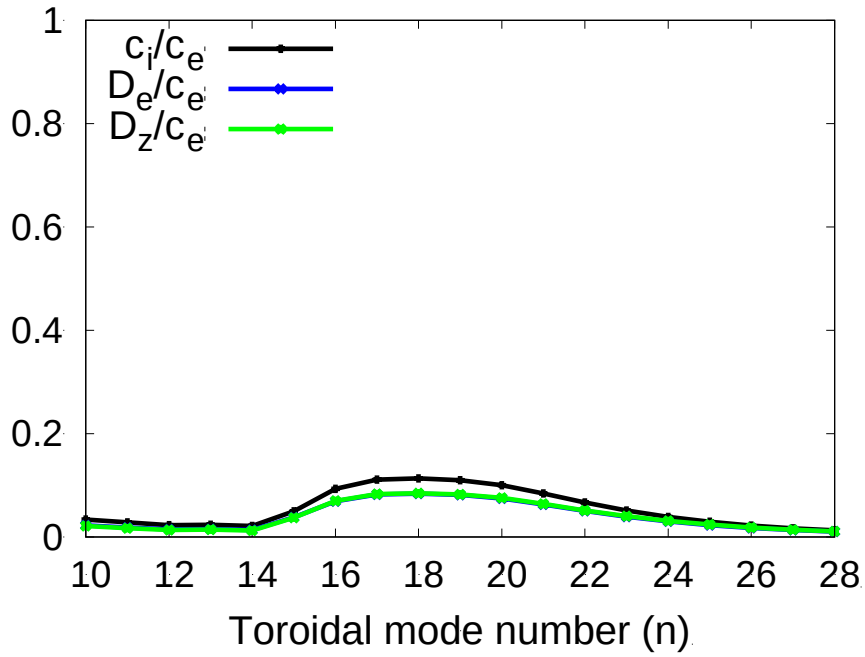

Figure 2.10 (e): Transport fingerprints for toroidal mode number scan for DIIID 98889 at $\rho_t = 0.972$.

DIIID 98889 Global linear simulations

Toroidal mode number (n)	Mode type	Growth rate $\gamma(c_s/a)$	Frequency in lab frame (kHz)
12	ES	0.005	-58
13	ES	0.016	-61
14	ES	0.025	-62.
15	ES	0.035	-64
16	MTM	0.18	-291
17	ES	0.046	-67
18	MTM	0.294	-331
19	ES	0.086	-70
20	ES	0.1	-72
21	MTM	0.152	-361
22	ES	0.124	-76

Table 2.3: Table of Global MTM versus mode number n for shot 98889.

We now turn to global linear simulations for shot 98889. There is unstable MTM for n = 16, 18 and 21 (Table 2.3). As was the case for shot 153674/5, the unstable n numbers are separated by stable n numbers.

For shot 98889, there is no experimental determination of the k_y, but, the f values for n =16 and 18 are about 1.5 times the high f bands on the magnetic spectrogram.

As we will see, nonlinear simulations of these modes show a strong nonlinear downshift of the frequency, to within ~ 40% of the observed values.

Global nonlinear MTM

For both shot 153674 and 98889, the full profile variation in the pedestal region was included in the global simulations. The outer simulation boundary was close to the separatrix ($\rho_t \sim 0.999$, where ρ_t is the normalized toroidal flux.). For 153674, the inner simulation boundary was $\rho_t = 0.95$, whereas for 98889, because the shot has a slightly wider pedestal, it was $\rho_t = 0.94$.

Both experiment shots find Quasi-Coherent Fluctuations. Hence, we choose nonlinear simulations that include a single n number corresponding to the QCF, as well as n=0. The simulations include nonlinear effects that are expected to be crucial saturation mechanisms for ion scale modes:

1) Coupling of the instability to zonal flows and GAMs

2) Flattening of equilibrium profiles near the mode maximum, or in the vicinity of rational surfaces.

Unfortunately, nonlinear electromagnetic global GENE simulations are subject to a numerical instability, which has occurred in many contexts. It manifests some time after a saturated phase is reached, after which a very low k mode begins to grow at an unphysically rapid rate. The nonlinear simulations here find this same instability. Hence, the saturated phase has only a finite length before the numerical instability arises. An example is Fig 2.11(a). Values for the flux and frequency are taken by averaging over the

time interval of apparent saturation, as shown. Also shown on Fig 2.11(a) is a blue line recording a reduced β (0.8 times the nominal value) simulation that started from a checkpoint before this numerical instability and ran with higher velocity space velocity (~1.5 times in both nv and nw) which avoids the numerical instability. Since the linear growth rate decreases by less than 20% with reduced beta, we use the result as a proxy to what would happen for the nonlinearly saturated state of the nominal β run if there were no numerical instability.

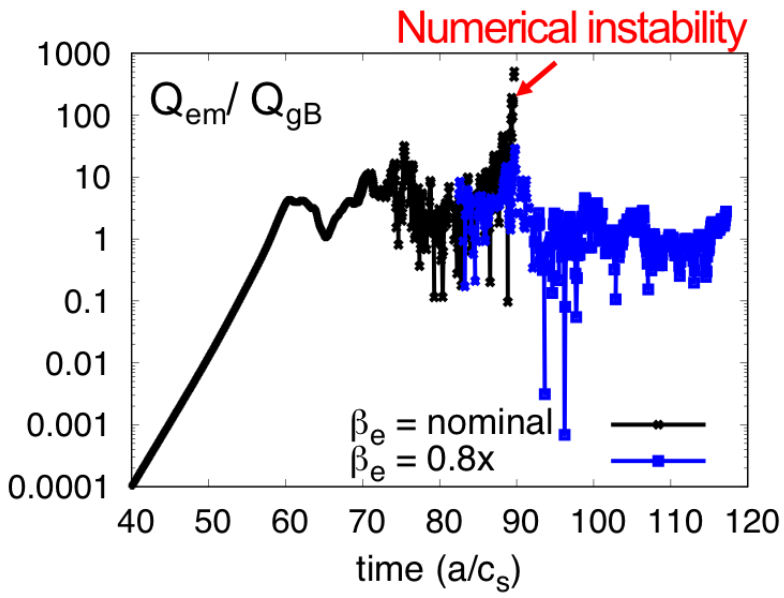

Figure 2.11 (a): Time evolution of the space averaged heat flux in GENE, showing the linear growth phase, nonlinear saturation phase, and nonlinear instability phase for the nominal β simulation (Black). Reduced β simulation with longer saturation phase is also shown (Blue).

Significant profile flattening of T_e occurs in the simulation. This is an important saturation mechanism. An example is shown in Fig 2.11(b). However, profiles of other plasma quantities are left nearly unaffected. Hence, as expected, nonlinear MTM cause mainly electron thermal transport.

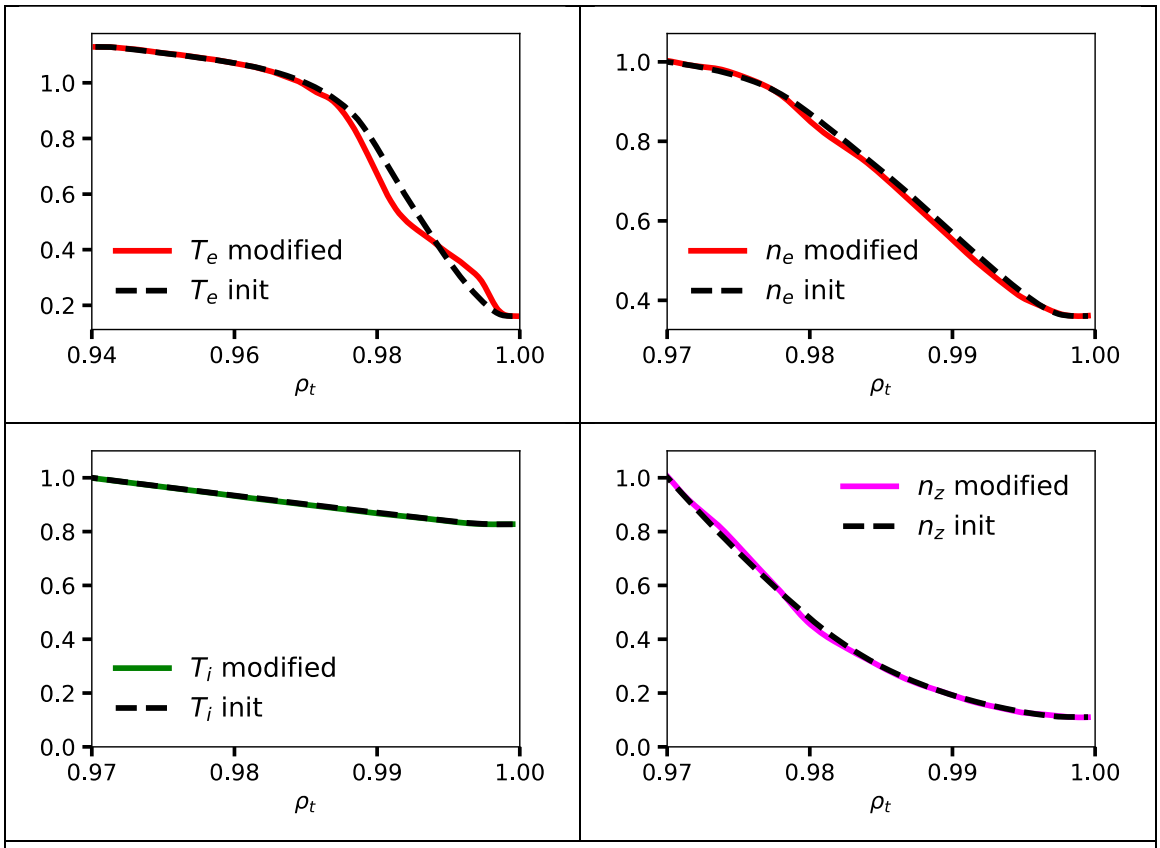

Figure 2.11(b): Profile modifications in nonlinear MTM simulations. Shown is a typical case, mod5 n=15. Note that only the T_e profile is significantly affected. This is consistent with the inter-ELM profile evolution seen on shot 153674/5. Dynamic profiles (solid line) from nonlinear simulation are compared to the equilibrium profiles (dashed line).

The nonlinear heat flux varies in the pedestal. A typical heat flux profile is shown in Fig 2.11(c) or for mod5, n=15.

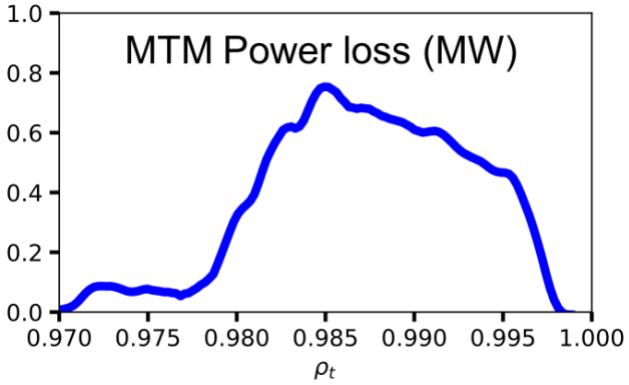

Figure 2.11(c): Heat flux profile in the pedestal averaged in the nonlinearly saturated state for DIIID 153764 mod5 case, n=15.

The magnitude of the maximum heat loss is ~ 0.8 MW. Together with heat loss from ETG ~ 1.4 MW (Table 2.5), the total of heat fluxes from the unstable modes is about 2 MW. Hence, the nonlinear simulations indicate that MTM can transport part of the heating power in the Diallo shot.

Next, we discuss the power balance from DIII-D 98889. We run nonlinear simulations for n = 16 and 18 which are unstable MTM modes as found in the global linear simulations (Table 2.3). The power loss profile calculated from the nonlinear saturation state for both n = 16 and n = 18 is shown in Fig 2.11(d). Adding the power loss from the two modes together, total power loss from MTM turbulence is about 1.6 MW. This is very close to match the experimental power loss of 1.8 MW. Nonlinear ETG simulations on several location of DIII-D 98889 (low η_e) has found low heat loss, about 0.1 – 0.3 MW. Therefore, MTM plus a small contribution from ETG is the dominant heat transport process in DIII-D pedestal.

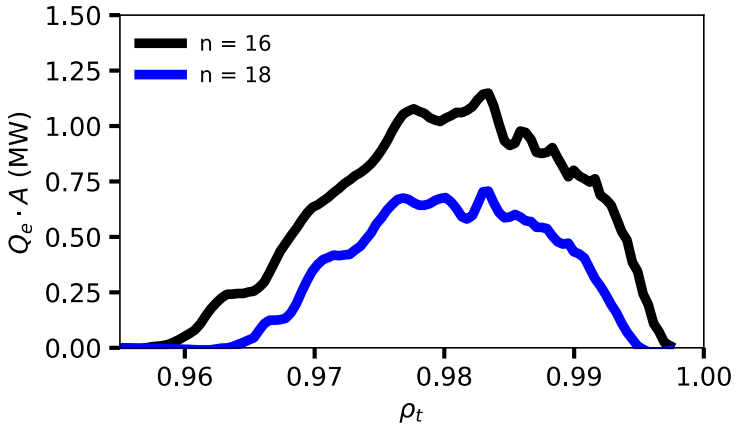

Figure 2.11(d): Heat flux profile in the pedestal averaged in the nonlinearly saturated state for DIIID 98889, n=16 and n=18.

Sometimes in the nonlinear simulations, we see a mode's heat flux nonlinearly crash down to very low values after reaching the nonlinear saturation state. We suspect this nonlinear crash is caused by the mode flattening of the T_e gradient to be below the stability

threshold therefore turning itself into a stable mode. An example of this nonlinear simulation is for the n = 13 mode on mod1 case (Fig 12(e)).

A summary of the results for selected nonlinear MTM simulations we performed are in Table 2.4. In this table, peak heat loss values are computed from the nonlinear saturation phase before numerical instability or after the nonlinear crash.

Case	Toroidal mode number (n)	Peak heat loss (MW)	Frequency in lab frame (kHz)
base	17	1.7	-255
mod1	13	0.54	-204
mod1	15	1.8	-262
mod3	15	2.1	-270
mod5	12	0.09	-195
mod5	15	0.8	-200

Table 2.4: Summary of nonlinear MTM simulation results.

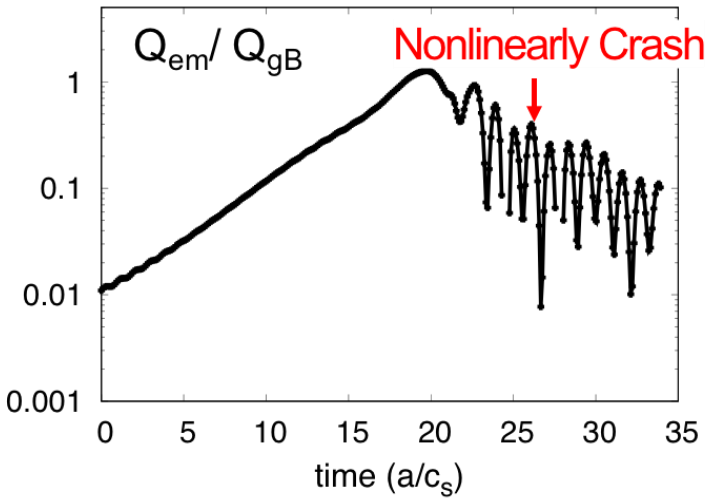

Figure 2.11 (e): Time evolution of the space averaged heat flux in GENE, showing the linear growth phase, nonlinearly crashing phase for mod1, n = 13.

Because flattening of T_e is an important mechanism, it is likely that existing non-linear gyrokinetic codes (including GENE and others) do not include complete enough physics to quantitatively describe the saturation. Specifically

1) By flattening the temperature profile, the bootstrap current in the equilibrium is changed, which should change the magnetic shear. However, no present gyrokinetic code updates the magnetic equilibrium to take this into account.

2) The modified T_e profile changes the T_e gradient, and therefore changes ETG transport in the pedestal. As shown in the section on ETG, the magnitude of ETG transport is significant. Hence, a physically correct description of the T_e profile evolution from MTM must also include the ETG transport.

Such multi-scale simulations would probably take several tens of millions of CPU hours, which is extraordinarily expensive.

Furthermore, the nonlinear results found here are sensitive to the initial profiles, with substantial variation in the results for profile changes within the error bars. Hence, one would have to run several nonlinear simulations to test sensitivity. This would be prohibitive for multiple multi-scale simulations.

Hence, with existing nonlinear gyrokinetic codes, including GENE, results for heat fluxes and frequencies with saturated QCFs from MTM can only be considered as qualitative. The most that can be said is that some combination of MTM and ETG appear capable of matching power balance, and frequencies appear to be in the correct range to explain the QCF.

Since only qualitative results are possible from nonlinear simulations, qualitative concepts such as the transport fingerprint are extremely important as a way to constrain the possible instabilities so that conclusions can be made about the modes that are responsible for transport.

ELECTROSTATIC MODES

High k_y ETG modes

We first consider modes with $k_y\rho_i < 1$: the high k_y ETG modes.

These modes have already been found to produce significant transport in H-mode pedestals.[32, 6, 7, 8].

ETG not suppressed by ExB shear

The growth rates of the modes are an order of magnitude higher than the ExB shearing rate (γ_{ExB} is ~ 1 for both these pedestals, in the normalized units of GENE). Hence, these modes are not suppressed in pedestals.

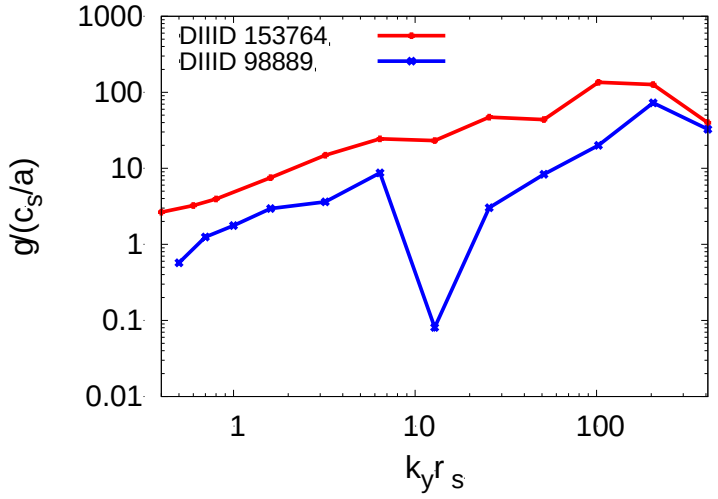

Figure 2.12 (a): Growth rates of ETG modes at mid-pedestal locations for the DIII-D pedestals.

Transport Fingerprint: χ_e is the dominant diffusivity

Because the ions are adiabatic, it is expected that they produce primarily electron thermal transport. We find that this is indeed true for these DIII-D pedestals, where local linear runs for these modes find that the quasilinear transport strongly conforms to this.

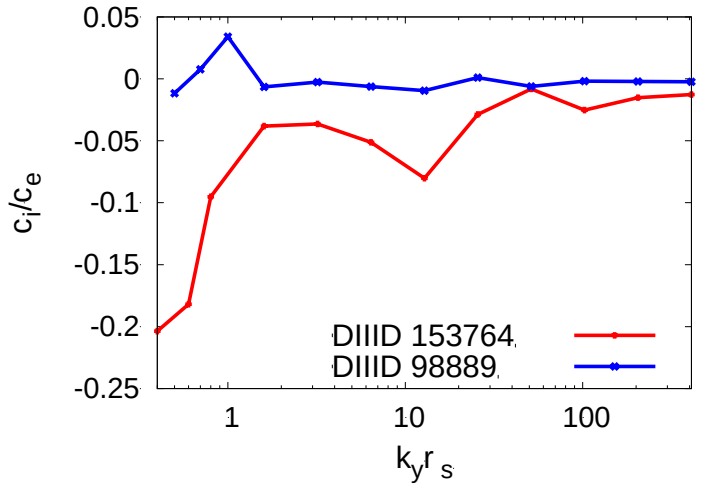

Figure 2.12 (b): Ratio of ion to electron thermal diffusivity of ETG modes at mid-pedestal locations for the DIII-D pedestals.

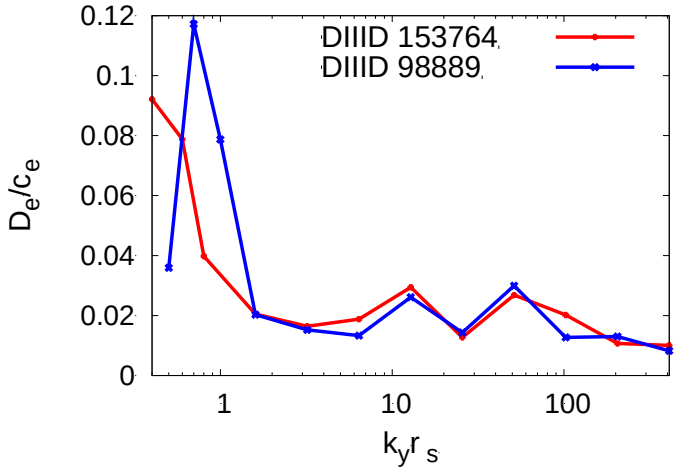

Figure 2.12 (c): Ratio of electron particle to thermal diffusivity of ETG modes at mid-pedestal locations for the DIII-D pedestals.

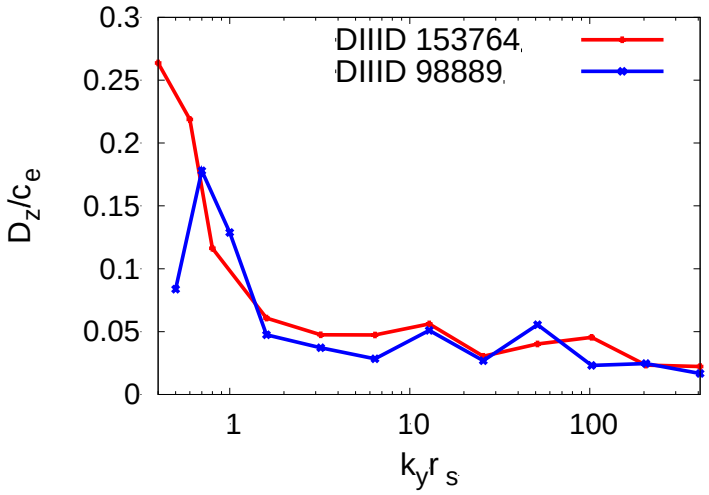

Figure 2.12 (d): Ratio of impurity diffusivity to electron thermal diffusivity of ETG modes at mid-pedestal locations for the DIII-D pedestals.

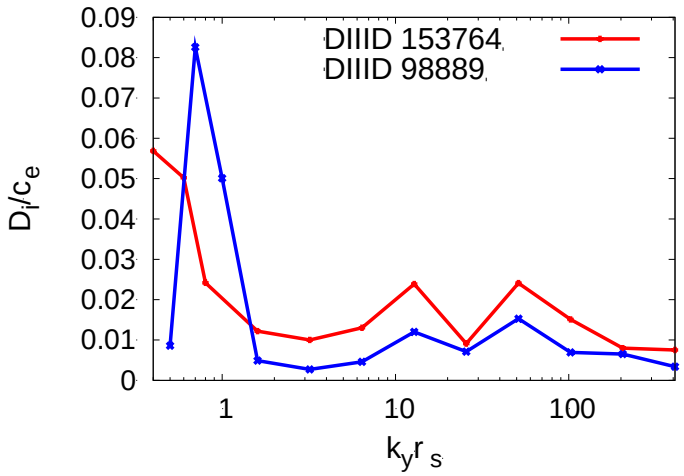

Figure 2.12 (e): Ratio of ion particle diffusivity to electron thermal diffusivity of ETG modes at mid-pedestal locations for the DIII-D pedestals.

In view of the mode scale is so short, and that ions are nearly adiabatic, it is conventional to find the heat flux from these modes by using local nonlinear simulations with adiabatic ions.

For shot 153784/5, the heat loss in the mid pedestal region is significant. The total transport through these pedestals is approximately 3 MW (A. Diallo and R. Groebner,

private communication). For the modified profiles, the ETG transport ranges from ~ 0.9 MW to 5 MW. Because these profile variations are likely within the error bars, from only the consideration of power balance, ETG are capable of causing transporting even all of the heating power in the middle of this pedestal.

Since the QCF is observed to be highly correlated with the heat transport, we expect that MTM also transport much of the heating power. And indeed, nonlinear simulations of coherent MTMs find that they can account for almost all the heat loss. Within the error bars of the profiles of these profiles, it is not possible to determine the relative amounts of the heat loss from MTM and ETG. Most likely both are significant.

Nonlinear ETG: Significant electron heat loss candidate

Some details of the nonlinear ETG runs are given below.

Case	ρ_t	η_e	τ	$\hat{s}$	Q_{es} (WM)
base	0.982	1.78	1.16	1.42	0.89
mod1	0.982	2.40	1.11	0.76	4.97
mod3	0.982	2.13	1.11	0.48	3.35
mod5	0.982	1.82	1.13	0.63	1.39

Table 2.5: Summary of nonlinear ETG simulation results.

The spectrum is well resolved by the spectral modes used in the simulation. As an example, see below, that the heat flux vanishes at the maximum values of the k_x and k_y that were simulated.

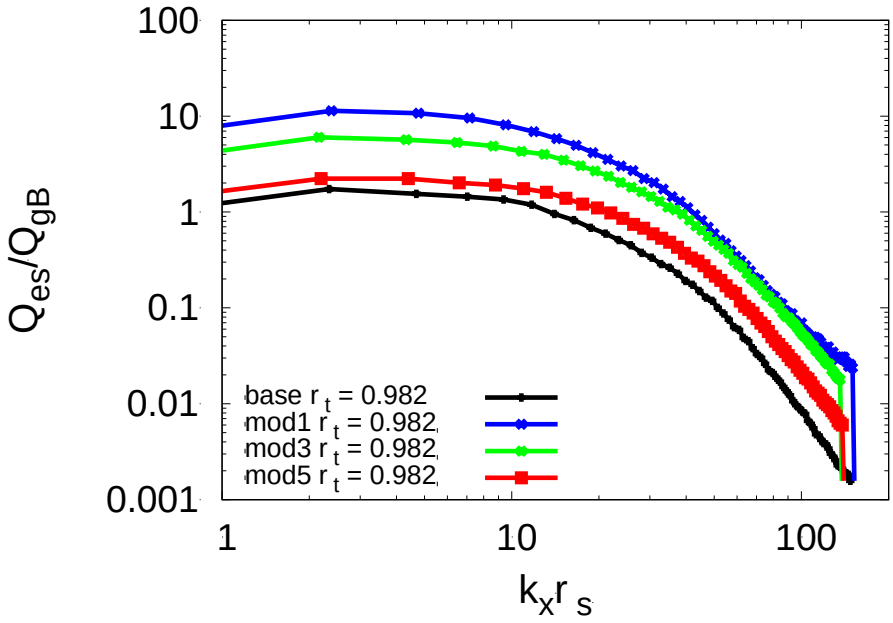

Figure 2.13 (a): Heat flux spectra versus $k_x\rho_s$ for nonlinear ETG simulations.

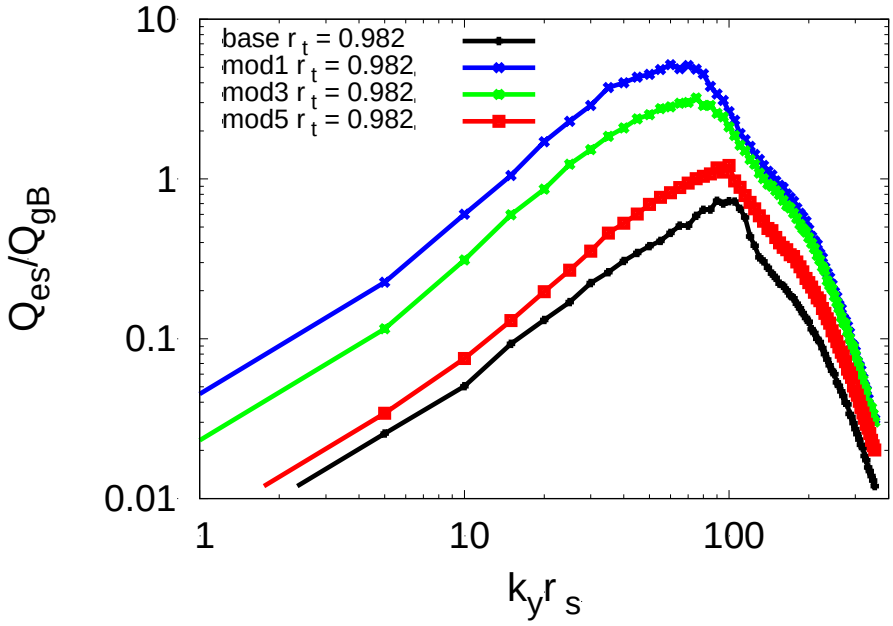

Figure 2.13 (b): Heat flux spectrum versus $k_y\rho_s$ for nonlinear ETG simulations.

TEM/ETG modes

In the core in the range of with $k_y\rho_s < 1$, ITG/TEM modes are the dominant instabilities. For pedestal parameters, as has been found previously[8, 7], ITG modes are more slab like, and are driven by $\eta_i = d \log T_i / d \log n$. Instabilities usually require $\eta_i \sim 1$ or more. But for shot 153674, η_i is significantly less than one over nearly the entire pedestal. The same is close to true for shot 98889, except, at the top of the pedestal $\eta_i \sim 1$. Hence, we do not find ITG-like modes for these shots, except near the pedestal top of 98889.

The dominant electron instabilities can be considered a hybrid between Trapped Electron Modes (TEM) and Electron Temperature Gradient (ETG) modes. As discussed previously[4], for pedestal parameters, the dominant electron driven modes for $k_y\rho_s < 1$ can be ETG-like modes, since instabilities with $k_x\rho_s >> 1$ can arise. These modes can also have mode frequencies less than, or of order, the electron bounce frequency ω_b. Hence, we refer to these modes as TEM/ETG modes, and they are the dominant instabilities found here. We discuss these modes first, and then turn to the ITG/TEM modes found at the pedestal top of 98889.

Local linear simulations

TEM/ETG unstable at $k_y\rho_s < 1$

We begin with local linear simulations for position near the mid pedestal. These modes are often unstable over a broad range of $k_y\rho_s$.

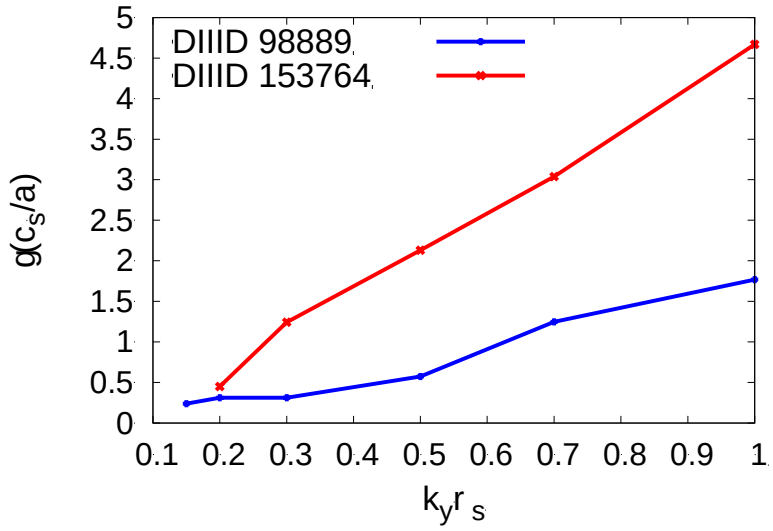

Figure 2.14(a): Growth rate for TEM/ETG modes at mid-pedestal locations for the DIII-D pedestals.

TEM/ETG frequency is smaller than or on the order of ω_b

The modes have frequencies less than or of order of the electron bounce frequency, hence, they can be considered Trapped Electron Modes.

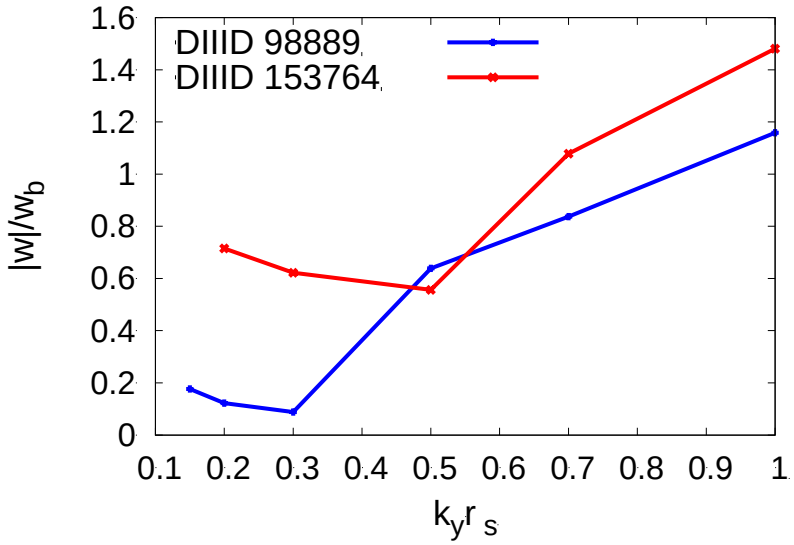

Figure 2.14(b): Frequency normalized by electron bounce frequency for TEM/ETG modes at mid-pedestal locations for the DIII-D pedestals.

TEM/ETG tend to have $k_x\rho_s > 1$

The modes have large radial wavenumbers, $k_x\rho_i >> 1$, even though they have $k_y\rho_i < 1$. Because these modes have large $k_\perp$, their mixing length diffusivity, $\gamma/k_\perp^2$ is very small, ~ 0.01 in gryoBohm units, or ~ .003 m^2/s. This is a low level diffusivity, even for a pedestal (It is about 2 orders of magnitude less than the heat diffusivity, and one order of magnitude less than the particle diffusivity, for shot 98889). Hence, even if these modes are operative, we expect that the transport level that they produce will not be significant. Additionally, due to the high $k_\perp$ of this mode, the magnetic fluctuations they produce will be very small at the Mirnov coils.

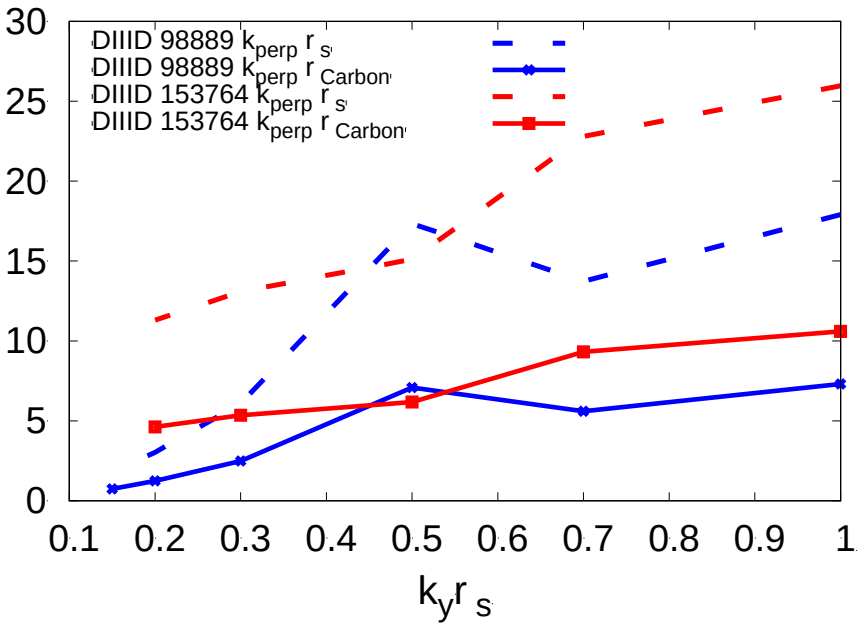

Figure 2.14(c): $k_\perp \rho_s$ *and* $k_\perp \rho_{carbon}$ for TEM/ETG modes at mid-pedestal locations for the DIII-D pedestals.

Transport Fingerprint

For completeness, we consider the transport fingerprints of these modes. Since $k_x\rho_i >> 1$ for the main ion species (deuterium), this species is nearly adiabatic, and there

is little transport in this channel. However, for impurity species, $k_x\rho_z$ can be of order 1. Hence, we expect these modes can cause particle transport for impurities, and electrons, but not for the main ion species.

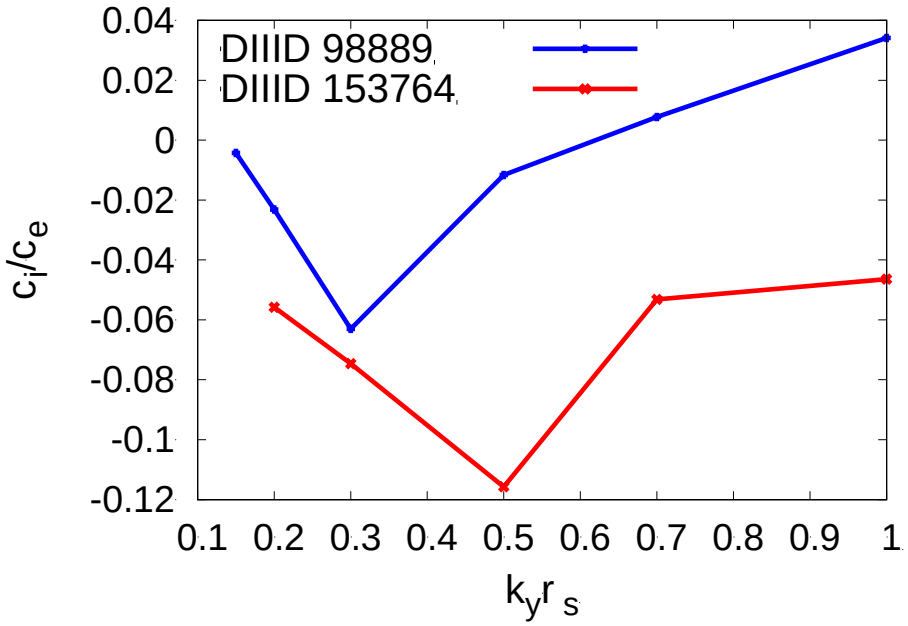

Figure 2.14(d): Ratio of ion to electron thermal diffusivity for TEM/ETG modes at mid-pedestal locations for the DIII-D pedestals.

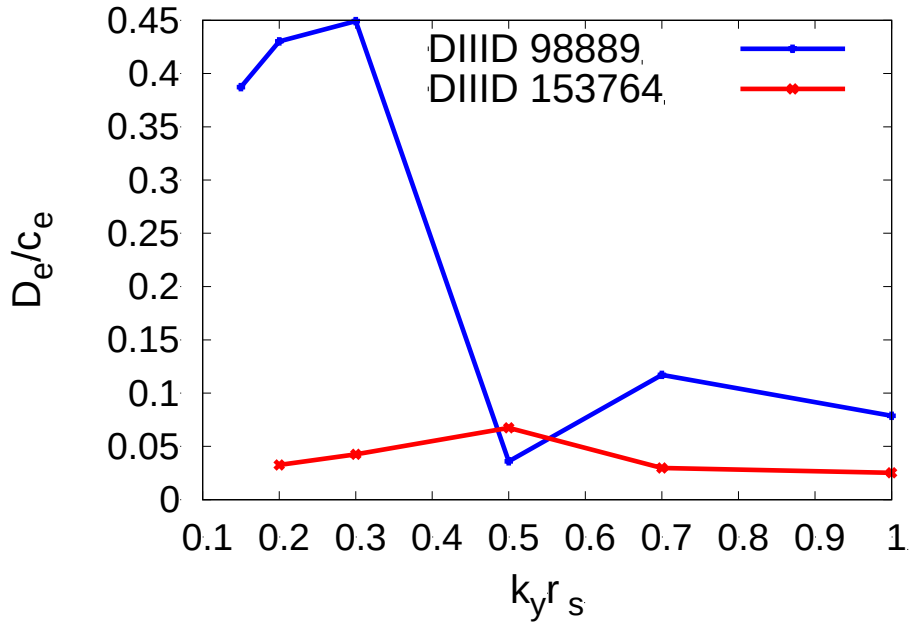

Figure 2.14(e): Ratio of electron particle diffusivity to thermal diffusivity for TEM/ETG modes at mid-pedestal locations for the DIII-D pedestals.

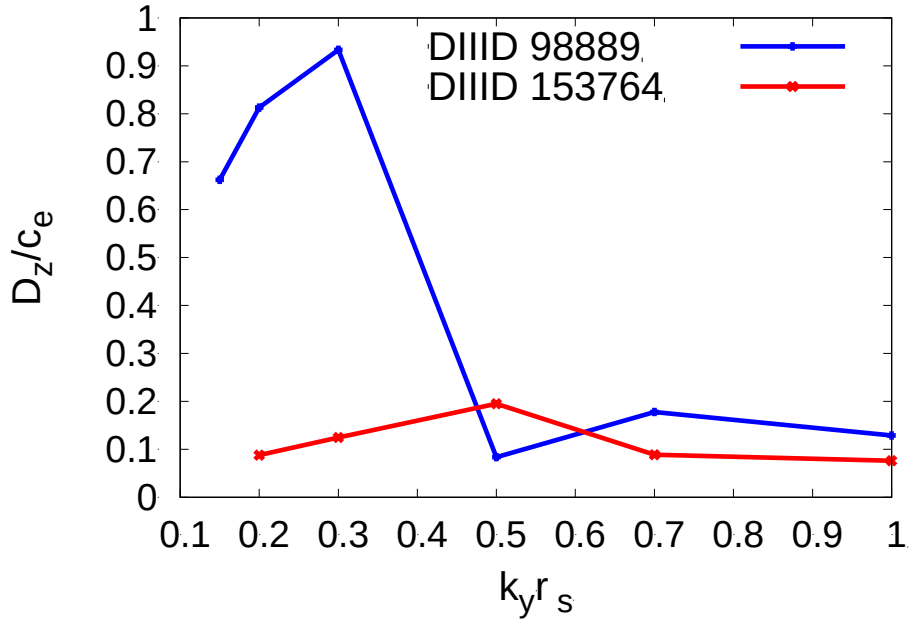

Figure 2.14(f): Ratio of impurity particle to thermal diffusivity for TEM/ETG modes at mid-pedestal locations for the DIII-D pedestals.

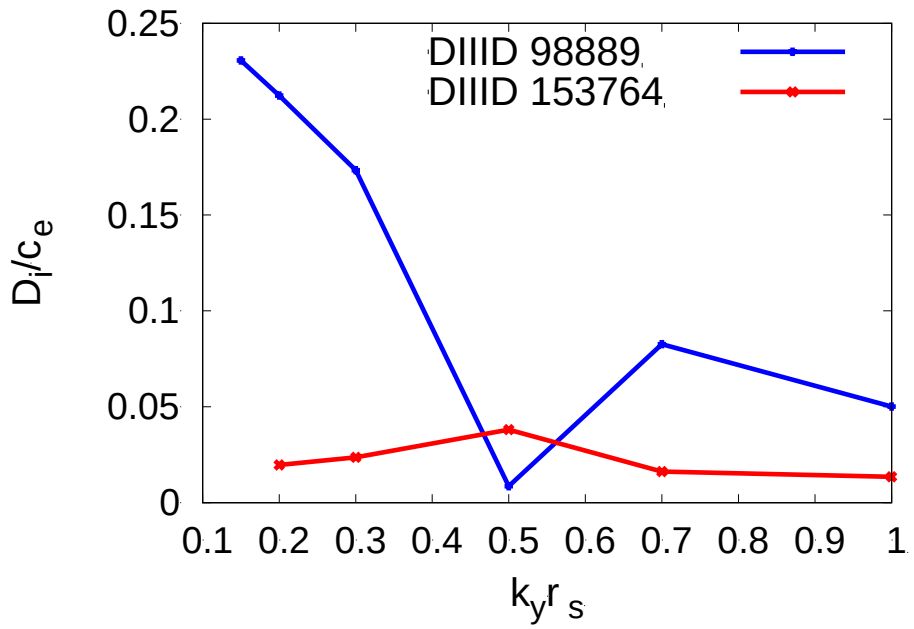

Figure 2.14(g): Ratio of ion particle diffusivity to electron thermal diffusivity for TEM/ETG modes at mid-pedestal locations for the DIII-D pedestals.

ITG/TEM

Local linear simulations

ITG/TEM suppressed by ExB shear

These modes are found at the top of the pedestal for shot 98889.

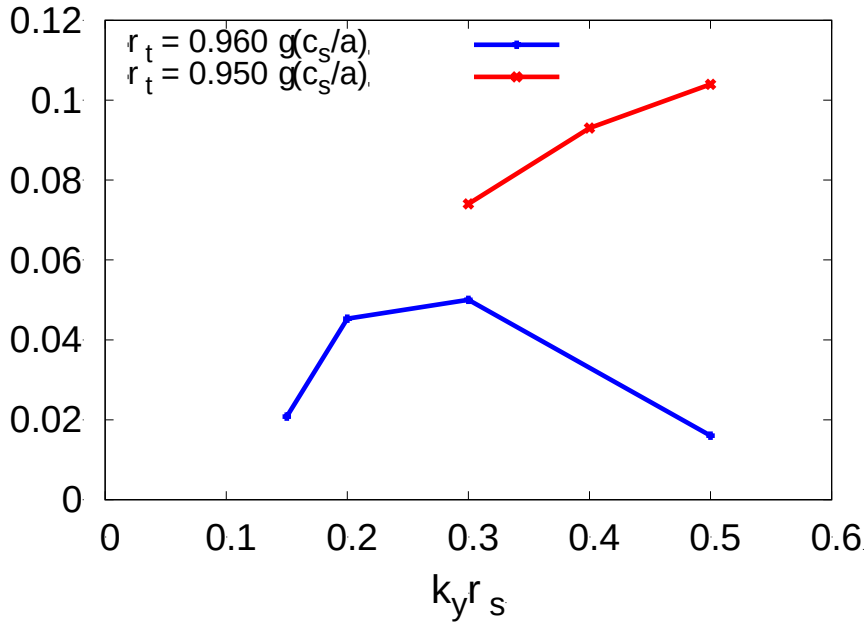

Figure 2.15(a): Growth rate for ITG/TEM modes at top-pedestal locations for DIII-D 98889.

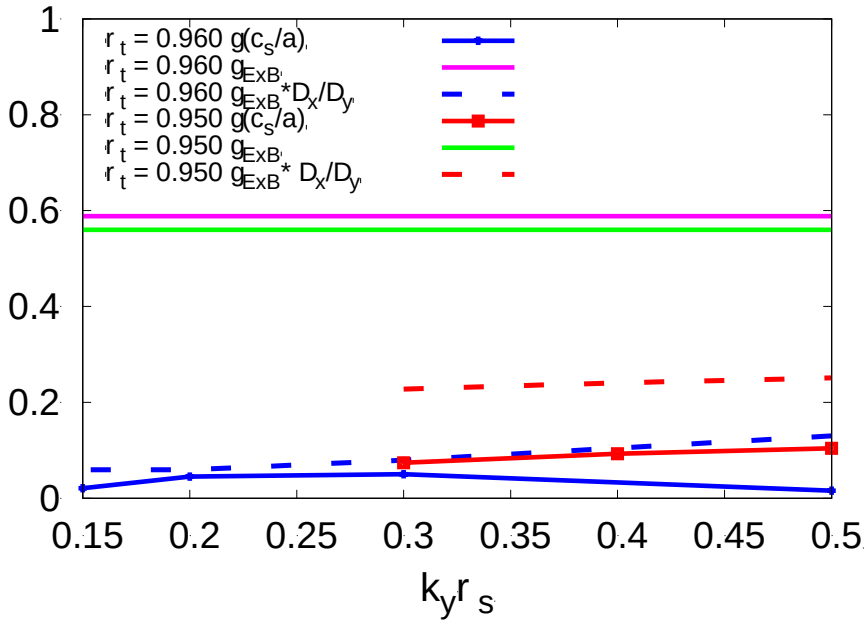

Figure 2.15(b): Growth rate and ExB shearing rate for ITG/TEM modes at top-pedestal locations for DIII-D 98889.

In nonlinear simulations of ITG modes, the ExB shear has been found to quench these modes when $\gamma < \gamma_E$. This is found to be true by a large margin, as seen above. Hence, we do not expect these modes to be important for the shots considered here. However, for completeness, we consider their properties below.

ITG/TEM frequency

As mentioned above, the modes are slab-like, with $\omega \leq k_z v_{th,i}$.

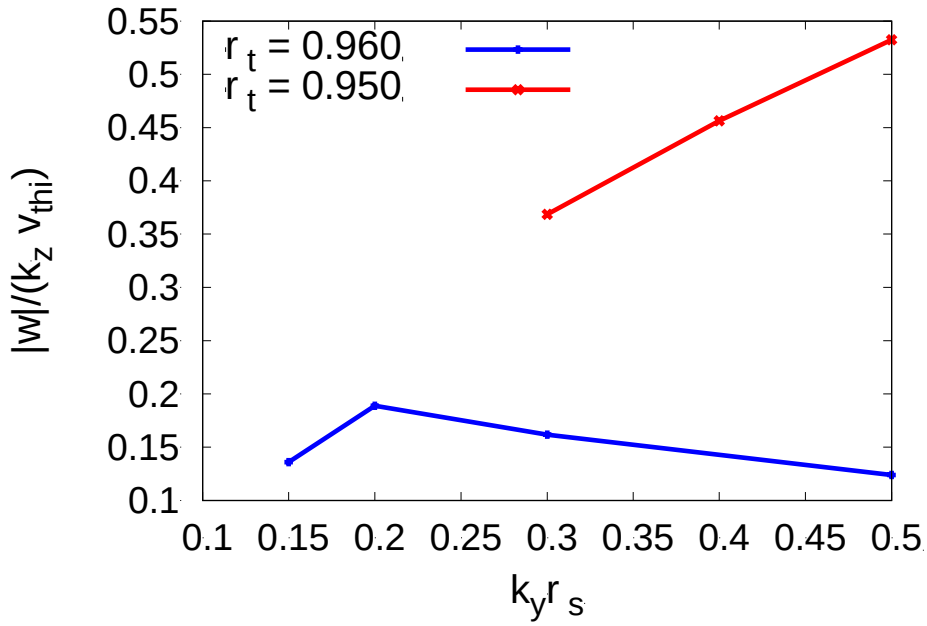

Figure 2.15(c): Frequency normalized by $k_z v_{th,i}$ for ITG/TEM modes at top-pedestal locations for DIII-D 98889.

In fact, ω can be so small that it is of order the ion bounce frequency; hence, these modes can sometimes be considered the trapped ion branch of the ITG mode.

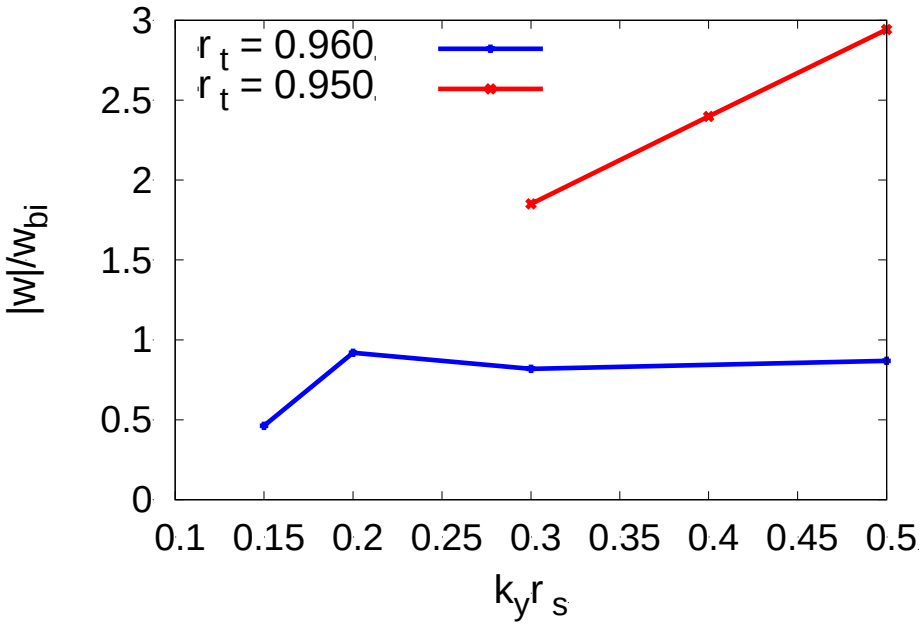

Figure 2.15(d): Frequency normalized by ion bounce frequency for ITG/TEM modes at top-pedestal locations for DIII-D 98889.

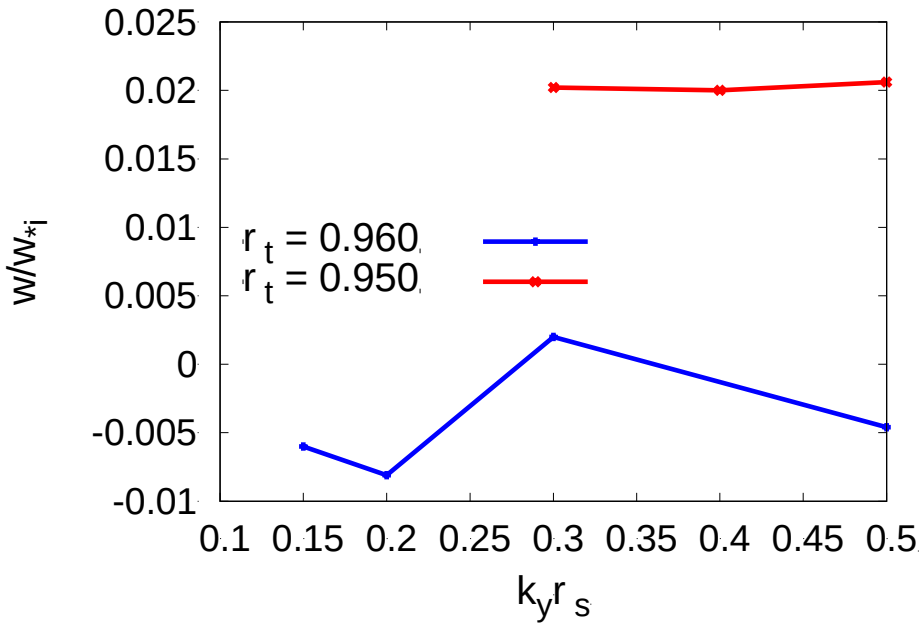

Figure 2.15(e): Frequency normalized by ion diamagnetic frequency for ITG/TEM modes at top-pedestal locations for DIII-D 98889. The frequency of these modes in pedestals are much less than ω_i*.

ITG/TEM transport fingerprint

The transport fingerprint of these modes is as one would expect for ITG-like modes. The electrons are roughly adiabatic. The ion thermal transport dominates, with other channels being relatively weak. However, these modes do affect impurity particle transport. As found in the analysis of the C-mod I-mode discharge, the impurity particle diffusivity can be even higher than the ion thermal diffusivity.

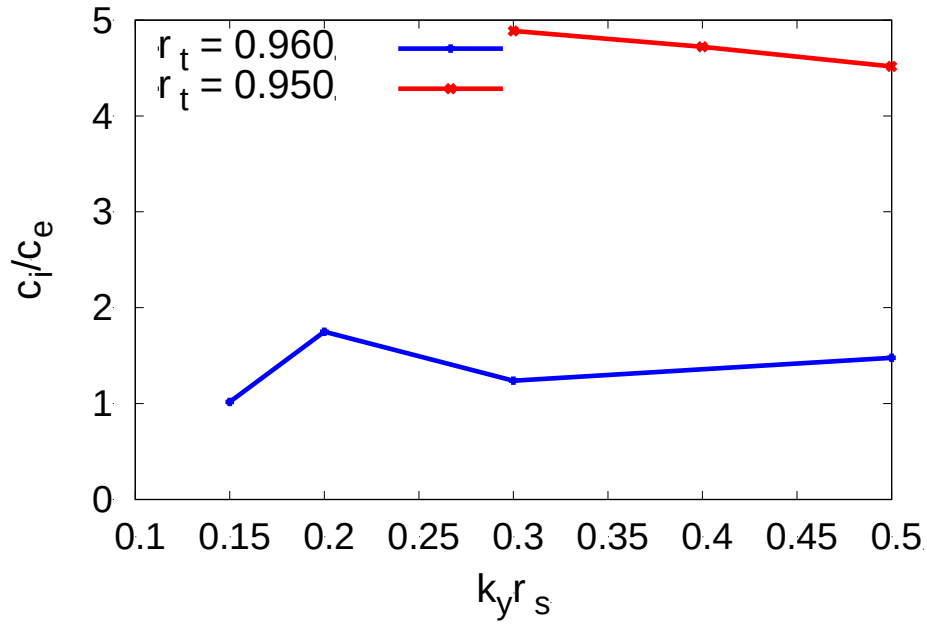

Figure 2.15(f): Ratio of ion to electron thermal diffusivity for ITG/TEM modes at top-pedestal locations for DIII-D 98889.

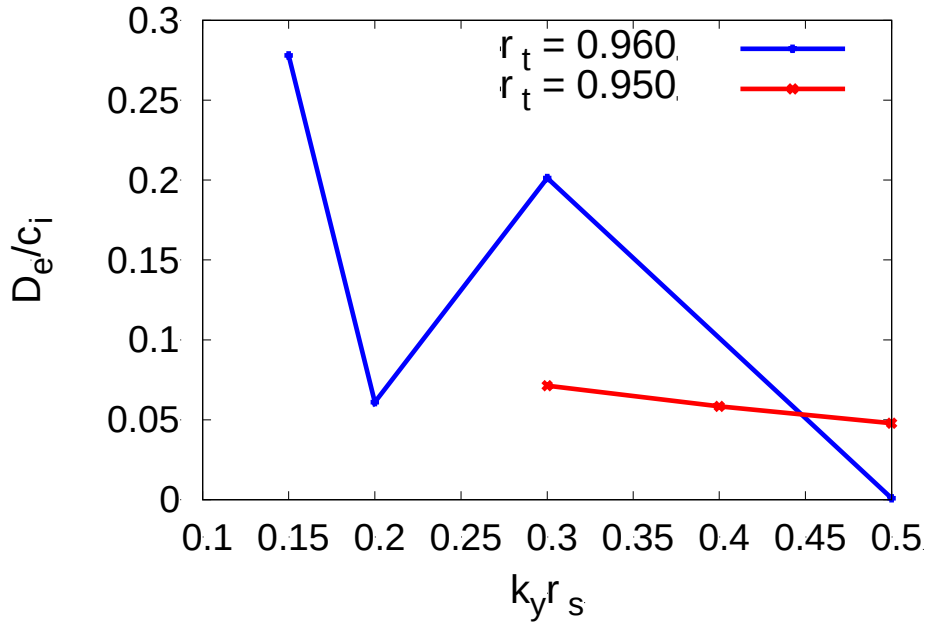

Figure 2.15(g): Ratio of electron particle diffusivity to ion thermal diffusivity for ITG/TEM modes at top-pedestal locations for DIII-D 98889.

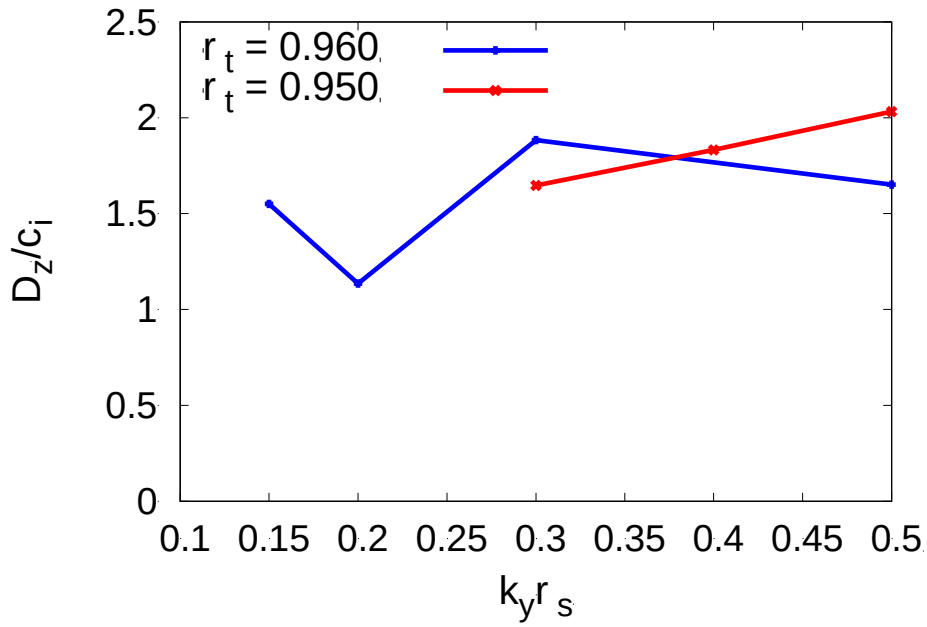

Figure 2.15(h): Ratio of impurity diffusivity to ion thermal diffusivity for ITG/TEM modes at top-pedestal locations for DIII-D 98889.

TOROIDAL ALFVEN EIGENMODE/ MICRO TEARING MODES (TAE/MTM)

In a pedestal, because of steep gradients, the diamagnetic frequency ω_e^* can also be the same as the frequency of Alfven eigenmodes. Thus, we find that hybrid MTM/TAE modes appear. Like MTM, these modes produce predominantly electron thermal transport. However, the transport has a substantial electrostatic component as well as an electromagnetic component. We can consider these to be a variant of MTM.

These modes appear primarily in local linear runs. Usually, they exist only for a narrow range of k_x, and cannot satisfy the criterion $\Delta k_x\, w > 2$. An example of a such a typical case is shown below, from shot 153674/5 at $\rho_t = 0.977$ and n=13. We plot relevant quantities verses k_x:

The mode simultaneously satisfies $\omega \sim \omega_e^*$, and $\omega \sim k_{||}\, V_{Alfven}$ (where $k_{||}^2$ is estimated from the numerically obtained eigenfunction by $\int dz\, |d\phi/dx|^2 / \int dz\, |\phi|^2$).

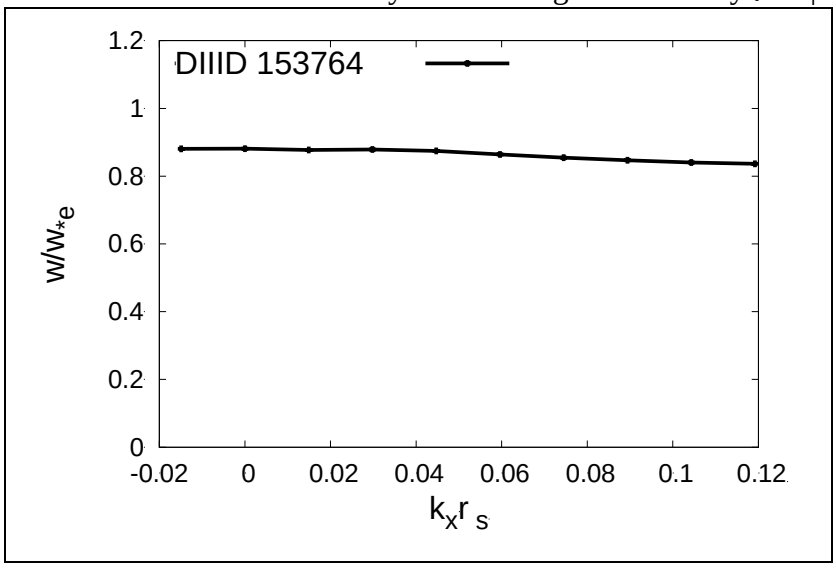

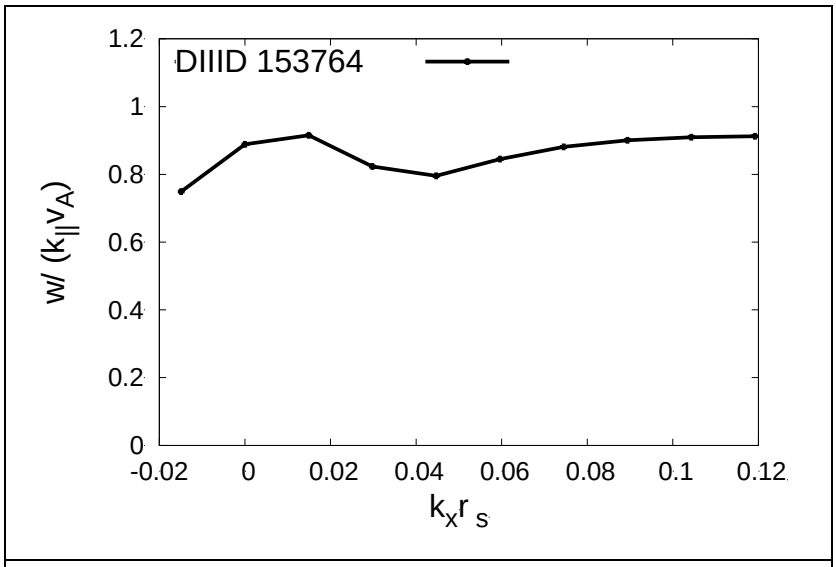

Figure 2.16 (a): The frequency normalized to ω_e* and to to $k_{||}V_A$ for the local linear TAE/MTM in 153674/5 at ρ_t = 0.977 (base case)

The heat flux for this case is predominantly electrostatic, so the mode is not a typical MTM. Also, the $E_{||}$ is small, so the mode is MHD-like.

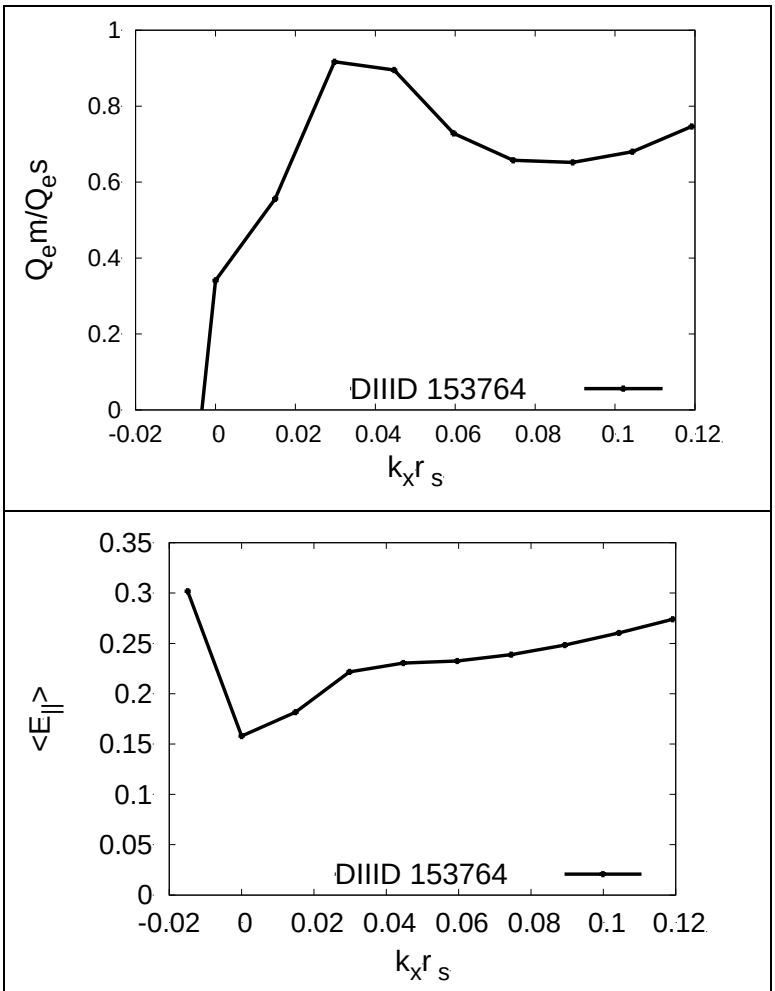

Figure 2.16 (b): The ratio of electromagnetic to electrostatic heat flux is less than 1, which shows that the mode cannot be an MTM. Also, the $E_{||}$ cancelation is typical of an MHD-like mode.

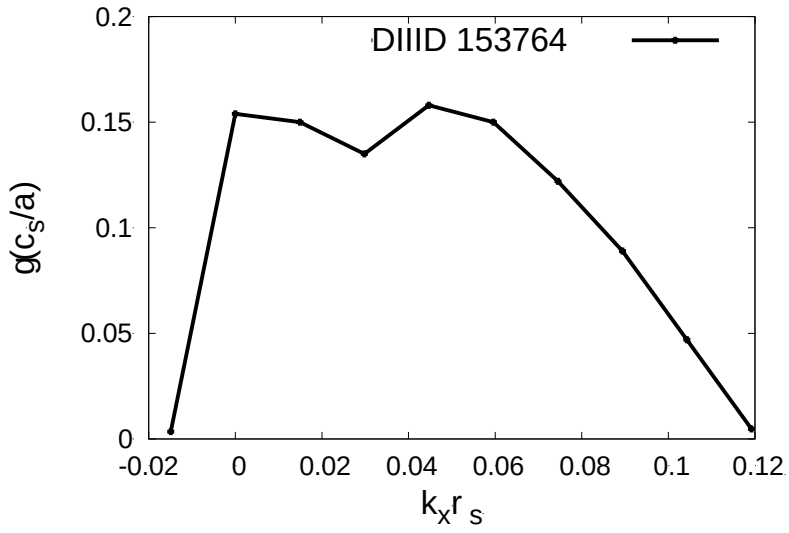

Figure 2.16(c): Growth rate for TAE/MTM modes for DIII-D 153764 base case at ρ_t = 0.977 and n=13.

The growth rate vs $k_x\rho_s$ for this typical TAE/MTM; the mode cannot fit into a box of the width of a pedestal, which is typical of this type of mode.

The transport fingerprints of the typical TAE/MTM mode are typical of an MTM, however, as seen in Fig 2.16(d).

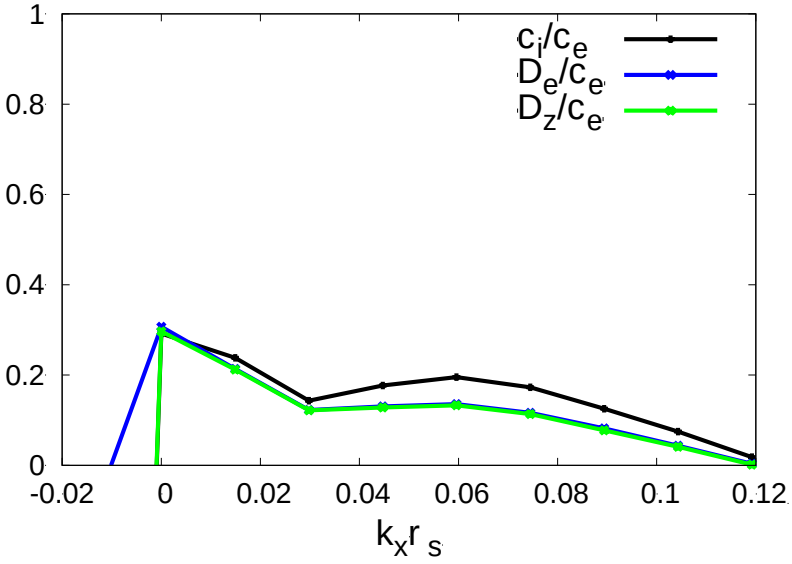

Figure 2.16 (d): The transport fingerprints of the typical TAE/MTM mode are typical of an MTM.

One case of a TAE/MTM has been found which can fit into a box, with $\Delta k_x w > 2$. This is from shot 98889, for n = 18. An instability was found in global simulations (Table 2.6). The global mode has predominantly electromagnetic heat transport, although is does have significant electrostatic flux. The mode has the same transport fingerprint as an MTM.

Case	Toroidal mode number (n)	χ_i / χ_e	$De/\chi e$	$Dz/\chi e$	Q_{es}/Q_{em}
98889	18	0.062	0.053	0.070	0.54

Table 2.6: Summary of global linear MTM simulation result for DIIID 98889 n=18.

CONCLUSION

C-MOD I-MODE

We identify the Weakly Coherent Mode (WCM) as primarily slab-like ITG modes whose growth rates are very sensitive to the impurity density gradient. Since this mode appears to be insensitive to collisionality parameter scans, we exclude the possibility of the mode being Resistive Ballooning mode. Impurity outflux computed from the nonlinear simulations of the ITG/Impurity modes indicate that this mode could cause significant impurity particle transport. The experimental impurity confinement time measured by the laser blow-off experiment is reproduced by nonlinear simulations of impurity profile variations. We discuss the sensitivity of power loss through ETG turbulence on profile gradients and the impurity level. Nonlinear simulations show that the ETG turbulence could be responsible for dominant heat transport by matching experimental power balance in the middle of the pedestal. In summary, simulation result of ITG/Impurity modes and ETG modes are consistent with the experimental transport ratios we inferred from profiles and sources: the impurity diffusivity is on the order of thermal diffusivity ($D_z \sim \chi_e$) and the main electron diffusivity is much smaller than the electron thermal diffusivity ($D_e << \chi_e$).

DIII-D H-MODES

We apply the 'transport fingerprints' concept to guide us in matching GENE simulation results to the experimental observations and transport analysis. For both DIII-D shots we analyze, transport fingerprints of MTM and ETG are consistent with experiment. The frequency of MTM in the lab frame are found to in the right range of the high band of the measured frequencies of the pedestal quasi-coherent fluctuations (QCF). Depending on the profiles, heat transport from a combination of MTM and ETG turbulence could explain experimental power loss for both H-modes. We exclude KBM from a candidate of QCF based on the discrepancy of its frequency in the lab frame to the observed

frequency of QCF. KBM also doesn't have the right transport fingerprints to be a dominant heat transport process.

We note that small changes in the pedestal profiles have large effect on stability and transport from MTM, ETG and KBM. Given the experimental uncertainties, in order to identify the modes responsible for fluctuations and transport, it's very important to 1) compare the transport fingerprints with experimental pedestal behavior and transport; 2) compare the mode frequency with measured fluctuation frequencies in the lab frame.

Reference

1. Wagner F., Plasma Phys. Control. Fusion 49 (2007) B1
2. Wesson, "Tokamaks", International Series of Monographs on Physics (Book 149), Oxford University Press, 2011
3. F. Jenko, W. Dorland, M. Kotschenreuther, and B. N. Rogers, Phys. Plasmas 7, 1904 (2000).
4. F. Jenko, D. Told, P. Xanthopoulos, F. Merz, and L. D. Horton, Phys. Plasmas 16 , 055901 (2009)
5. D.R. Hatch, D. Told, F. Jenko, H. Doerk, M.G. Dunne, E. Wolfrum, E. Viezzer, The ASDEX Upgrade Team and M.J. Pueschel, 2015 Nucl. Fusion 55 063028
6. D.R. Hatch, M. Kotschenreuther, S. Mahajan, P. Valanju, F. Jenko, D. Told, T. Görler and S. Saarelma, 2016 Nucl. Fusion 56 104003
7. D.R. Hatch, M. Kotschenreuther, S. Mahajan, P. Valanju and X. Liu, 2017 Nucl. Fusion 57 036020
8. M. Kotschenreuther, D.R. Hatch, S. Mahajan, P. Valanju, L. Zheng and X. Liu, 2017 Nucl. Fusion 57 064001
9. C Theiler, J L Terry, E Edlund, I Cziegler, R M Churchill, J W Hughes, B LaBombard, T Golfinopoulos and the Alcator C-Mod Team, 2017 Plasma Phys. Control. Fusion 59 025016
10. Z. X. Liu, X. Q. Xu, X. Gao, A. E. Hubbard, J. W. Hughes, J. R. Walk, C. Theiler, T. Y. Xia, S. G. Baek, T. Golfinopoulos, D. Whyte, T. Zhang, and J. G. Li, Physics of Plasmas 23, 120703 (2016)
11. D.G. Whyte, A.E. Hubbard, J.W. Hughes, B. Lipschultz, J.E. Rice, E.S. Marmar, M. Greenwald, I. Cziegler, A. Dominguez, T. Golfinopoulos, N. Howard, L. Lin, R.M. McDermott, M. Porkolab, M.L. Reinke, J. Terry, N. Tsujii, S.Wolfe, S.Wukitch, Y. Lin and the Alcator C-Mod Team, 2010 Nucl. Fusion 50 105005
12. A. E. Hubbard, D. G. Whyte, R. M. Churchill, I. Cziegler, A. Dominguez, T. Golfinopoulos, J. W. Hughes, J. E. Rice, I. Bespamyatnov, M. J. Greenwald, N. Howard, B. Lipschultz, E. S. Marmar, M. L. Reinke, W. L. Rowan, J. L. Terry, and Alcator C-Mod Group, Physics of Plasmas 18 (2011): 056115
13. Coppi, B., and T. Zhou. "Heavy Particle Modes and Signature of the I-Regime." Physics Letters A 375, no. 32 (July 2011): 2916–2920.
14. J. Q. Dong, W. Horton, and W. Dorland, Physics of Plasmas 1, 3635 (1994)
15. A. Dominguez, "Study of density fluctuations and particle transport at the edge of I-mode plasmas," Ph.D. thesis (Massachusetts Institute of Technology, 2012).
16. J.E. Rice, M.L. Reinke, C. Gao, N.T. Howard, M.A. Chilenski, L. Delgado-Aparicio, R.S. Granetz, M.J. Greenwald, A.E. Hubbard, J.W. Hughes, J.H. Irby, Y. Lin, E.S. Marmar, R.T. Mumgaard, S.D. Scott, J.L. Terry, J.R. Walk, A.E. White, D.G. Whyte, S.M. Wolfe and S.J. Wukitch, 2015 Nucl. Fusion 55 033014

17. I. Cziegler, P. H. Diamond, N. Fedorczak, P. Manz, G. R. Tynan, M. Xu, R. M. Churchill, A. E. Hubbard, B. Lipschultz, J. M. Sierchio, J. L. Terry, and C. Theiler, Physics of Plasmas 20, 055904 (2013)

18. S. J. Zweben, J. L. Terry, D. P. Stotler, and R. J. Maqueda, Review of Scientific Instruments 88, 041101 (2017)

19. A. Diallo, R. J. Groebner, T. L. Rhodes, D. J. Battaglia, D. R. Smith, T. H. Osborne, J. M. Canik, W. Guttenfelder, and P. B. Snyder, Phys. Plasmas 22, 056111 (2015)

20. J.D. Callen, R.J. Groebner, T.H. Osborne, J.M. Canik, L.W. Owen, A.Y. Pankin, T. Rafiq, T.D. Rognlien and W.M. Stacey Nucl. Fusion 50 (2010) 064004

21. Hirshman S.P. and Whitson J.C. 1983 Phys. Fluids 26 3553

22. O. Sauter, C. Angioni, and Y. R. Lin-Liu, Physics of Plasmas 6, 2834 (1999)

23. R. Hager and C.S. Chang, Physics of Plasmas 23, 042503 (2016)

24. J. W. Connor, R. J. Hastie, and J. B. Taylor, 1978 Phys. Rev. Lett. 40, 396

25. Y. Z. Zhang and S. M. Mahajan, Physics of Fluids B, 5,2000 (1993)

26. K. Burrell Phys. Plasmas 4 (5) 1499 (1996)

27. T. S. Hahm and Burrell Phys. Plasmas 2 (5) 1648 (1995)

28. W. Guttenfelder, J. L. Peterson, J. Candy, S. M. Kaye, Y. Ren, R. E. Bell, G. W. Hammett, B. P. LeBlanc, D. R. Mikkelsen, W. M. Nevins and H. Yuh, Nucl. Fusion 53 (2013) 093022

29. J.M. Canik, W. Guttenfelder, R. Maingi, T.H. Osborne, S. Kubota, Y. Ren, R.E. Bell, H.W. Kugel, B.P. LeBlanc and V.A. Souhkanovskii, Nucl. Fusion 53 (2013) 113016

30. P.B. Snyder, R.J. Groebner, J.W. Hughes, T.H. Osborne, M. Beurskens, A.W. Leonard, H.R. Wilson and X.Q. Xu, Nucl. Fusion 51 (2011) 103016

31. M. Kotschenreuther, The Physics of Fluids 29, 2898 (1986)

32. Told D. 2012 PhD Thesis Universitat Ulm

33. A. Navarro, private communication

34. C. Michoski, in process